University of Windsor
Scholarship at UWindsor

Electronic Theses and Dissertations

1998

ESR studies of some iron(II) spin crossover complexes.

Raymond Chi Wai. Sung
University of Windsor

Follow this and additional works at: http://scholar.uwindsor.ca/etd

Recommended Citation

Sung, Raymond Chi Wai., "ESR studies of some iron(II) spin crossover complexes." (1998). *Electronic Theses and Dissertations.* Paper 1954.

This online database contains the full-text of PhD dissertations and Masters' theses of University of Windsor students from 1954 forward. These documents are made available for personal study and research purposes only, in accordance with the Canadian Copyright Act and the Creative Commons license—CC BY-NC-ND (Attribution, Non-Commercial, No Derivative Works). Under this license, works must always be attributed to the copyright holder (original author), cannot be used for any commercial purposes, and may not be altered. Any other use would require the permission of the copyright holder. Students may inquire about withdrawing their dissertation and/or thesis from this database. For additional inquiries, please contact the repository administrator via email (scholarship@uwindsor.ca) or by telephone at 519-253-3000ext. 3208.

INFORMATION TO USERS

This manuscript has been reproduced from the microfilm master. UMI films the text directly from the original or copy submitted. Thus, some thesis and dissertation copies are in typewriter face, while others may be from any type of computer printer.

The quality of this reproduction is dependent upon the quality of the copy submitted. Broken or indistinct print, colored or poor quality illustrations and photographs, print bleedthrough, substandard margins, and improper alignment can adversely affect reproduction.

In the unlikely event that the author did not send UMI a complete manuscript and there are missing pages, these will be noted. Also, if unauthorized copyright material had to be removed, a note will indicate the deletion.

Oversize materials (e.g., maps, drawings, charts) are reproduced by sectioning the original, beginning at the upper left-hand corner and continuing from left to right in equal sections with small overlaps.

Photographs included in the original manuscript have been reproduced xerographically in this copy. Higher quality 6" x 9" black and white photographic prints are available for any photographs or illustrations appearing in this copy for an additional charge. Contact UMI directly to order.

Bell & Howell Information and Learning
300 North Zeeb Road, Ann Arbor, MI 48106-1346 USA
800-521-0600

UMI®

ESR STUDIES OF SOME IRON(II) SPIN CROSSOVER COMPLEXES

by

Raymond Chi Wai Sung

A Dissertation
Submitted to the Faculty of Graduate Studies and Research
through the Department of Chemistry and Biochemistry
in Partial Fulfillment of the Requirements for
the Degree of Doctor of Philosophy at the
University of Windsor

Windsor, Ontario, Canada

November 1997

©1997 Raymond Chi Wai Sung

National Library of Canada
Acquisitions and Bibliographic Services
395 Wellington Street
Ottawa ON K1A 0N4
Canada

Bibliothèque nationale du Canada
Acquisitions et services bibliographiques
395, rue Wellington
Ottawa ON K1A 0N4
Canada

Your file Votre référence

Our file Notre référence

The author has granted a non-exclusive licence allowing the National Library of Canada to reproduce, loan, distribute or sell copies of this thesis in microform, paper or electronic formats.

L'auteur a accordé une licence non exclusive permettant à la Bibliothèque nationale du Canada de reproduire, prêter, distribuer ou vendre des copies de cette thèse sous la forme de microfiche/film, de reproduction sur papier ou sur format électronique.

The author retains ownership of the copyright in this thesis. Neither the thesis nor substantial extracts from it may be printed or otherwise reproduced without the author's permission.

L'auteur conserve la propriété du droit d'auteur qui protège cette thèse. Ni la thèse ni des extraits substantiels de celle-ci ne doivent être imprimés ou autrement reproduits sans son autorisation.

0-612-52415-9

Canada

ABSTRACT

X-band ESR powder studies have been done on the spin transition in Mn^{2+} doped $[Fe(bpp)_2][CF_3SO_3]_2.H_2O$, $[Fe(bpp)_2][BF_4]_2$ and $[Fe(5\text{-}NO_2\text{-}sal\text{-}N(1,4,7,10))]$ complexes. The use of Mn^{2+} as an ESR probe in the studies is based on the knowledge that the ion is very sensitive to changes in its surrounding environment, enabling the changes within the system during HS ↔ LS crossover to be observed. The computer simulations of the powder ESR spectra of Mn^{2+} ion in these complexes using the SimFonia simulation program, obtained from Bruker, gave numerical values of D and E for Mn^{2+} in the $[Fe(bpp)_2][CF_3SO_3]_2.H_2O$ and $[Fe(bpp)_2][BF_4]_2$ systems. The magnitudes of D for Mn^{2+} ion are very different in the HS and LS phases of both the $[Fe(bpp)_2][CF_3SO_3]_2.H_2O$ and $[Fe(bpp)_2][BF_4]_2$ systems, indicating that the spin transition in these systems is accompanied by a phase transformation. The spectra show that during the transition there are separate domains for each spin state. Attempts to simulate the powder ESR spectra of Mn^{2+} in $[Fe(5\text{-}NO_2\text{-}sal\text{-}N(1,4,7,10))]$ complex were unsuccessful owing to their poor quality, and further ESR study of this system was not pursued.

The temperature-dependence studies of $[Fe(bpp)_2][CF_3SO_3]_2.H_2O$ complex showed a sudden transition at 134K in the cooling direction and a two stage transition at 177K and 280K for the first and second stage, respectively, and a plateau region from 180K to 275K in the heating direction. The comparison between these results and those reported in the literature revealed a marked difference of 13K in the HS → LS transition temperature, but the reverse transition temperatures are in good agreement except that the LS → HS conversion occurs over a much smaller interval of 5K and 9K for the first and second stage transition, respectively, in the ESR measurements relative to the 40K and 50K for the corresponding stages reported in the literature. These discrepancies may simply be due to differences in the final process of drying the samples. The results from the irradiation experiments on the $[Fe(bpp)_2][CF_3SO_3]_2.H_2O$ complex indicate that the LIESST induced spin transition at liquid nitrogen temperature is not accompanied by a phase transformation. The kinetic studies of HS → LS phase transformation in the

system, when the HS state is formed by rapidly cooling the HS state, indicate that the thermally-induced spin crossover is coupled to the phase transformation.

Similar results were also obtained for the [Fe(bpp)$_2$][BF$_4$]$_2$ complex. The transition temperatures for the system were found to be 166K and 173K in the cooling and heating directions, respectively, giving a 7K difference in the hysteresis curves. The differences between these results and those reported in the literature are small, and could also be attributed to the slight differences in the drying process. The results obtained from the irradiation studies are practically the same as those observed in the [Fe(bpp)$_2$][CF$_3$SO$_3$]$_2$.H$_2$O complex. The results obtained from HS → LS phase transformation studies indicate that the phase transformation in the system is followed by the spin-state transition.

In summary, ESR studies of [Fe(bpp)$_2$][CF$_3$SO$_3$]$_2$.H$_2$O show that the phase transformation is coupled to the thermally-induced spin crossover, whereas in [Fe(bpp)$_2$][BF$_4$]$_2$ the phase transformation takes place first. The rate of HS → LS phase transformation in the [Fe(bpp)$_2$][CF$_3$SO$_3$]$_2$.H$_2$O system, when the HS state is formed by rapidly cooling the HS state, is the same as the HS → LS conversion reported in the literature using magnetic susceptibility measurements. The rate of HS → LS phase transformation in the [Fe(bpp)$_2$][BF$_4$]$_2$ system, when the HS state is formed by rapidly cooling the HS state, is twice the rate of the spin-state transition reported in the literature using Mössbauer spectroscopy. There is also no evidence of a phase change seen in the ESR spectra of the [Fe(5-NO$_2$-sal-N(1,4,7,10))] complex.

ACKNOWLEDGEMENTS

With great pleasure, I acknowledge my sincere thanks to Dr. Bruce R. McGarvey for his patient, guidance, skill in elucidating the many problems encountered during this work and, not least, for his enthusiasm and encouragement.

I thank my friends, Dr. Andrew Ozarowski for many helpful discussions, Mr. Mike Fuerth for his assistance in the operation of the Bruker AVANCE DPX 300 MHz NMR spectrometer and Mr. Bill Price for his assistance in the operation of the Lexel 95 Ar-laser and the Spectra Physics 2000 Kr-laser.

I am grateful to Dr. Ricardo Aroca for allowing the use of the laser equipment during the irradiation studies of the $[Fe(bpp)_2][CF_3SO_3]_2.H_2O$ and $[Fe(bpp)_2][BF_4]_2$ complexes.

Dr. Stephen J. Loeb is also thanked for his expert advice on the synthesis of $[Fe(5\text{-}NO_2\text{-}sal\text{-}N(1,4,7,10))]$ complex.

Finally, I would like to express my gratitude, once again, to Dr. Bruce R. McGarvey, for reading the entire manuscript and for helpful advice and innumerable suggestions.

TABLE OF CONTENTS

ABSTRACT

ACKNOWLEDGEMENTS

LIST OF TABLES

LIST OF FIGURES

LIST OF ABBREVIATIONS

CHAPTER

1 THEORY OF ELECTRON SPIN RESONANCE

1.1 Introduction 1

1.2 Crystal Field Splitting 3

1.3 Spin-Orbit Coupling 5

1.4 g-Factor 8

1.5 Nuclear Hyperfine Splitting 10

1.6 Zero-Field Splitting Parameters 12

1.7 ESR Spectrum of Mn^{2+} Ion 14

1.8 Powder ESR Spectra 16

2 GENERAL FEATURES OF SPIN CROSSOVER COMPLEXES

2.1 Spin Crossover Phenomenon 18

2.2 Magnetic Property 20

2.3 Methods of Study 22

2.4 Light-Induced Excited Spin State Trapping (LIESST) 24

2.5 Effect of Pressure 26

3 CHEMICAL SYNTHESIS AND ANALYSIS OF COMPLEXES

3.1 Materials and Chemicals 27

3.2 Preparation of 2,6-bis(pyrazol-3-yl) pyridine (bpp) ligand 28

3.3 Preparation of Mn^{2+} doped $[Fe(bpp)_2][CF_3SO_3]_2.H_2O$ Complex 28
3.4 Preparation of Mn^{2+} doped $[Fe(bpp)_2][BF_4]_2$ Complex 29
3.5 Preparation of Mn^{2+} doped $[Fe(5\text{-}NO_2\text{-}sal\text{-}N(1,4,7,10))]$ Complex 29

4 TEMPERATURE-DEPENDENT ESR STUDIES

4.1 Introduction 31
4.2 Instrumentation and Apparatus 33
4.3 Calibration of Temperature 34
4.4 Variable Temperature ESR Measurements 36
4.5 ESR Spectra at Room Temperature and 77K 37
4.6 ESR Spectral Analysis and Simulations 38

4.7 Results and Discussion

$[Fe(bpp)_2][CF_3SO_3]_2.H_2O$ Complex 46
$[Fe(bpp)_2][BF_4]_2$ Complex 55
$[Fe(5\text{-}NO_2\text{-}sal\text{-}N(1,4,7,10))]$ Complex 60

5 IRRADIATION EXPERIMENTS

5.1 Introduction 65
5.2 Experimental Procedures 66

5.3 Results and Discussion

$[Fe(bpp)_2][CF_3SO_3]_2.H_2O$ Complex 67
$[Fe(bpp)_2][BF_4]_2$ Complex 68

6 KINETICS OF HS → LS PHASE TRANSFORMATION

6.1 Introduction 72
6.2 Experimental Procedures 73

6.3 Results and Discussion

$[Fe(bpp)_2][CF_3SO_3]_2.H_2O$ Complex 74
$[Fe(bpp)_2][BF_4]_2$ Complex 75

7 CONCLUSIONS 85

REFERENCES 89

VITA AUCTORIS 94

LIST OF TABLES

Table 2.1.1 19

Ground states for d^4 to d^7 configurations.

Table 4.6.1 44

Parameters used in SimFonia simulations of powder ESR spectra of Mn^{2+}-doped $[Fe(bpp)_2][CF_3SO_3]_2.H_2O$ complex.

Table 4.6.2 46

Parameters used in SimFonia simulations of powder ESR spectra of Mn^{2+}-doped $[Fe(bpp)_2][BF_4]_2$ complex.

LIST OF FIGURES

Figure 1.2.1 4

Energy levels for d^n configurations in an octahedral crystal field.

Figure 1.3.1 6

Schematic representation of energy levels for d^1 ion in distorted O_h field.

Figure 1.4.1 9

Computer-simulated powder ESR spectra with different principal g-values as indicated.

Figure 1.6.1 13

Schematic energy levels diagram showing the zero-field splitting for an $S = 1$ system with **H** along the *z* axis.

Figure 1.6.2 14

Schematic diagram showing zero-field splitting of high-spin Mn^{2+} ion in strong magnetic field.

Figure 2.1.1 18

Electronic configurations of HS and LS ground states of Fe^{2+} (d^6) system in O_h symmetry.

Figure 2.2.1 21

Schematic representation of discontinuous and continuous types of HS ↔ LS crossover.

Figure 2.2.2 21

Thermal hysteresis effect.

Figure 2.4.1 25

Schematic potential energy curves for the ground and excited states of a d^6 spin crossover system.

Figure 3.2.1 28

300MHz ^{1}H NMR spectrum of bpp ligand in DMSO-d_6 at room temperature.

Figure 4.2.1 34

Pictures showing a VT-Dewar and a 50ml finger Dewar.

Figure 4.3.1 35

Calibration of temperature.

Figure 4.6.1 40

Schematic diagram showing the resonance fields for **H** along the *z*-axis and **H** in the *xy* plane.

Figure 4.6.2 41

Powder ESR spectra of Mn^{2+} in $[Fe(bpp)_2][CF_3SO_3]_2.H_2O$ complex at 290.5K.

Figure 4.6.3 43

Powder ESR spectra of Mn^{2+} in $[Fe(bpp)_2][CF_3SO_3]_2.H_2O$ complex at temperatures T* from 239.5K to 142.5K in the cooling direction.

Figure 4.6.4 45

Temperature-dependence of D parameter for Mn^{2+} ion in HS phase of $[Fe(bpp)_2][CF_3SO_3]_2.H_2O$ complex.

Figure 4.6.5 45

Temperature-dependence of E parameter for Mn^{2+} ion in HS phase of $[Fe(bpp)_2][CF_3SO_3]_2.H_2O$ complex.

Figure 4.7.1(a) 49

Powder ESR spectra of Mn^{2+} ion in $[Fe(bpp)_2][CF_3SO_3]_2.H_2O$ complex at decreasing temperatures T* (290.5K to 149.2K).

Figure 4.7.1(b) 50

Powder ESR spectra of Mn^{2+} ion in $[Fe(bpp)_2][CF_3SO_3]_2.H_2O$ complex at decreasing temperatures T* (148.3K to 137.5).

Figure 4.7.1(c) 51

Powder ESR spectra of Mn^{2+} ion in $[Fe(bpp)_2][CF_3SO_3]_2.H_2O$ complex at decreasing temperatures T* (136.5K to 117.8K).

Figure 4.7.1(d) 52

Powder ESR spectra of Mn^{2+} ion in $[Fe(bpp)_2][CF_3SO_3]_2.H_2O$ complex at increasing temperatures T* (127.5K to 187.7K).

Figure 4.7.1(e) 53

Powder ESR spectra of Mn^{2+} ion in $[Fe(bpp)_2][CF_3SO_3]_2.H_2O$ complex at increasing temperatures T* (192.0K to 298.0K).

Figure 4.7.2 54

Powder ESR spectra of Mn^{2+} ion in $[Fe(bpp)_2][CF_3SO_3]_2.H_2O$ complex at room temperature and 77K.

Figure 4.7.3(a) 56

Powder ESR spectra of Mn^{2+} ion in $[Fe(bpp)_2][BF_4]_2$ complex at decreasing temperatures T* (289.5K to 169.7K).

Figure 4.7.3(b) 57

Powder ESR spectra of Mn^{2+} ion in $[Fe(bpp)_2][BF_4]_2$ complex at decreasing temperatures T* (168.5K to 150.3K).

Figure 4.7.3(c) 58

Powder ESR spectra of Mn^{2+} ion in $[Fe(bpp)_2][BF_4]_2$ complex at increasing temperatures T* (156.7K to 292.5K).

Figure 4.7.4 59

Powder ESR spectra of Mn^{2+} ion in $[Fe(bpp)_2][BF_4]_2$ complex at room temperature and 77K.

Figure 4.7.5(a) 61

Powder ESR spectra of Mn^{2+} ion in $[Fe(5\text{-}NO_2\text{-}sal\text{-}N(1,4,7,10))]$ complex at decreasing temperatures T* (288.0K to 167.0K).

Figure 4.7.5(b) 62

Powder ESR spectra of Mn^{2+} ion in $[Fe(5\text{-}NO_2\text{-}sal\text{-}N(1,4,7,10))]$ complex at decreasing temperatures T* (165.0K to 101.0K).

Figure 4.7.5(c) 63

Powder ESR spectra of Mn^{2+} ion in [Fe(5-NO_2-sal-N(1,4,7,10))] complex at increasing temperatures T* (127.5K to 290.5K).

Figure 4.7.6 64

Powder ESR spectra of Mn^{2+} ion in [Fe(5-NO_2-sal-N(1,4,7,10))] complex at room temperature and 77K.

Figure 5.3.1 70

Powder ESR spectra of Mn^{2+} ion in $[Fe(bpp)_2][CF_3SO_3]_2.H_2O$ complex at 77K after various treatments.

Figure 5.3.2 71

Powder ESR spectra of Mn^{2+} ion in $[Fe(bpp)_2][BF_4]_2$ complex at 77K after various treatments.

Figures 6.3.1(a) and (b) 76

Powder ESR spectra of Mn^{2+} ion in $[Fe(bpp)_2][CF_3SO_3]_2.H_2O$ complex at 104.3K, showing the kinetics of the paramagnetic to diamagnetic phase transformation.

Figure 6.3.2 78

Powder ESR spectra of Mn^{2+} ion in $[Fe(bpp)_2][CF_3SO_3]_2.H_2O$ complex at 119.6K, showing the kinetics of the paramagnetic to diamagnetic phase transformation.

Figure 6.3.3 79

Kinetic curves of the paramagnetic to diamagnetic phase transformation of $[Fe(bpp)_2][CF_3SO_3]_2.H_2O$ complex at 104.3K and 119.6K.

Figure 6.3.4 80

Relaxation curves $\gamma_{HS}(t)$ of the metastable HS state of $[Fe(bpp)_2][CF_3SO_3]_2.H_2O$ complex in the temperature range 104 - 118K. (This figure was taken from reference 73).

Figure 6.3.5 81

Powder ESR spectra of Mn^{2+} ion in $[Fe(bpp)_2][BF_4]_2$ complex at 99K showing the kinetics of the paramagnetic to diamagnetic phase transformation.

Figure 6.3.6 82

Powder ESR spectra of Mn^{2+} ion in $[Fe(bpp)_2][BF_4]_2$ complex at 104.7K showing the kinetics of the paramagnetic to diamagnetic phase transformation.

Figure 6.3.7 83

Kinetic curves of the paramagnetic to diamagnetic phase transformation of $[Fe(bpp)_2][BF_4]_2$ complex at 99K and 104.7K.

Figure 6.3.8 84

Relaxation curves $\gamma_{HS}(t)$ of the metastable HS state of $[Fe(bpp)_2][BF_4]_2$ complex in the temperature range 92.5 - 100K. (This figure was taken from reference 68).

LIST OF ABBREVIATIONS

bpp ligand	2,6-bis(pyrazol-3-yl) pyridine

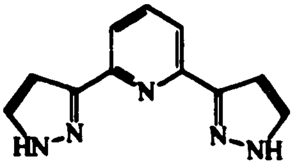

$(5\text{-}NO_2\text{-sal-N}(1,4,7,10))^{2-}$ ligand

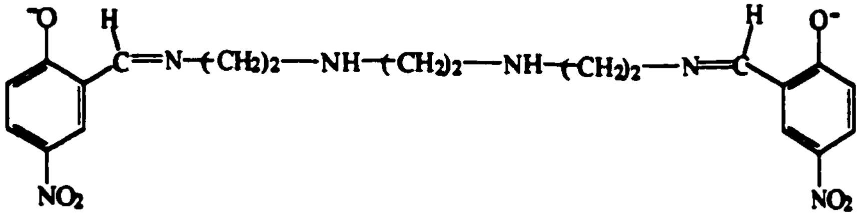

ptz	1-propyltetrazole
phen	1,10-phenanthroline
2-pic	2-(aminomethyl)pyridine or 2-picolylamine
btr	4,4'-bi-1,2,4-triazole
BT	2,2'-bi-2-thiazoline
paptH	2-(2-pyridylamino)-4-(2-pyridyl)thiazole
bpen	N,N'-bis(2-pyridylmethyl)-1,2-ethanediamine
L ligand	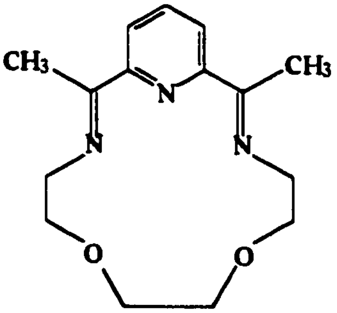

$\hat{\ell}$	orbital angular momentum operator of a single electron
$\hat{s}$	spin angular momentum operator of a single electron
ΔH°	standard enthalpy change

ΔS°	standard entropy change
ΔG°	standard free energy change
$\hat{S}$	total electronic spin angular momentum operator
$\hat{L}$	total orbital angular momentum operator
λ	spin-orbit coupling constant
Δ	crystal field energy
ν	frequency of radiation
$\boldsymbol{\mu}$	magnetic dipole moment vector
μ	magnitude of magnetic dipole moment
Π	mean spin-pairing energy
δ	NMR chemical shift in parts per million
π^*	antibonding π orbitals
β_e	Bohr magneton
μ_{eff}	magnitude of effective magnetic dipole moment
ΔE_Q	Mössbauer quadrupole splitting
δ_{IS}	Mössbauer isomer shift
Å	angstrom unit (1 Å = 10^{-8} cm)
$\mathcal{A}$	atomic number
A	isotropic nuclear hyperfine splitting constant
$\mathbf{A}$	nuclear hyperfine tensor
A(H)	absorption shape function for powder systems
ca.	approximately
D	axial zero-field splitting parameter
DMSO-d_6	deuterated dimethylsulphoxide
E	rhombic zero-field splitting parameter
ESR	Electron Spin Resonance
g	electronic g-factor
G	magnetic field strength in gauss
GHz	gigahertz in cycles per second

H	magnetic field strength
$\mathbf{H}$	magnetic field vector
HS	high-spin
Hz	Hertz in cycles per second
H_z	magnetic field along z-direction
I	nuclear spin angular momentum quantum number
$\mathbf{I}$	nuclear spin angular momentum vector
$I(t \sim \infty)$	intensity after a long time
I(t)	intensity at time = t
ISC	intersystem crossing
J	resultant angular momentum quantum number
K	absolute temperature in degrees Kelvin
L	orbital angular momentum quantum number
LIESST	Light-Induced Excited Spin State Transition
LS	low-spin
m.p.	melting point
MHz	megahertz in cycles per second
M_I	nuclear spin magnetic quantum number
mmol	millimole
M_s	electronic spin magnetic quantum number
mW	milliwatt power
nm	wavelength unit in nanometer (10^{-9} m)
NMR	Nuclear Magnetic Resonance
O_h	octahedral crystal field symmetry
Q-band	microwave frequency range 33 - 56GHz
Q-factor	quality factor of resonator
S	electron spin angular momentum quantum number
$\mathbf{S}$	electronic spin angular momentum vector
T	magnetic field strength in Tesla (1T = 10^4 G)

T^*	corrected temperature
T_c	critical temperature
VT	variable temperatures
W-band	microwave frequency range 80 - 120GHz
X-band	microwave frequency range 8 - 12GHz
$\mathcal{Z}$	atomic mass number

CHAPTER 1

THEORY OF ELECTRON SPIN RESONANCE

1.1 Introduction

Electron spin resonance spectroscopy measures the allowed magnetic dipole transitions within a group of energy levels of the lowest ground electronic state in the presence of an externally applied static magnetic field. Classically, the energy of interaction between a magnetic dipole $\boldsymbol{\mu}$ and the externally applied static magnetic field **H** is expressed as

$$E = -\boldsymbol{\mu}\cdot\mathbf{H} = -\mu H\cos\theta \qquad (1.1.1)$$

where θ is the angle between $\boldsymbol{\mu}$ and **H**. Although the classical description allows the angle θ to assume any value between 0 and 2π, electrons and nuclei obey quantum rather than classical mechanics. In quantum mechanics, when an electron is placed in a static magnetic field, the magnetic moment $\boldsymbol{\mu}_e$ of the electron is given by the expression

$$\boldsymbol{\mu}_e = -\,g\beta_e\mathbf{S} \qquad (1.1.2)$$

where **S** is the intrinsic angular momentum in units of $\hbar$ associated with the electron, β_e is the Bohr magneton and g is a dimensionless constant commonly called the electronic g-factor. $\hbar$ is equal to the Planck constant h divided by 2π and it has a value of 1.05459×10^{-34} Js, β_e has a value of 9.2741×10^{-24} JT^{-1} and g has a value of 2.00232 for a free electron. The energy of interaction between $\boldsymbol{\mu}_e$ and **H** is analogously expressed as

$$E = -\boldsymbol{\mu}_e\cdot\mathbf{H} = g\beta_e\mathbf{S}\cdot\mathbf{H} \qquad (1.1.3)$$

Quantum mechanically, this energy of interaction is described in terms of the spin Hamiltonian operator

$$\hat{\mathcal{H}} = g\beta_e \hat{\mathbf{S}} \cdot \mathbf{H} \tag{1.1.4}$$

where $\hat{S}$ is electronic spin angular momentum operator. This is the Zeeman interaction between the electron spin and the magnetic field. When **H** is directed along a given direction, say the z-axis, of the Cartesian coordinate system, the Zeeman interaction has the form

$$\hat{\mathcal{H}} = g\beta_e H_z \hat{S}_z \tag{1.1.5}$$

For a system with a total electronic spin S, there exist a number of energy states defined by the electronic magnetic quantum number M_s. M_s can have values S, (S − 1),..., 0,..., −(S − 1), −S for integral value of S and S, (S − 1),..., $\frac{1}{2}$, $-\frac{1}{2}$,..., −(S − 1), −S for half-integral value of S. The total number of possible M_s values is (2S + 1), and the selection rule for the allowed transitions is $\Delta M_s = \pm 1$. Each energy state is characterized by a spin function $|S, M_s\rangle$ and the energy of a state is given by

$$E = g\beta_e H_z M_s \tag{1.1.6}$$

For an electron with S = $\frac{1}{2}$, the two energy states are thus

$$E = \pm \tfrac{1}{2} g\beta_e H_z \tag{1.1.7}$$

which correspond to the two possible orientations of the electronic spin in the magnetic field along the chosen z-axis. Absorption of microwave energy is allowed by the selection rule, and when the microwave energy is equal to the energy separation between the two spin states

$$h\nu = g\beta_e H_z \tag{1.1.8}$$

where ν is the frequency of radiation, h is the Planck constant and it has a value of 6.6262×10^{-34} Js. Equation (1.1.8) is the basic condition for ESR to occur, and it is valid to use in the study of other spin systems with $S > \frac{1}{2}$. By substituting the numerical values for h and β_e, the following simple relationship can be obtained

$$g = 714.484\left(\frac{\nu}{H}\right) \tag{1.1.9}$$

where ν is the microwave frequency in GHz, H is the resonance field in Gauss and g may be regarded as equivalent to the chemical shift δ normally reported in NMR studies. In ESR studies, it is a common practice to keep the frequency ν constant while monitoring the variation of the magnetic field H. In the case of a resonance field of 3400G, the frequency is found to be 9.5GHz, which is in the X-band of the microwave region. The microwave quantum energy is 0.3 cm^{-1}.

An X-band ESR spectrometer is the most commonly used and commercially available instrument, it has a wide application[1-11] in many fields of research, in physics, chemistry, biology and medicine, it can also be used as a routine analytical instrument. The next most commonly used is probably the Q-band ESR spectrometer which has a microwave frequency of *ca.* 35GHz, it is also commercially available. ESR spectrometers that operate at higher microwave frequencies are very expensive, they are usually built by individual research groups for specialized purposes. The W-band ESR spectrometer[12] constructed at the Illinois ESR Research Center has a microwave frequency of *ca.* 95GHz. One of the many advantages of performing ESR studies at higher microwave frequencies is the potential for much better spectral resolution, especially the g resolution. It can be seen easily from equation (1.1.9) that the difference in resonance field is proportional to the microwave frequency of resonance, hence the resolution of the ESR signal at Q- and W-bands will be 3.7 and 10 times better than at X-band, respectively, providing the signal linewidths do not increase.

1.2 Crystal Field Splitting

The effect of crystal field on a d-transition metal ion is to lift the degeneracy of the five d-orbitals, causing them to split in the way depending upon the strength of the field Δ. The result is a quenching or partial quenching of the orbital angular momentum associated with the unpaired electrons. In the presence of an octahedral crystal field, the five degenerate orbitals are split into three lower t_{2g} and two upper e_g levels. The energy separation between the two levels is determined by the type and nature of the ligands bonded to the metal ion. Typical energy separation between them is of the order of 10^4 cm^{-1}. Further splitting of the three lower t_{2g} orbitals may occur at a lower crystal field symmetry, such as a tetragonal distortion. The detailed quantitative treatment of the effect of a crystal field of different strength on d-transition metal ions having different orbital states can be found elsewhere[13-18].

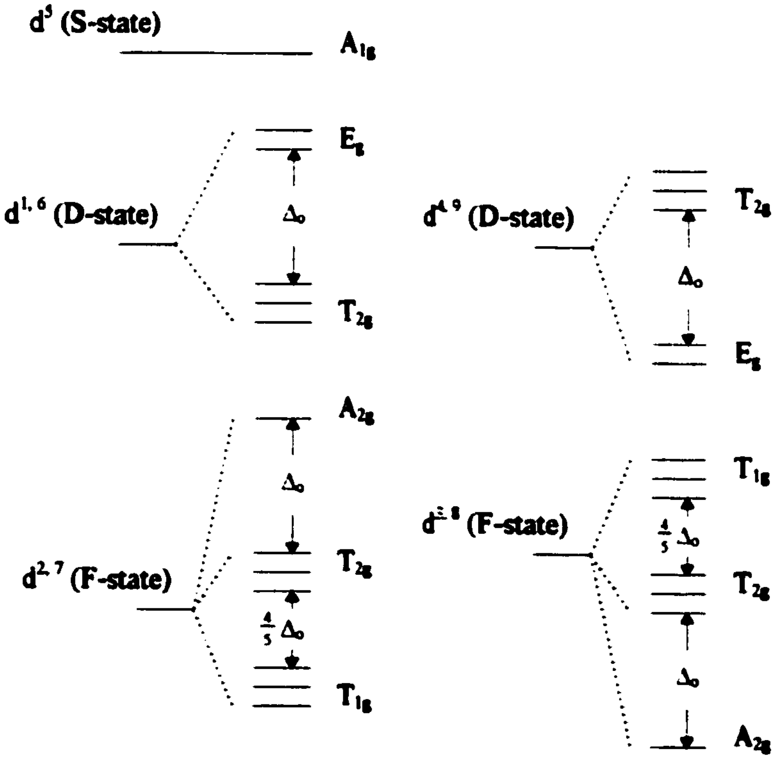
d^5 (S-state)
A_{1g}
$d^{1,6}$ (D-state)
E_g
Δ_o
T_{2g}
$d^{4,9}$ (D-state)
T_{2g}
Δ_o
E_g
$d^{2,7}$ (F-state)
A_{2g}
Δ_o
T_{2g}
$\frac{4}{5}\Delta_o$
T_{1g}
$d^{3,8}$ (F-state)
T_{1g}
$\frac{4}{5}\Delta_o$
T_{2g}
Δ_o
A_{2g}

Figure 1.2.1 Energy levels for d^n configurations in an octahedral crystal field.

There are only three types of orbital states in the first transition metal series. They are labeled as S-, D- and F-states, and their corresponding d^n electronic configurations are d^5, $d^{1,4,6,9}$ and $d^{2,3,7,8}$, respectively. The splitting pattern of the energy levels for various d^c configurations in an octahedral crystal field is shown schematically in figure 1.2.1. In both the d^1 and d^6 configurations, the electrons find the t_{2g} orbitals lowest in energy because they are kept away from the negative charges along the x, y and z axes. The d^4 and d^9 configurations can be regarded as having a positive hole in the d-shell, and this positive hole finds the e_g orbitals to be most stable because the electrons are concentrated along the x, y and z axes. Therefore both d^4 and d^9 configurations have their energy levels reversed from that of d^1 and d^6. The arrangement of energy levels for F-state ions can be understood in a qualitative way with the aid of Hund's rule. In the d^2 configuration, there are three possible ways of distributing the two electrons in two different t_{2g} orbitals of the lowest energy state. Therefore the ground state is triply degenerate, and both d^2 and d^7 should have the energy levels arranged as shown in figure 1.2.1. In the d^3 configuration, the ground state is nondegenerate because there is only one way to distribute three electrons into the three t_{2g} orbitals. Hence d^3 and d^8 have the energy levels arranged as shown in the figure.

1.3 Spin-Orbit Coupling

A single electron in a free d-transition metal ion has its electronic spin closely associated with the orbital angular momentum, the interaction between them gives rise to spin-orbit coupling which can be expressed as

$$\hat{\mathcal{H}}_{so} = \xi \hat{\ell} \cdot \hat{s} \tag{1.3.1}$$

where ξ is a measure of the strength of interaction between the spin and orbital angular momentum of the electron, $\hat{\ell}$ and $\hat{s}$ are the respective orbital and spin angular momentum operators. For the many electron case, the expression has the form

$$\hat{\mathcal{H}}_{so} = \lambda \hat{\mathrm{L}} \cdot \hat{\mathrm{S}} \tag{1.3.2}$$

where λ is the spin-orbit coupling constant, it has a positive value for a less than half-filled d-shell and a negative value for a more than half-filled shell, $\hat{L}$ and $\hat{S}$ are then the total orbital and spin angular momentum operators, respectively. In most d-transition metal complexes, except high-spin Mn^{2+}, the crystal field is incapable of completely quenching the orbital angular momenta of the electrons. This gives rise to a coupling between the electron spins and the residual orbital angular momenta, and one of the results is the deviation of the observed g-values from that of the free electron. This has been shown[15,18,19] in the case of Ti^{3+} ion in a tetragonally distorted O_h field. The arrangement of the energy levels for the system is schematically given in figure 1.3.1.

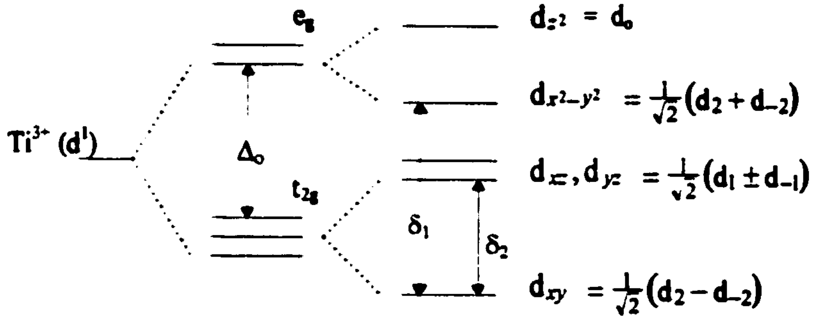
Ti^{3+} (d^1)
e_g
Δ_o
t_{2g}
δ_1
δ_2
$d_{z^2} = d_0$
$d_{x^2-y^2} = \frac{1}{\sqrt{2}}(d_2 + d_{-2})$
$d_{xz}, d_{yz} = \frac{1}{\sqrt{2}}(d_1 \pm d_{-1})$
$d_{xy} = \frac{1}{\sqrt{2}}(d_2 - d_{-2})$

Figure 1.3.1 Schematic representation of energy levels for d^1 ion in distorted O_h field.

The ground state wave functions are expressed in the form

$$\Psi_o = d_{xy}\alpha \qquad (1.3.3)$$
$$\Psi_o = d_{xy}\beta$$

where α and β correspond to the two possible M_s values of $+\frac{1}{2}$ and $-\frac{1}{2}$, respectively. Upon the application of the $\hat{\mathcal{H}}_{so}$ as a small perturbation to the system, these wave functions then become

$$\Psi(+) = d_{xy}\alpha - \frac{\lambda}{\delta_1}d_{x^2-y^2}\alpha + \frac{\lambda}{\sqrt{2}\delta_2}d_{-1}\beta \tag{1.3.4}$$

$$\Psi(-) = d_{xy}\alpha + \frac{\lambda}{\delta_1}d_{x^2-y^2}\beta - \frac{\lambda}{\sqrt{2}\delta_2}d_{1}\alpha$$

The effect of spin-orbit coupling is to mix in the ground state wave functions with certain excited state wave functions, and the energy obtained after solving the secular determinant ignoring second and higher order terms is given as

$$E = \pm\frac{1}{2}g_{eff}\beta_e H \tag{1.3.5}$$

where

$$g_{eff} = \sqrt{g_{\parallel}^2\cos^2\theta + g_{\perp}^2\sin^2\phi} \tag{1.3.6}$$

and

$$g_{\parallel} = g_e - \frac{8\lambda}{\delta_1} \tag{1.3.7}$$

$$g_{\perp} = g_e - \frac{2\lambda}{\delta_2}$$

g_e is equal to 2.00232.

In the Fe^{2+} system, spin-orbit coupling may split the $^5T_{2g}$ ground electronic state into a total of fifteen levels which are so close to each other giving rise to a very large zero-field splitting and a very short relaxation time. Therefore, the ESR of most Fe^{2+} complexes is very difficult, if not impossible, to be observed at room temperature. In general, very low temperatures, such as liquid helium or hydrogen temperatures, are often required to observe Fe^{2+} ESR. The present ESR studies of Fe^{2+} spin crossover complexes are done by doping the complexes with the Mn^{2+} ion which serves as a probe to monitor the behavior of the crystal field. The use of Mn^{2+} ion as a probe in various host lattices in a variety of ESR studies has been thoroughly reviewed[20,21]. It has to be noted that the phenomenon of spin-orbit coupling is practically unimportant in the Mn^{2+} case. Since Mn^{2+} is an S-state ion which does not split in the crystal field, and all the excited states are far removed from the $^6A_1$ ground state and have a different spin, giving rise to a very small change in the g values.

1.4 g-factor

The basic resonance condition of equation (1.1 8) introduces the g-factor as a single parameter, assuming that the system is isotropic and there is no orbital contribution to μ_e. For a free transition metal ion, g can be expressed as

$$g = 1 + \frac{S(S+1) - L(L+1) + J(J-1)}{2J(J+1)} \tag{1.4.1}$$

where S is the total electronic spin angular momentum quantum number, L is the total orbital angular momentum quantum number and J is the resultant angular momentum quantum number. The possible values of J range from L + S to |L - S| in integral steps. In the absence of an orbital contribution, g is equal to 2.0. For most d-transition metal complexes, g is highly dependent upon the environment of the metal ion and the actual value will depend on the orientation of the molecule with respect to the applied magnetic field **H**. In a magnetically diluted system, the electronic Zeeman interaction is expressed in terms of the symmetric g-tensor which is characterized by three mutually orthogonal principal values g_{xx}, g_{yy} and g_{zz}. The relationship between these g-values is determined by the point symmetry at the metal ion. For a metal ion in a field of O_h or T_d symmetry, $g_{xx} = g_{yy} = g_{zz}$ and the system is isotropic. It is generally true that molecules with the above geometry will give isotropic g-values but the reverse is not necessarily true. It is possible for a molecule with no symmetry elements to give three g-values so close together that experimentally they cannot be resolved, especially when the experiment is done at low microwave frequencies. Isotropic ESR spectra of d-transition metal complexes are usually observed in dilute solutions. It is essential that the molecules are tumbling much more rapidly than the time scale of the experiment so that any anisotropy is averaged. A single crystal of low symmetry will have $g_{xx} \neq g_{yy} \neq g_{zz}$, the deviation of these g-values from the free electron value of 2.00232 is a measure of the contribution from the orbital angular momentum of the electron. At any orientation of the **H** with respect to all principal axes of the g-tensor, the effective g-value of the system can be expressed as

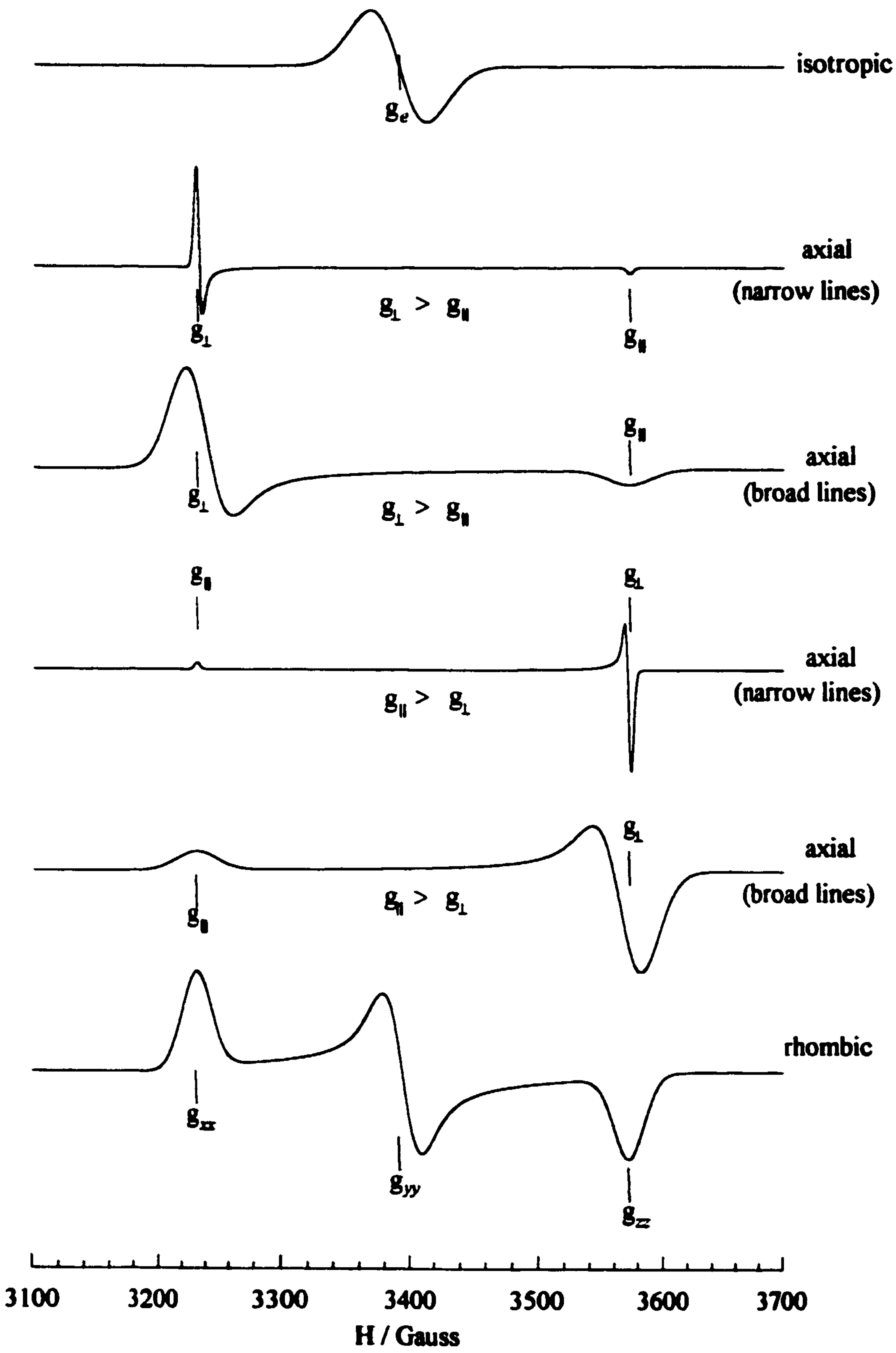

Figure 1.4.1 Computer-simulated powder ESR spectra with different principal g-values as indicated.

$$g^2 = g_{zz}^2\cos^2\theta + g_{xx}^2\sin^2\theta\cos^2\phi + g_{yy}^2\sin^2\theta\sin^2\phi \qquad (1.4.2)$$

where θ and ϕ are the polar angles of **H** with respect to the principal axes of the g-tensor. For a system with axial symmetry, the effective g-value as given in equation (1.4.2) becomes

$$g^2 = g_\parallel^2\cos^2\theta + g_\perp^2\sin^2\theta \qquad (1.4.3)$$

where $g_\parallel = g_{zz}$, $g_\perp = g_{xx} = g_{yy}$ and $g_\parallel \neq g_\perp$. In a powder or glass system with axial g-values, the resonance field range for the paramagnetic ion is determined by $g_\parallel$ and $g_\perp$. A powder ESR spectrum has an unusual shape which is basically the envelope of all possible orientations of the molecule with respect to **H**. Various representative powder ESR spectra having different principal g-values are given in figure 1.4.1.

1.5 Nuclear Hyperfine Splitting

This arises from the interaction of a magnetic nucleus and the unpaired electrons. Some nuclei possess intrinsic nuclear spin angular momentum I, the value of I depends on the atomic number $\mathcal{A}$ and the atomic mass number $\mathcal{Z}$. I will have a zero value when both $\mathcal{A}$ and $\mathcal{Z}$ are even numbers. When $\mathcal{A}$ is an odd or even number and $\mathcal{Z}$ is odd, I will have half integral values. When $\mathcal{A}$ is an odd number and $\mathcal{Z}$ is even, I will have integral values. For half integral values of I, the nuclear spin magnetic quantum number M_I has values I, I - 1, .., $\frac{1}{2}$, $-\frac{1}{2}$, .., -(I - 1), -I. For integral values of I, M_I can have values I, I - 1, ..,0 .., -(I - 1), -I. The total number of possible M_I values is (2I + 1).

The interaction between the nuclear spin and the total electron spin can be expressed as

$$\hat{\mathcal{H}}_{\mathrm{SI}} = \hat{\mathcal{H}}_{\mathrm{dipolar}} + \hat{\mathcal{H}}_{\mathrm{Fermi}} \qquad (1.5.1)$$

The first dipolar term has the form

$$\hat{\mathcal{H}}_{\text{dipolar}} = -g_e g_N \beta_e \beta_N \left[\frac{\hat{S}\cdot\hat{I}}{r_{ij}^3} - \frac{3(\hat{S}\cdot r_{ij})(\hat{I}\cdot r_{ij})}{r_{ij}^5} \right] \tag{1.5.2}$$

where g_e and g_N are the electronic and nuclear g-values, β_e and β_N are the respective electronic and nuclear magnetic moments, and r_{ij} is the distance between the electrons and the nucleus. The dipolar interaction is generally used to account for anisotropic systems when the nuclear hyperfine splittings are characterized by the hyperfine tensor **A**. For an anisotropic system with $I = S = \frac{1}{2}$, **A** can be expressed in terms of the spherical polar coordinates as

$$\mathbf{A} = \begin{bmatrix} \frac{1-3\sin^2\theta\cos^2\phi}{r^3} & -\frac{3\sin^2\theta\sin\phi\cos\phi}{r^3} & -\frac{3\sin\theta\cos\theta\cos\phi}{r^3} \\ -\frac{3\sin^2\theta\sin\phi\cos\phi}{r^3} & \frac{1-3\sin^2\theta\sin^2\phi}{r^3} & -\frac{3\sin\theta\cos\theta\sin\phi}{r^3} \\ -\frac{3\sin\theta\cos\theta\cos\phi}{r^3} & -\frac{3\sin\theta\cos\theta\sin\phi}{r^3} & \frac{1-3\cos^2\theta}{r^3} \end{bmatrix} \tag{1.5.3}$$

where θ and ϕ are the polar angles with respect to the molecular *x*, *y*, *z* axes.

The second Fermi contact term[22] has the form

$$\hat{\mathcal{H}}_{\text{Fermi}} = \left(\frac{8\pi}{3}\right) g_e g_N \beta_e \beta_N |\psi_0|^2 \hat{S}\cdot\hat{I} \tag{1.5.4}$$

where $|\psi_0|^2$ is the Dirac function which measures the electron density at the nucleus. This term operates only on s-orbitals, and it gives isotropic hyperfine splitting constants A in units of energy.

$$A = \left(\frac{8\pi}{3}\right) g_e g_N \beta_e \beta_N |\psi_0|^2 \tag{1.5.5}$$

In the study of Mn^{2+}-doped Fe^{2+} spin crossover complexes, the observed Mn^{2+} hyperfine splitting is primarily the result of the Fermi contact term. Since Mn^{2+} is an S-state ion, the hyperfine interaction is independent of the orientation of the ion with respect to the applied magnetic field. Typical hyperfine interaction energy for Mn^{2+} ion is of the order of 8×10^{-3} cm^{-1}.

1.6 Zero-Field Splitting Parameters

For a system with total a electronic spin $S \geq 1$, the interaction of the electron spins is given by the general expression

$$\hat{\mathcal{H}}_{ss} = g_e^2 \beta_e^2 \sum_{j>i} \left[\frac{\hat{s}_i \cdot \hat{s}_j}{r_{ij}^3} - \frac{3(\hat{s}_i \cdot \mathbf{r}_{ij})(\hat{s}_j \cdot \mathbf{r}_{ij})}{r_{ij}^5} \right] \qquad (1.6.1)$$

where g_e and β_e are the respective electronic g-value and magnetic moment, $\hat{s}_i$ and $\hat{s}_j$ are the electronic spin angular momentum operators for the ith and jth electrons, respectively, and r_{ij} is the distance between the two electrons i and j. The effect of the interaction is to further split the ground electronic state into a number of levels in the absence of an applied magnetic field **H**. The separation of these energy levels is characterized by two parameters D and E, commonly referred to as the zero-field splitting parameters. D is usually called the axial zero-field splitting parameter, E is called the rhombic zero-field splitting parameter, and they are both regarded as a measure of the distortion of the system from O_h symmetry. In triplet state organic molecules, the main contribution to the zero-field splitting is due to the dipolar electronic spin-spin interaction of the two unpaired electrons. However, in transition metal ions the major contribution to the zero-field splitting is due to the spin-orbit coupling of the ground state with certain excited states. For an S = 1 system, the result of zero-field splitting is a separation of the energy levels characterized by $M_s = 0$ and $M_s = \pm 1$. When **H** is along the z axis, these energy levels are given[18] as

$$\varepsilon(M_s = \pm 1) = \tfrac{1}{3}D \pm \sqrt{g_e^2\beta_e^2 H_0^2 + E^2} \qquad (1.6.2)$$

$$\varepsilon(M_s = 0) = -\tfrac{2}{3}D$$

where $H_o = \frac{h\nu}{g_e\beta_e}$ is the resonance field for the allowed $(M_s - 1) \rightarrow M_s$ transition when **H** is along the *z* axis. This situation is schematically illustrated as in figure 1.6.1.

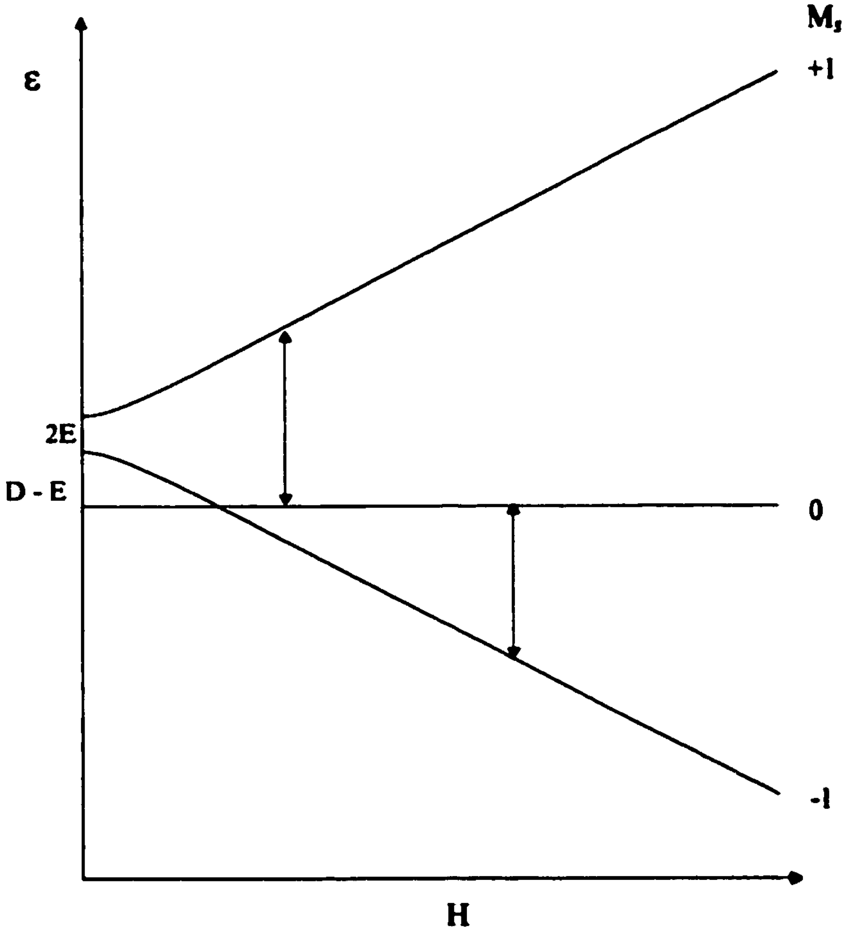

Figure 1.6.1 Schematic energy level diagram showing the zero-field splitting for an S = 1 system with **H** along the *z* axis.

It should be noted that in some metal ions, such as Fe^{2+}, the effect of zero-field splitting may give rise to a large number of spin states with very short lifetimes for the ESR to be experimentally observed. In the Mn^{2+} system with $S = I = \frac{5}{2}$, the spin sextet is split as a result of the very small zero-field effect and the five allowed (M_s - 1) to M_s transitions are observed. The zero-field splitting pattern of Mn^{2+} ion in O_h symmetry is shown in figure 1.6.2.

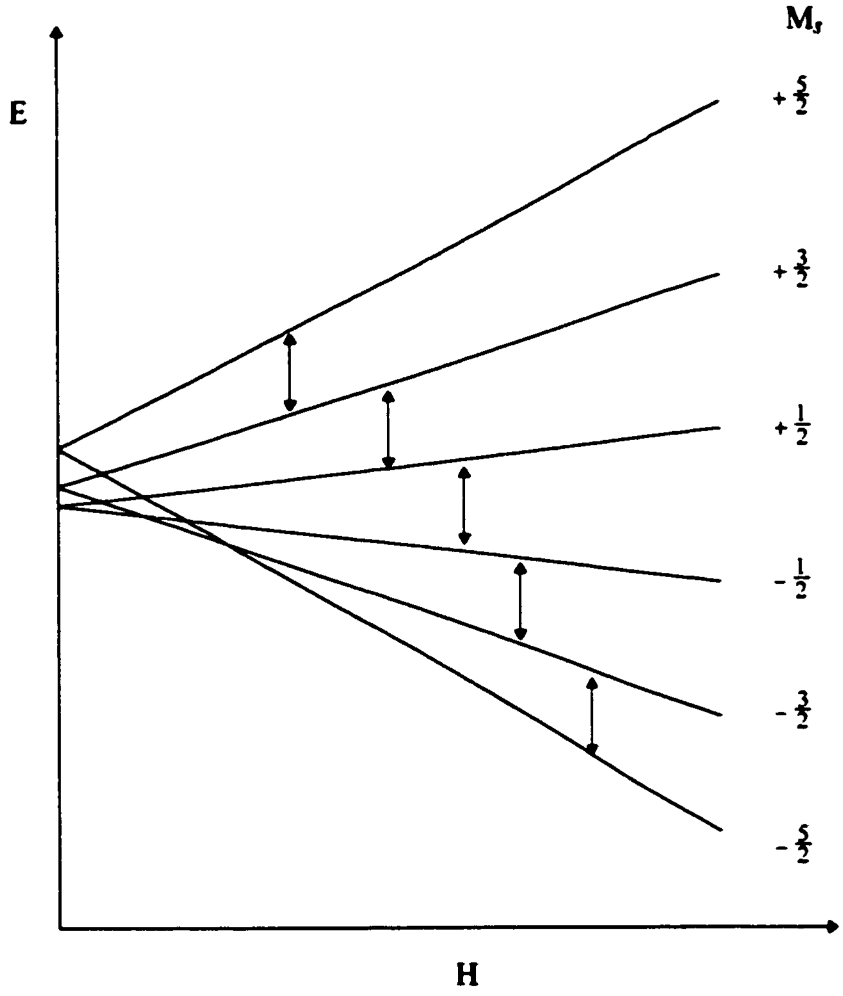
E
M_s
$+\frac{5}{2}$
$+\frac{3}{2}$
$+\frac{1}{2}$
$-\frac{1}{2}$
$-\frac{3}{2}$
$-\frac{5}{2}$
H

Figure 1.6.2 Schematic diagram showing zero-field splitting of high-spin Mn^{2+} ion in strong magnetic field.

1.7 ESR Spectrum of Mn^{2+} Ion

The main features of Mn^{2+} ESR spectrum can be interpreted with the use of the spin Hamiltonian given[16,18] by

$$\hat{\mathcal{H}} = g\beta_e\hat{S}\cdot\mathbf{H} + D\left(\hat{S}_z^2 - \tfrac{35}{12}\right) + E\left(\hat{S}_x^2 - \hat{S}_y^2\right) + A\hat{S}\cdot\hat{I}$$
$$+ \tfrac{1}{6}a\left(\hat{S}_x^4 + \hat{S}_y^4 + \hat{S}_z^4 - \tfrac{707}{16}\right) + \tfrac{1}{180}F\left(35\hat{S}_z^4 - \tfrac{475}{2}\hat{S}_z^2 + \tfrac{3255}{16}\right) \qquad (1.7.1)$$

where g is the electronic g-value, A is the hyperfine splitting for the stable ^{55}Mn isotope, D, E, a and F are the fine structure terms. Experimentally g is isotropic and very close to 2, A is isotropic, a is usually much smaller than D which in turn is generally much smaller than the Zeeman interaction, and F is practically negligible. The term in a involving S to the fourth order is non-zero even in octahedral or tetrahedral symmetry. The term F is non-zero when there is an axial distortion, it is sometimes needed to give a better agreement with the observed spectrum. The detailed discussion of equation (1.7.1) and the various spin Hamiltonian parameters can be found in many review articles[23-25]. The absorption energy for the $(M_s - 1) \rightarrow M_s$ transition has the form

$$h\nu\,(M_s) = g\beta_e H + \tfrac{1}{2}D\left[3\left(\frac{g_\parallel}{g}\right)^2\cos^2\theta - 1\right](2M_s - 1)$$
$$- \frac{D^2}{2g\beta_e H}\left(\frac{g_\parallel g_\perp}{g^2}\right)^2 \sin^2\theta\cos^2\theta\left[4S(S+1) - 24M_s(M_s - 1) - 9\right]$$
$$+ \frac{D^2}{8g\beta_e H}\left(\frac{g_\perp}{g}\right)^4 \sin^4\theta\left[2S(S+1) - 6M_s(M_s - 1) - 3\right] \qquad (1.7.2)$$

where g is given by equation (1.4.3) and fourth-order terms are omitted. Equation (1.7.2) was first obtained by Bleaney[26] in 1951, and it is applicable to any spin system S that obeys the spin Hamiltonian given by

$$\hat{\mathcal{H}} = g_\parallel\beta_e H_z\hat{S}_z + g_\perp\beta_e\left(H_x\hat{S}_x + H_y\hat{S}_y\right) + D\left[\hat{S}_z^2 - \tfrac{1}{3}S(S+1)\right] + E\left(\hat{S}_x^2 - \hat{S}_y^2\right) \qquad (1.7.3)$$

To a first-order approximation, the spectrum consists of five $\Delta M_s = \pm 1$ resonance lines separated by $\tfrac{1}{2}D\left[3\left(\frac{g_\parallel}{g}\right)^2\cos^2\theta - 1\right](2M_s - 1)$ from the center line at $g\beta_e H$ for the

$M_s = -\frac{1}{2} \rightarrow M_s = +\frac{1}{2}$ transition. The effect of the second-order terms is to displace the resonance lines from the center value of $g\beta_e H$. If the system has a very large D value, such that $D \gg g\beta_e H$, the resonance lines of the allowed transitions may spread over a very wide magnetic field range causing some of them to be experimentally unobservable. The detailed analysis of an experimental Mn^{2-} ESR spectrum is given in section 4.6.

1.8 Powder ESR Spectra

Although single crystal experiments allow the maximum information to be extracted from the ESR spectrum, it is possible to obtain the spin Hamiltonian parameters from powders. The powder method of analysis has been used and discussed[18,27-31] in detail for different spin systems.

For an $S = \frac{1}{2}$ system having axial symmetry and no hyperfine interaction, the absorption shape function A(H) expressed in terms of the applied magnetic field H is given[18] as

$$A(H) = \frac{1}{2}\frac{h^2 \nu_0^2}{\beta_e^2 H^3}\left(g_\parallel^2 - g_\perp^2\right)^{-\frac{1}{2}}\left(\frac{h^2 \nu_0^2}{\beta_e^2 H^2} - g_\perp^2\right)^{-\frac{1}{2}} \qquad (1.8.1)$$

where ν_o is the frequency of the spectrometer. This function was derived assuming that the paramagnetic ion has an infinitely sharp absorption, and it can be shown that the absorption profile has a large sharp absorption at $H = \frac{h\nu_0}{g_\perp \beta_e}$ and a small sharp cutoff at $H = \frac{h\nu_0}{g_\parallel \beta_e}$. The first derivative of the absorption curve is shown by the second computer-simulated powder ESR spectrum given in figure 1.4.1. The value of $g_\perp$ is obtained from the location of the large peak and $g_\parallel$ from the location of the small peak. The detailed treatment of how to obtain the three principal g-values from the powder absorption curve with $g_{xx} \neq g_{yy} \neq g_{zz}$ has been given by Kneubühl[31].

The absorption profile becomes more complex when there is hyperfine interaction, and the resulting ($2M_I + 1$) absorption curves are usually superimposed on each other. It has to be noted that the spin Hamiltonian parameters obtained from a powder spectrum cannot be related to the molecular axis system, and their accuracy is less than that for a single crystal.

CHAPTER 2

GENERAL FEATURES OF SPIN CROSSOVER COMPLEXES

2.1 Spin Crossover Phenomenon

In the first transition metal series, there are two possible ground states for the octahedral (O_h) complexes with d^4, d^5, d^6 and d^7 electronic configurations. The formation of the so called high-spin (HS) or low-spin (LS) ground states is dependent upon the relative strength of the ligand field Δ and the mean spin-pairing energy Π of the system. HS ground states are formed in weak field systems when $\Delta < \Pi$, whereas LS ground states become favourable in strong field systems when $\Delta > \Pi$. It is only when $\Delta \approx \Pi$ where HS and LS ground states may be interconvertible with the result that both ground states may be thermally populated. The energy difference between the ground states becomes so small that a change of ground state may occur under the influence of an external variable such as temperature or pressure. There is also a change in the total electron spin during the conversion between the two ground states. This phenomenon is often called spin crossover or spin-state transition. In the case of an Fe^{2+} system, as shown in figure 2.1.1, the crossover from the HS($^5T_{2g}$) ground state to the LS($^1A_{1g}$) ground state is accompanied by a change in the total electron spin from $S = 2$ to $S = 0$.

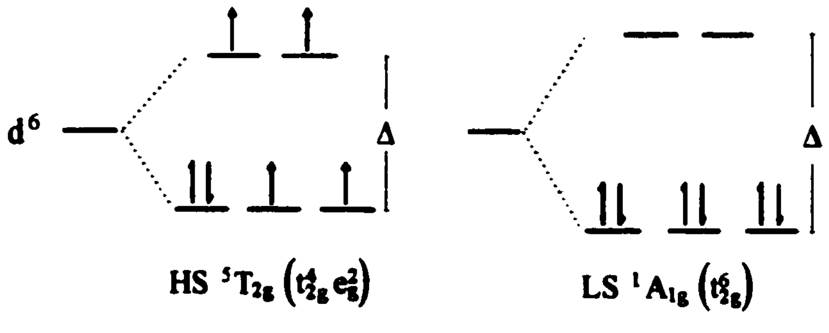

Figure 2.1.1 Electronic configurations of HS and LS ground states of Fe^{2+} (d^6) system in O_h symmetry.

Term symbols, arising from group theoretical considerations, are commonly used to designate the spin states and this practice will be followed below. Ground state terms for the d^4 to d^7 configurations in O_h symmetry are given in Table 2.1.1, a thorough treatment of the subject can be found elsewhere[13,14,32]. Values of Π for the aforementioned configurations have been calculated and reported by König and Kremer[33] in 1971.

Table 2.1.1 Ground States for d^4 to d^7 Configurations

d^n	Weak Field	Strong Field
d^4	^5E_g	$^3T_{1g}$
d^5	$^6A_{1g}$	$^2T_{2g}$
d^6	$^5T_{2g}$	$^1A_{1g}$
d^7	$^4T_{1g}$	^2E_g

A thermally-induced crossover of the HS and LS ground states, HS↔LS, is essentially a solid-state phenomenon. The critical temperature T_c is defined when both the HS and LS ground states have the same thermal population. It then follows that the relative stability of the HS and LS ground states depends on the standard free energy change ΔG° of the system

$$\Delta G^\circ = \Delta H^\circ - T\Delta S^\circ \qquad (2.1.1)$$

where ΔH° is the standard enthalpy change and ΔS° is the standard entropy change of the system. Since it is known from thermodynamics that

$$\Delta G^\circ = -RT \ln K \qquad (2.1.2)$$

where K is the equilibrium constant, R and T are the gas constant and the temperature, respectively. The critical temperature T_c is defined to be the one when K becomes unity. T_c is therefore given by the expression

$$T_c = \frac{\Delta H^\circ}{\Delta S^\circ} \tag{2.1.3}$$

In all Fe^{2+} systems measured[40,51-54,68,72,74], so far, the HS ground states are more stable at temperatures above T_c whereas LS ground states are more stable at temperatures below T_c. X-ray diffraction studies[34-42] have shown that the average metal-ligand bond length is longer in HS ground state than in the LS ground state. The difference is about 0.17Å for Fe^{2+} complexes, 0.13Å for Fe^{3+} complexes and 0.06Å for Co^{2+} complexes. A change in crystallographic phase has also been observed in some Fe^{2+} systems during the HS $\leftrightarrow$ LS crossover.

2.2 Magnetic Property

There are two types of magnetic behavior commonly observed in spin crossover complexes, they are shown schematically in figure 2.2.1. The first type has a discontinuous HS $\leftrightarrow$ LS crossover over a narrow temperature range, such systems have an abrupt change of the effective magnetic moment μ_{eff} with temperature. The second type has a continuous HS $\leftrightarrow$ LS crossover over an extended temperature range, such systems show a gradual change of μ_{eff} with temperature. Thermal hysteresis may occur in both discontinuous and continuous types of system, this is shown in figure 2.2.2. The conversion from HS $\rightarrow$ LS ground states will follow the descending path I with a unique critical temperature $T_c^{\downarrow}$, the reverse conversion from LS $\rightarrow$ HS ground states will follow the path II with a unique $T_c^{\uparrow}$. The two paths, I and II, form a closed loop which is independent of the rate of change of temperature. The difference between the critical temperatures may vary from a few tenth of a degree to sometimes over a hundred degrees.

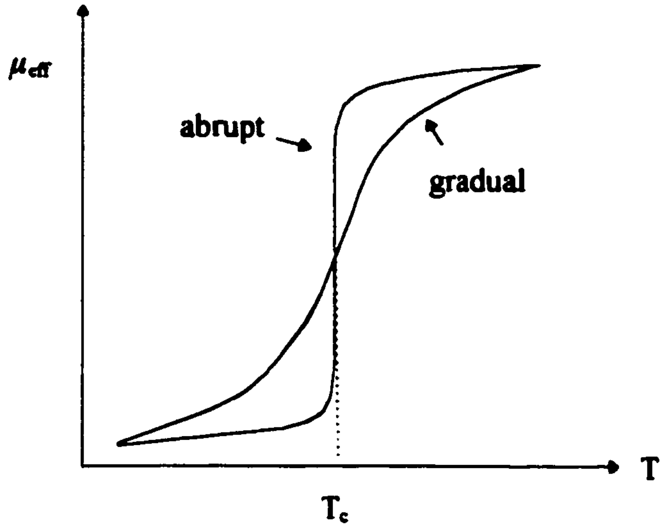

Figure 2.2.1 Schematic representation of discontinuous and continuous types of HS ↔ LS crossover.

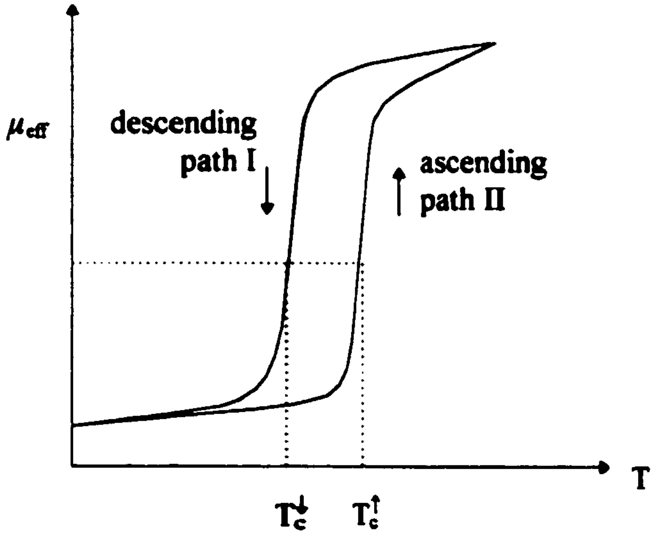

Figure 2.2.2 Thermal hysteresis effect.

Hysteresis effects are closely associated with the formation of domains[40] during HS ↔ LS crossover. This has been shown[40,43] to occur in many Fe^{2+} spin crossover systems. It has been shown[40] that, in general, the discontinuous type of HS ↔ LS crossover is followed by a change of the crystallographic phase of the system. ESR studies[44] have shown that, in $[Fe(ptz)_6][BF_4]_2$ complex, the crystalline phase transformation is driven by the HS ↔ LS crossover. Both the HS ↔ LS and first-order phase changes are due to cooperative interactions between the individual HS and LS molecules.

2.3 Methods of Study

The temperature-dependent HS↔LS crossover of Fe^{2+} systems has been studied by various physical methods. As can be seen in Table 2.1.1, the spin states for the ground states of all the spin crossover systems are different. Magnetic susceptibility measurements are very commonly used to establish the spin state of the ground state during HS↔LS crossover. The change from $^5T_{2g} \rightarrow {}^1A_{1g}$ or vice versa, as in an Fe^{2+} system, is accompanied by a change of μ_{eff} of the system. In all Fe^{2+} systems studied, so far, the existence of HS or LS ground states can be determined by ^{57}Fe Mössbauer spectroscopy. The identification of ground states is based on the fact that HS Fe^{2+} has a different isomer shift δ_{IS} and quadrupole splitting ΔE_Q from that of LS Fe^{2+}. Typical values[45-48] of δ_{IS} for the HS and LS Fe^{2+} in a spin crossover system are 0.7 - 1.7 mms^{-1} and -0.24 - 0.5 mms^{-1}, respectively. X-ray diffraction studies allow for the determination of structural phase changes during HS↔LS crossover. Heat capacity measurements[49,50] on the $[Fe(phen)_2][NCS]_2$ and $[Fe(phen)_2][NCSe]_2$ complexes have shown that the spin-state transition in the systems is cooperative in nature and it is coupled to the phonon system. The major phonon vibration is due to metal-ligand vibrations, and a small contribution from the lattice vibrations. Other methods such as electronic and vibrational spectroscopies, NMR and ESR have also been used. Most of these techniques have been discussed in several review articles[42,51-54].

All previous ESR studies[43,44,55-57] of Fe^{2+} spin crossover systems were done by following the spectral changes of Mn^{2+} ion doped into the sample. In all cases studied[43,44,55-57], so far, the amount of dopant used is less than 5 mole % which is the maximum quantity allowed by the system for not causing any appreciable dipolar broadening of the Mn^{2+} spectral lines. The reason for using Mn^{2+} in the ESR study of

Fe^{2+} spin crossover systems is simply due to the fact that Fe^{2+} ($S = 2$) has a very large zero-field splitting and a very short lifetime for its spin states and its ESR is difficult, if not impossible, to be experimentally observed. Mn^{2+} ion has a total electronic spin $S = \frac{5}{2}$, it is very sensitive to changes of its surrounding environment, and it monitors the crystal field directly via its spin Hamiltonian parameters D, E, *a* and F. It has a long spin-lattice relaxation time, can be doped into a host lattice easily, and its ESR spectrum is readily observed in HS and LS of the host Fe^{2+} lattice over a wide range of temperature. The presence of the impurity Mn^{2+} ion in an Fe^{2+} spin crossover system has also been shown[55] to have no effect on both the spin-state transition and the cooperative interaction between the HS and LS Fe^{2+} during the transition.

A vast amount of additional information concerning the nature and dynamics of spin crossover in different Fe^{2+} systems were provided by ESR technique. In the studies[55] of Mn^{2+}-doped powder samples of $[Fe(phen)_2][NCS]_2$ and $[Fe(2\text{-}pic)_3]Cl_2.EtOH$ complexes, no phase change was detected during the spin-state transition in these complexes. A separate study[56] of the latter system using Mn^{2+}-doped single crystals showed the existence of domains during spin-state transition in the system. The identification of domains was based on the results that at least three different types of Mn^{2+} spectra were seen in the temperature interval in which the spin crossover occurred, each type characterized by a unique set of zero-field splitting parameters and principal axes for the Mn^{2+} ion in the system. In the single crystal studies[43] of $[Fe(btr)_2][SeCN]_2.H_2O$ and $[Fe(btr)_2][SCN]_2.H_2O$ complexes, the spin-state transition was also seen to occur in domains rather than in a statistically random manner. The same study also showed a phase change had occurred during the spin-state transition. ESR studies[44] of both the Mn^{2+}- and Cu^{2+}-doped single crystals of $[Fe(ptz)_6][BF_4]_2$ complex detected the existence of two different structural phases I and II below the HS → LS transition temperature depending on the way the system was cooled. The diamagnetic phase I was obtained by fast cooling the system in liquid nitrogen, and no phase change was observed during the HS → LS transition. The diamagnetic phase II was obtained either by slow cooling the paramagnetic sample to 77K or by warming the diamagnetic phase I to a temperature slightly below that for the HS → LS transition, and a phase change was observed only in the slow cooling process. The spontaneous transformation from diamagnetic phase I to II at temperatures just below the HS → LS transition indicated that the structural phase change was driven by the spin-state transition in this system. The Mn^{2+}-doped single crystal studies[57] of two polymorphs A and B of the [Fe(BT)$_2$][NCS]$_2$ system showed that the HS ↔ LS transition occurred only in polymorph A. The spin-state transition occurred rapidly in powders but took over an hour in single crystals cooled rapidly to 77K. The HS → LS transition was accompanied by a phase change in the system and the crystals pulverized during the reverse LS → HS transition when warmed to room temperature. The same study also confirmed the cooperative nature of spin crossover in the system.

2.4 Light-Induced Excited Spin State Trapping (LIESST)

When certain Fe^{2+} spin crossover complexes are irradiated at low temperatures with light of suitable wavelengths, the LS → HS crossover may occur and the system will remain trapped in the HS ground state. This phenomenon is called light-induced excited spin state trapping (LIESST). The trapped HS ground states can be pumped back to the LS ground states by irradiating the system at low temperatures with light of different wavelengths, this is the reverse LIESST effect. The LIESST effects were first observed by Decurtins *et al.*[58,59] in their studies of [Fe(ptz)$_6$][BF$_4$]$_2$ complex at temperatures below 50K. The complex was discovered by Franke *et al.*[60] to exhibit an abrupt HS ↔ LS crossover with thermal hysteresis[61], the critical temperatures were determined as $T_c^{\downarrow} = 128K$ and $T_c^{\uparrow} = 134K$. The color of the complex changed from purple to white during LS → HS crossover. Extensive studies[62-68] of LIESST and the reverse LIESST effects in [Fe(ptz)$_6$][BF$_4$]$_2$ and other Fe^{2+} spin crossover systems have been done. A mechanism for the LIESST effects has been proposed[64] and fully interpreted[59,64,65] as shown by the schematic diagram in figure 2.4.1. The upward and wavy downward arrows indicate the possible pathways for the excitation and relaxation processes, respectively, in the system during the irradiation.

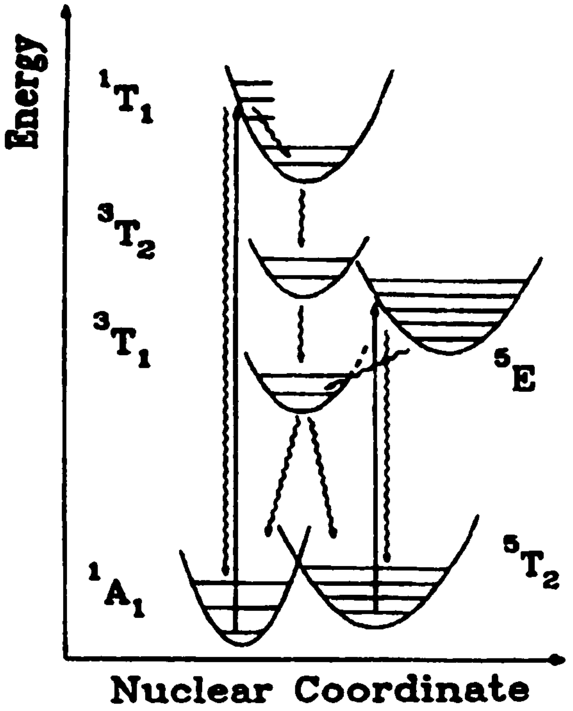

Figure 2.4.1 Schematic potential energy curves for the ground and excited states of a d^6 spin crossover system. This figure was modified from reference 64.

The irradiation of the LS ground state at temperatures much below T_c, using light of *ca.* 514 nm, leads to a population of the very short lived $^1T_1$ singlet state. Most of the ions in this excited singlet state decay back to the LS ground state. However, an alternative decay path to the lowest $^3T_1$ triplet state is possible, and from there either to the LS ground state or to the metastable HS ground state. The continuous pumping by laser irradiation results in complete conversion of the LS state to the metastable HS state. This process can occur in the opposite direction. The reverse process involves a pumping back of the system trapped in the HS ground state to the normal LS ground state, using light of *ca.* 800 nm corresponding to the $^5T_2 \rightarrow {}^5E$ transition. The formation of a metastable HS ground state may often be achieved thermally by rapidly cooling of the system from temperatures where the HS state is the stable ground state.

2.5 Effect of Pressure

It has been shown[69,70] that pressure induced HS ↔ LS crossover can occur in some Fe^{2-} systems under constant temperature. Fe^{2+} complexes involving phenanthroline, substituted-phenanthroline, bipyridyl and other anionic ligands such as Cl^-, Br^-, NCS^-, $NCSe^-$, NCO^-, N_3^- and CN^- have been studied at high pressure to 180 kbar using Mössbauer and Optical methods. The observed experimental results are explained in terms of the degree of back bonding between the metal t_{2g} orbitals and the ligand π^* orbitals. For a pressure induced HS → LS crossover, the effect of increasing pressure is to increase the ligand field strength Δ and to decrease the interelectronic repulsion (Racah) parameters[13,14,32,33]. The increase in Δ is the result of the increased electrostatic repulsion and the decrease in the Racah parameters is caused by an increase in the overlap of the metal and ligand electrons. For LS complexes at room temperature, the LS → HS crossover also occurs with increasing pressure. This is due to a decrease in the back donation of the metal t_{2g} electrons to the ligand π^* orbitals, the result is a decrease of Δ and an increase of the Racah parameters. A comprehensive review of the effect of pressure on the spin states of Fe^{2+} and other systems has been given by Drickamer and Frank[71].

CHAPTER 3

CHEMICAL SYNTHESIS AND ANALYSIS OF COMPLEXES

3.1 Materials and Chemicals

All chemicals used in the present studies were obtained from Aldrich Chemical Company. 2,6-Diacetylpyridine (99%), N,N-dimethylformamide dimethyl acetal (94%) and hydrazine hydrate were used to synthesize the 2,6-bis(pyrazol-3-yl) pyridine (bpp) ligand, they were used without further purification. Iron(II) chloride tetrahydrate (99.995%), manganese(II) chloride tetrahydrate (99.99%) and sodium trifluoromethansulfonate (98%) were used, without further treatment, in the preparation of Mn^{2+}-doped $[Fe(bpp)_2][CF_3SO_3]_2.H_2O$ complex. Iron(II) tetrafluoroborate hexahydrate (98%), manganese(II) carbonate (99.9%) and fluoroboric acid (48% solution in water) were used, without further treatment, in the preparation of Mn^{2+}-doped $[Fe(bpp)_2][BF_4]_2$ complex. 5-Nitrosalicyaldehyde (99%), sublimed prior to use, and 1,4,7,10-tetraazadecane (98%) were used to synthesize the $(5\text{-}NO_2\text{-sal-}N(1,4,7,10))^{2-}$ ligand. Iron(II) acetate (95%) and manganese(II) acetate tetrahydrate (99.99%) were used, without further treatment, in the preparation of Mn^{2+}-doped $[Fe(5\text{-}NO_2\text{-sal-}N(1,4,7,10))]$ complex. A Schlenk line was used in this synthesis. Methanol was distilled over MgO under nitrogen atmosphere. Elemental analysis of the synthesized compounds were done at the Guelph Chemical Laboratories Ltd. One dimensional ^1H NMR characterization of the bpp ligand dissolved in DMSO-d_6 was done using the Bruker AVANCE DPX 300 MHz NMR spectrometer. All samples used in ESR measurements were carefully sealed under vacuum in quartz tubes. The quartz tubes used were of the same quality as the type 707-SQ obtainable from Wilmad Glass.

3.2 Preparation of 2,6-bis(pyrazol-3-yl) pyridine (bpp) ligand

The 2,6-bis(pyrazol-3-yl) pyridine (bpp) ligand was synthesized by the method of Lin and Lang[76]. 2,6-Diacetylpyridine (10 g, 61 mmol) and 20 ml N,N-dimethylformamide dimethyl acetal were refluxed for 10 hours, the solvent was then removed by distillation under reduced pressure using a water pump. The yellow solid obtained after recrystallization from $CHCl_3$ was then reacted with 5 ml of hydrazine hydrate in 25 ml ethanol. The content was stirred for 3 hours at room temperature. The subsequent dilution of the content gave a solid which was recrystallized twice from $CHCl_3$. The bpp ligand was obtained as a white solid, m.p. 258 - 260°C. Anal. Calcd. for bpp: C, 62.55; H, 4.30; N, 33.16. Found: C, 62.33; H, 4.28; N, 32.93. One dimensional ^1H NMR spectrum of bpp ligand dissolved in DMSO-d_6 was given in figure 3.2.1, δ values 6.7 - 8.2 ppm (ArH), 13.04 ppm (NH) and 13.50 ppm (NH).

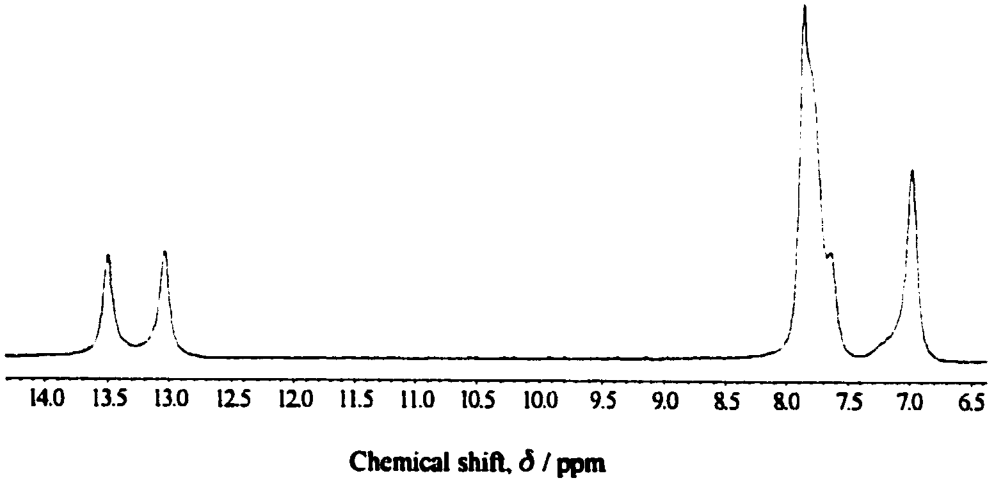

Figure 3.2.1 300 MHz ^1H NMR spectrum of bpp ligand in DMSO-d_6 at room temperature.

3.3 Preparation of Mn^{2+}-doped $[Fe(bpp)_2][CF_3SO_3]_2.H_2O$ complex

The Mn^{2+}-doped $[Fe(bpp)_2][CF_3SO_3]_2.3H_2O$ complex was made by reacting the bpp ligand (2.2 mmol) in 20 ml hot water with aqueous solutions of $FeCl_2.4H_2O$ (1 mmol) and $MnCl_2.4H_2O$ (0.1 mmol) under N_2 atmosphere, this was followed by the addition of $NaCF_3SO_3$ (2.2 mmol) to the cooled filtrate and the trihydrate was obtained as red-brown crystals after the contents were left to stand overnight. The monohydrate was obtained, as yellow powder, by heating the trihydrate at 65°C for 24 hours in an oven. Anal. Calcd. for $[Fe(bpp)_2][CF_3SO_3]_2.3H_2O$: C, 34.71; H, 2.91; N, 16.87; Fe, 6.72. Found: C, 34.98; H, 2.86; N, 17.05; Fe, 6.80. Anal. Calcd. for $Fe(bpp)_2(CF_3SO_3)_2.H_2O$: C, 36.29; H, 2.54; N, 17.63; S, 8.07; F, 14.35; Fe, 7.03. Found: C, 36.14; H, 2.48; N, 17.90; S, 7.94; F, 14.20; Fe, 7.20.

3.4 Preparation of Mn^{2+}-doped $[Fe(bpp)_2][BF_4]_2$ complex

The $[Fe(bpp)_2][BF_4]_2.2H_2O$ complex was made according to the procedure given elsewhere[77]. It was obtained by reacting $Fe(BF_4)_2.6H_2O$ (1 mmol) and bpp ligand (2 mmol) in 20 ml warm ethanol solution, this was followed by the addition of a small volume of diethyl ether, the precipitates were filtered, washed with diethyl ether and dried in air. The Mn^{2+}-doped $[Fe(bpp)_2][BF_4]_2.2H_2O$ complex was made by recrystallising a mixture of the pure Fe^{2+} complex and $Mn(BF_4)_2$ (*ca.* 3 mole % with respect to the Fe^{2+} complex) in ethanol solution, it was obtained as a red-brown flaky solid. The anhydrous form was obtained, as a yellow powder, by heating the hydrated form at 110°C for 1 hour in an oven. Anal. Calcd. for $[Fe(bpp)_2][BF_4]_2.2H_2O$: C, 38.41; H, 3.22; N, 20.36; Fe, 8.12. Found: C, 38.87; H, 3.16; N, 20.73; Fe, 8.01; Mn, 0.05. Anal. Calcd. for $[Fe(bpp)_2][BF_4]_2$: C, 40.53; H, 2.78; N, 21.49; Fe, 8.57. Found: C, 40.14; H, 2.71; N, 21.20; Fe, 8.50; Mn, 0.05.

3.5 Preparation of Mn^{2+}-doped $[Fe(5\text{-}NO_2\text{-}sal\text{-}N(1,4,7,10))]$ complex

The Mn^{2+}-doped $[Fe(5\text{-}NO_2\text{-}sal\text{-}N(1,4,7,10))]$ complexes was synthesized with reference to the "one pot" procedure described elsewhere[78,79]. 1,4,7,10-Tetraazadecane (3.4 mmol) in 10 ml of methanol was added dropwise to 5-nitrosalicyaldehyde (6.5 mmol) in 20 ml of methanol and the contents were refluxed for 1 hour, this was followed by the addition of a sufficient amount of freshly prepared $NaOCH_3$ (3.2 mmol) to the cooled yellow suspension. $Fe(CH_3COO)_2$ (3.0 mmol) in 10 ml methanol was added to the deprotonated ligand solution, this was followed by adding $Mn(CH_3COO)_2.4H_2O$ (0.3 mmol) in 5 ml of methanol and the resulting dark greenish blue suspension was heated at 45°C for 16 hours. The final product was washed with 20 ml cold methanol followed by 20 ml of petroleum ether, then dried in a vacuum desiccator overnight. The Mn^{2+}-doped [Fe(5-NO_2-sal-N(1,4,7,10))] complex was obtained as dark green powder. Anal. Calcd. for [Fe(5-NO_2-sal-N(1,4,7,10))]: C, 48.21; H, 4.45; N, 16.87; Fe, 11.21. Found: C, 46.52; H, 3.87; N, 15.37; Fe, 10.15; Mn, 0.26.

CHAPTER 4

TEMPERATURE-DEPENDENT ESR STUDIES

4.1 Introduction

The $[Fe(bpp)_2][CF_3SO_3]_2.H_2O$ complex has been found[73], using magnetic susceptibility measurement, to show a temperature-dependent HS ↔ LS crossover with critical temperatures $T_c^{\downarrow} = 147K$ and $T_c^{\uparrow} \approx 285K$ in the cooling and heating directions, respectively. The color of the complex being yellow and orange-brown for the HS and LS state, respectively. The LS → HS crossover occurs in two stages in the heating direction. The first stage transition occurs over a temperature range 150 - 190K, followed by a plateau region from 190K to 250K containing *ca*. 33% HS state, and the second stage occurs over the temperature range 250 - 300K. A metastable HS state can be formed by rapidly cooling the sample at liquid nitrogen temperature, but the normal HS → LS relaxation occurs at higher temperatures. This freezing-in of the HS state at low temperature has also been observed in other Fe^{2+} spin crossover systems[42,53,72]. A first-order phase change is also inferred from the thermal hysteresis behavior of the $[Fe(bpp)_2][CF_3SO_3]_2.H_2O$ system.

The $[Fe(bpp)_2][BF_4]_2$ complex has been found in Buchen *et al.*[68] studies, using Mössbauer and magnetic susceptibility measurements, and in Goodwin and Sugiyarto[72] studies, using magnetic susceptibility measurement, to show the thermal HS ↔ LS crossover behavior. Buchen *et al.*[68] reported the critical temperatures $T_c^{\downarrow} = 170K$ and $T_c^{\uparrow} = 180K$ in the respective cooling and heating directions, whereas Goodwin and Sugiyarto[72] reported $T_c^{\downarrow} = 173K$ and $T_c^{\uparrow} = 183K$. The color of the complex being yellow and red-brown for the HS and LS state, respectively. A metastable HS state can also be formed by rapidly cooling the system from room temperature to liquid nitrogen temperature, and at higher temperatures the usual HS → LS transition also occurs in association with a first-order phase change. In both studies, the first-order phase change is inferred from the thermal hysteresis behavior of the system.

The [Fe(5-NO_2-sal-N(1,4,7,10))] complex has been found[74], using Mössbauer and magnetic susceptibility studies, to undergo an unusual two-step thermal spin crossover with an abrupt change in temperatures at T = 173K, 136K and T = 146K, 180K along the cooling and the heating curves, respectively. The two-step conversion between the HS and LS ground states is separated by a plateau, at about 140K to 170K, corresponding to an approximately equal thermal population of the two spin states. X-ray studies[75] at 292K and 153K revealed the space group of P2/c with Z = 2 (a = 10.153Å, b = 8.490Å, c = 13.173Å and β = 109.93°) and P2 with Z = 2 (a = 9.952Å, b = 8.537Å, c = 13.070Å and β = 109.47°), respectively, of the monoclinic system, and the space group P1 with Z = 2 (a = 9.839Å, b = 8.336Å, c = 13.066Å, α = 90.06°, β = 107.84° and γ = 90.01°) of the triclinic system at 103K. This indicates that a structural phase transformation has occurred during the spin-state transition. The color of the complex being dark blue-green to black.

The main objective of the present work is to provide more information concerning the HS ↔ LS crossover in these complexes, experimental results may be valuable in providing a better understanding of the nature and dynamics of the interconversion between the HS and LS ground states in the systems. All complexes were doped with the Mn^{2+} ion (*ca.* 0.6 - 3 mole %) which served as an ESR probe, enabling the changes within the system during HS ↔ LS crossover to be observed. Since the amount of Mn^{2+} ion used in the present studies is well within the concentration range normally used in the previous ESR studies[43,44,55-57] of Fe^{2+} spin crossover complexes, there would be no appreciable broadening of the Mn^{2+} spectral lines. Although the concentration of Mn^{2+} ion in the Mn^{2+} doped [Fe(5-NO_2-sal-N(1,4,7,10))] system is about 2.5 mole %, X-ray studies[75] of the pure Fe^{2+} complex has shown that the shortest distance between Fe atoms is about 8.5Å which would keep the Mn^{2+} ions far from each other to allow for the appearance of hyperfine splitting in the Mn^{2+} spectrum.

4.2 Instrumentation and Apparatus

An X-band Bruker ESP 300E spectrometer was used in all the experimental measurements of the Mn^{2+} doped complexes. Since a detailed discussion of the major components and the working principles of an ESR spectrometer can be found elsewhere[1,3,5,6,28,80-83], only a brief summary of those features of practical importance will be given. Both the microwave source and the detector are housed in a box known as the microwave bridge which is connected to the microwave cavity by the waveguide. The microwave radiation is generated by a klystron, and the frequency is tunable over the range 9.1 - 9.9GHz. An HP 5350B microwave frequency counter is used to measure the frequency to an accuracy of 10^{-7} GHz. The spectrometer has a rectangular TE_{102} mode microwave cavity, the inner surface of the cavity is gold-plated to maximize the Q-factor and minimize possible spurious signals from the presence of paramagnetic impurities in the cavity walls. The microwave radiation generated by the klystron is coupled into the cavity via an iris, and the size of the iris can be varied by using the adjustable iris screw situated in front of the iris. The amount of microwaves going in and out of the cavity is determined by the size of the iris. A magnetic field from 50G to 15kG is provided by an electromagnet. A variable temperature unit is used for all the ESR measurements at different temperatures. The unit consist of a 25 litre liquid nitrogen storage Dewar, a liquid nitrogen evaporator, metal transfer line, thermocouple, heater, VT-Dewar holder, and a Bruker B-VT2000 temperature control unit capable of providing a digital temperature readout to $\pm 0.1K$. For low temperature ESR measurements at 77K, a 50 ml finger Dewar is used. Both the VT-Dewar and the finger Dewar can best be described by the pictures shown in figure 4.2.1.

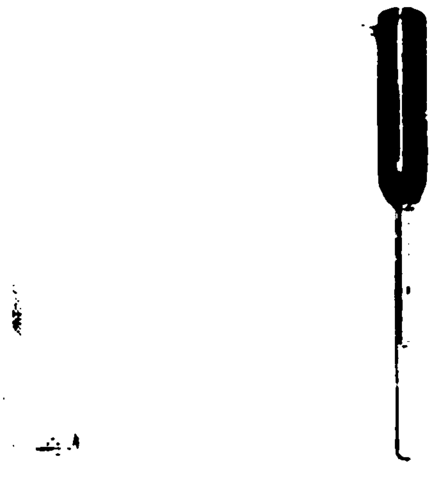

VT-Dewar

50 ml finger Dewar

Figure 4.2.1 Pictures showing a VT-Dewar and a 50 ml finger Dewar.

4.3 Calibration of Temperature

Although the variable temperature unit associated with the Bruker ESP 300E spectrometer can provide a digital temperature readout to ± 0.1K, the actual temperature T* of the sample during the variable temperature measurements may not correspond to the measured temperature owing to the configuration and the positioning of the sample tube within the unit. A temperature calibration procedure was undertaken to ensure that the experimental temperature readings can be corrected to reflect T* of the volume of the sample during the measurements. This was done by using the pre-calibrated copper-constantan thermocouple thermometer, model 8528-12, obtained from the Cole-Parmer Instrument Company. The thermocouple probehead was inserted into an ESR tube, it was then carefully placed inside the VT-Dewar leaving a 2 - 3 mm gap above the temperature control sensor mounted inside the VT-Dewar. Gaseous nitrogen produced from the insulated liquid nitrogen container was fed along the transfer line connected to the side arm near the bottom of the VT-Dewar. The temperature of the system was lowered gradually from room temperature to the lowest controllable temperature of 104.5K. The digital temperature readouts from the Bruker B-VT2000 nitrogen-flow variable temperature control unit were then correlated with the temperature readings

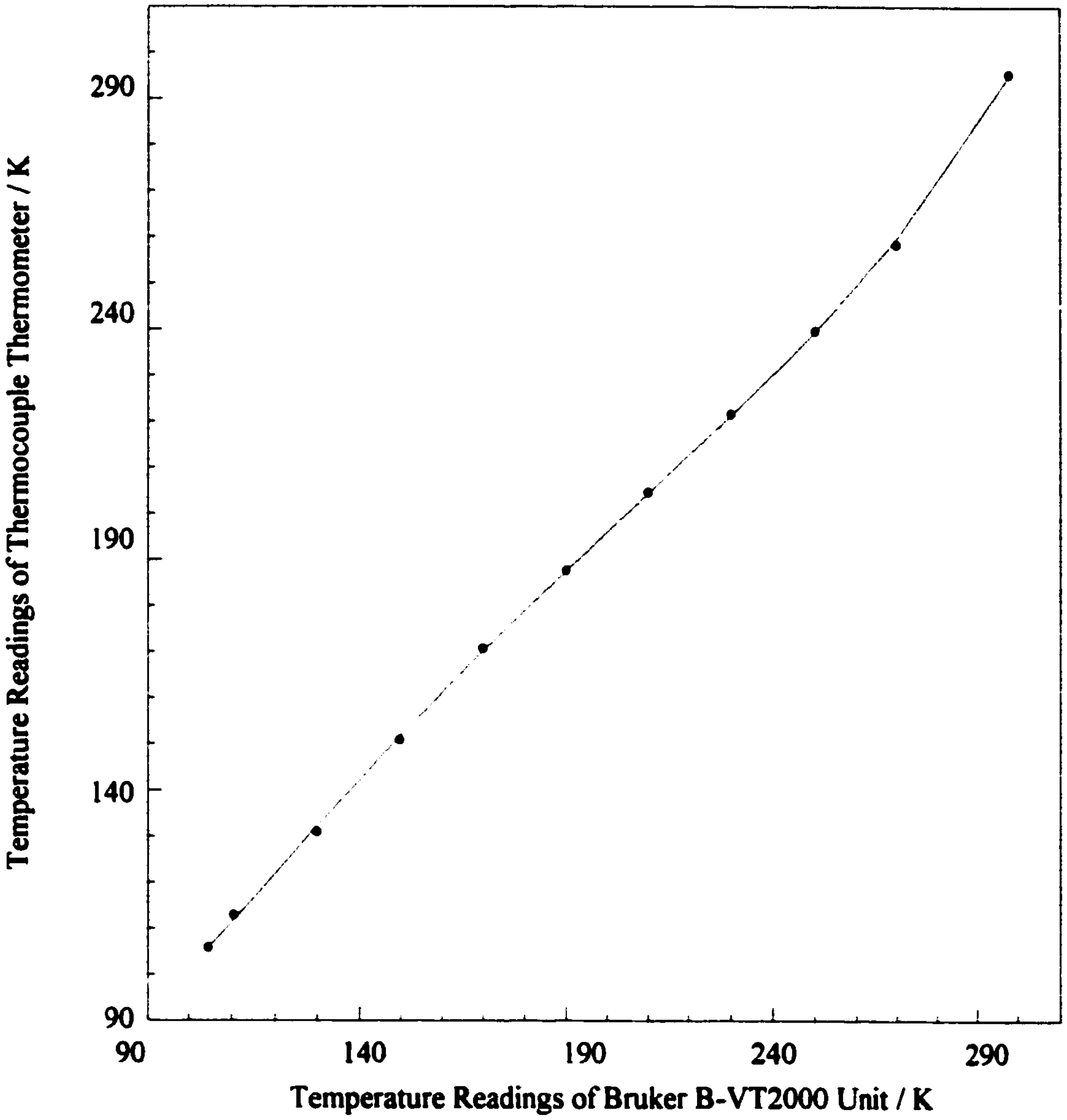

Figure 4.3.1 Calibration of temperature. The data points are fitted using a polynomial to the fourth-order. Coefficient of determination is 0.9998.

obtained from the thermocouple thermometer. A graph of best fit was constructed using a polynomial to the fourth-order, and the coefficient of determination was found to be 0.9998. The results are given in figure 4.3.1.

4.4 Variable Temperature ESR Measurements

Powder ESR spectra of Mn^{2+} ion in the $[Fe(bpp)_2][CF_3SO_3]_2.H_2O$, $[Fe(bpp)_2][BF_4]_2$ and $[Fe(5\text{-}NO_2\text{-}sal\text{-}N(1,4,7,10))]$ complexes at different temperatures were obtained using the variable temperature unit. The sample tube was carefully inserted into the VT-Dewar mounted inside the microwave cavity. It was then adjusted to leave a 2 - 3 mm gap above the temperature control sensor mounted inside the VT-Dewar. Gaseous nitrogen produced from the insulated liquid nitrogen container was fed along the transfer line connected to the side arm near the bottom of the VT-Dewar. The temperature of the sample was controlled at $\pm 0.1K$ by the Bruker B-VT2000 nitrogen-flow variable temperature control unit. The sample was gradually cooled from room temperature to the lowest attainable temperature during the measurements, it was then gradually heated to the room temperature again. All the experimental temperature readings obtained from the B-VT2000 unit were corrected to give the corresponding actual temperature readings T^* by means of the calibration graph given in figure 4.3.1. A total of 58, 35 and 41 spectra were obtained for $[Fe(bpp)_2][CF_3SO_3]_2.H_2O$, $[Fe(bpp)_2][BF_4]_2$, and $[Fe(5\text{-}NO_2\text{-}sal\text{-}N(1,4,7,10))]$ complexes, respectively. They are given in figures 4.7.1(a) - (e), figures 4.7.3(a) - (c), and figures 4.7.5(a) - (c), respectively.

The same set of experimental parameters was employed in the VT measurements of the complexes. All powder ESR spectra were acquired using a microwave power 20mW, microwave frequency 9.5GHz, modulation frequency 100kHz, modulation amplitude 4.062G, 4k data points covering a magnetic field from 50G - 7500G for $[Fe(bpp)_2][CF_3SO_3]_2.H_2O$ and $[Fe(bpp)_2][BF_4]_2$ complexes and 50G - 8500G for $[Fe(5\text{-}NO_2\text{-}sal\text{-}N(1,4,7,10))]$ complex.

4.5 ESR Spectra at Room Temperature and 77K

Room temperature ESR measurements of Mn^{2+} ion in the powder sample of the $[Fe(bpp)_2][CF_3SO_3]_2.H_2O$, $[Fe(bpp)_2][BF_4]_2$, and $[Fe(5\text{-}NO_2\text{-sal-N}(1,4,7,10))]$ complexes were done by carefully placing the sample tube directly inside the microwave cavity. The ESR results are given in figures 4.7.2(a), 4.7.4(a) and 4.7.6(a), respectively.

Low temperature measurements of the complexes at 77K were done using the 50 ml finger Dewar flask. In the slow-cooled experiments, the sample tube was very slowly dipped in the liquid nitrogen contained in the finger Dewar flask outside the microwave cavity, this was then carefully transferred to the microwave cavity and ESR spectra taken. In the case of $[Fe(bpp)_2][CF_3SO_3]_2.H_2O$ complex, the color of the sample changed from yellow to orange-brown during the cooling process. The color of the $[Fe(bpp)_2][BF_4]_2$ complex also changed from yellow to red-brown during the cooling process. Visual detection of color change for the $[Fe(5\text{-}NO_2\text{-sal-N}(1,4,7,10))]$ complex was not possible owing to its dark-green nature. Powder ESR spectra of Mn^{2+} ion in the $[Fe(bpp)_2][CF_3SO_3]_2.H_2O$, $[Fe(bpp)_2][BF_4]_2$, and $[Fe(5\text{-}NO_2\text{-sal-N}(1,4,7,10))]$ complexes are given in figures 4.7.2(b), 4.7.4(b) and 4.7.6(b), respectively. In the rapid-cooled experiments, the sample tube was plunged directly into the liquid nitrogen contained in the finger Dewar flask outside the microwave cavity, this was then carefully transferred to the microwave cavity and ESR spectra taken. The color of both the $[Fe(bpp)_2][CF_3SO_3]_2.H_2O$ and $[Fe(bpp)_2][BF_4]_2$ complexes remained yellow during the cooling process. The dark-green color of the $[Fe(5\text{-}NO_2\text{-sal-N}(1,4,7,10))]$ complex also remained unchanged during the cooling process. The ESR results are given in figures 4.7.2(c), 4.7.4(c), and 4.7.6(c), respectively.

The same experimental measurement conditions used in the VT measurements of the $[Fe(bpp)_2][CF_3SO_3]_2.H_2O$, $[Fe(bpp)_2][BF_4]_2$, and $[Fe(5\text{-}NO_2\text{-sal-N}(1,4,7,10))]$ complexes were also used in the room temperature and 77K measurements.

4.6 ESR Spectral Analysis and Simulations

Since all the complexes studied were doped with Mn^{2-} ion, the same general principle used in the analysis of Mn^{2-} powder spectrum can be applied. For an S-state ion with $S = \frac{5}{2}$ and $I = \frac{5}{2}$, there should be five resonance lines corresponding to the $M_s = -\frac{5}{2} \rightarrow M_s = -\frac{3}{2}$, $M_s = -\frac{3}{2} \rightarrow M_s = -\frac{1}{2}$, $M_s = -\frac{1}{2} \rightarrow M_s = \frac{1}{2}$, $M_s = \frac{1}{2} \rightarrow M_s = \frac{3}{2}$ and $M_s = \frac{3}{2} \rightarrow M_s = \frac{5}{2}$ transitions if **H** is along the *z*-axis. Each of these resonance line will be split into a sextet by the nuclear spin of the ion giving rise to a pattern of five groups of sextet. The microwave absorption energy for the allowed $(M_s - 1) \rightarrow M_s$ transition is given by equation (1.7.2), and to first-order approximation this can be expressed as

$$h\nu = g\beta_e H + \frac{1}{2} D \left[3\left(\frac{g_{\parallel}}{g}\right)^2 \cos^2\theta - 1 \right] (2M_s - 1) \qquad (4.6.1)$$

When $\theta = 0^\circ$ for **H** along the *z*-axis, the resonance fields H can be obtained from

$$H = H_0 - \frac{D(2M_s - 1)}{g\beta_e} \qquad (4.6.2)$$

where $H_0 = \frac{h\nu}{g\beta_e}$ which is the resonance field for the system with g = 2.0000. By substituting the appropriate M_s values into equation (4.6.2), the resonance fields for the five resonance lines are

$$H\left(-\tfrac{5}{2} \rightarrow -\tfrac{3}{2}\right) = H_0 + \frac{4D}{g\beta_e}$$

$$H\left(-\tfrac{3}{2} \rightarrow -\tfrac{1}{2}\right) = H_0 + \frac{2D}{g\beta_e}$$

$$H\left(-\tfrac{1}{2} \rightarrow \tfrac{1}{2}\right) = H_0 \qquad (4.6.3)$$

$$H\left(\tfrac{1}{2} \rightarrow \tfrac{3}{2}\right) = H_0 - \frac{2D}{g\beta_e}$$

$$H\left(\tfrac{3}{2} \rightarrow \tfrac{5}{2}\right) = H_0 - \frac{4D}{g\beta_e}$$

The zero-field splitting parameter D can be obtained by solving any two of the formulae given in equation (4.6.3). For example, by dividing the difference between the resonance line at $H\left(-\tfrac{5}{2} \rightarrow -\tfrac{3}{2}\right)$ and $H\left(-\tfrac{1}{2} \rightarrow \tfrac{1}{2}\right)$ by 4 and multiplying the result by $g\beta_e$ gives the D value expressed in units of erg. In ESR studies, D values are normally reported in units of wavenumbers cm^{-1} and 1 erg is equal to 5.0348×10^{15} cm^{-1}. In a similar manner, the five resonance fields for the allowed $(M_s - 1) \rightarrow M_s$ transition in the *xy* plane can also be found when $\theta = 90^\circ$.

$$\begin{aligned}
H\left(-\tfrac{5}{2} \rightarrow -\tfrac{3}{2}\right) &= H_0 - \frac{2D}{g\beta_e} \\
H\left(-\tfrac{3}{2} \rightarrow -\tfrac{1}{2}\right) &= H_0 - \frac{D}{g\beta_e} \\
H\left(-\tfrac{1}{2} \rightarrow \tfrac{1}{2}\right) &= H_0 \qquad\qquad (4.6.4) \\
H\left(\tfrac{1}{2} \rightarrow \tfrac{3}{2}\right) &= H_0 + \frac{D}{g\beta_e} \\
H\left(\tfrac{3}{2} \rightarrow \tfrac{5}{2}\right) &= H_0 + \frac{2D}{g\beta_e}
\end{aligned}$$

A schematic diagram showing the resonance fields for **H** along *z*-axis and **H** in the *xy* plane is given in figure 4.6.1. The final ESR spectrum may also be further complicated due to the overlapping of some or all of resonance lines between the sextets. These can be visualized from the analysis of the spectrum obtained at 290.5K in the VT measurements of the $[Fe(bpp)_2][CF_3SO_3]_2.H_2O$ complex as given in figure 4.6.2(a).

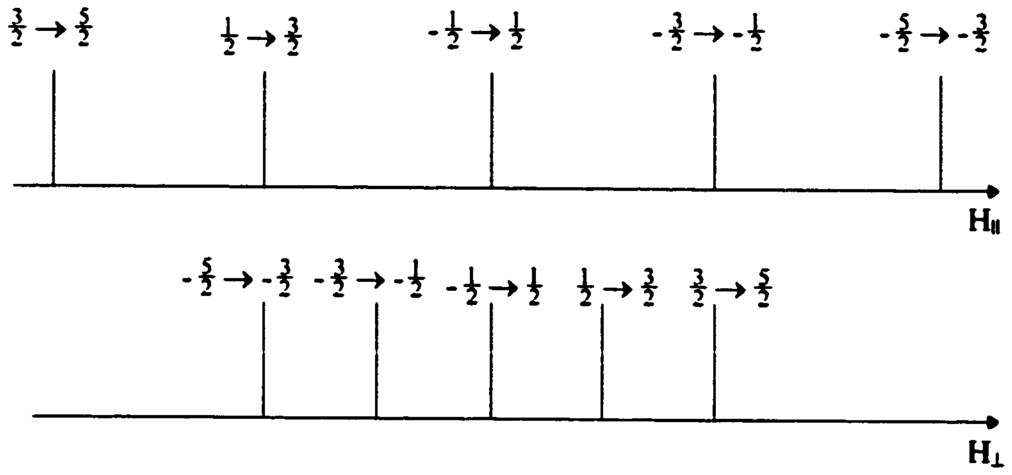
$\frac{3}{2}\to\frac{5}{2}$
$\frac{1}{2}\to\frac{3}{2}$
$-\frac{1}{2}\to\frac{1}{2}$
$-\frac{3}{2}\to-\frac{1}{2}$
$-\frac{5}{2}\to-\frac{3}{2}$
$H_\parallel$
$-\frac{5}{2}\to-\frac{3}{2}$
$-\frac{3}{2}\to-\frac{1}{2}$
$-\frac{1}{2}\to\frac{1}{2}$
$\frac{1}{2}\to\frac{3}{2}$
$\frac{3}{2}\to\frac{5}{2}$
$H_\perp$

Figure 4.6.1 Schematic diagram showing the resonance fields for **H** along the *z*-axis and **H** in the *xy* plane.

The experimental powder ESR spectrum given in figure 4.6.2(a) is the paramagnetic form of the $[Fe(bpp)_2][CF_3SO_3]_2.H_2O$ complex, it has a number of identifiable spectral features. The resonance fields of H-3 centered at 6123G, H-1 at 4734G, H1 at 3378G and H5 at 634G have been identified to correspond to the $M_s=-\frac{5}{2}\to M_s=-\frac{3}{2}$, $M_s=-\frac{3}{2}\to M_s=-\frac{1}{2}$, $M_s=-\frac{1}{2}\to M_s=\frac{1}{2}$, and $M_s=\frac{3}{2}\to M_s=\frac{5}{2}$ transitions, respectively, for **H** along the *z*-axis. The resonance field of H'5 centered at 5383G corresponds to the $M_s=\frac{3}{2}\to M_s=\frac{5}{2}$ transition for **H** in the *xy* plane. Both the sextets at H-3 and H'5 look like negative absorption curves because they are the high field cutoffs for the $M_s=-\frac{5}{2}\to M_s=-\frac{3}{2}$ transition when $\theta = 0^\circ$ and $M_s=\frac{3}{2}\to M_s=\frac{5}{2}$ transition when $\theta = 90^\circ$, respectively. The nuclear hyperfine-splitting constant A for Mn^{2+} ion is found to be 83 ± 1G. This is done by measuring the distance between the outside peaks of H-3 and dividing by 5. The zero-field splitting parameter D is estimated at 685G, this is found by dividing the distance between the resonance field at H1 for a system with g = 2.0000 and that at H-3 by 4. The correct D value is then found from the computer simulation. H-1 is the highest turning point for the $-\frac{3}{2}\to-\frac{1}{2}$ transition in the *z*-principal direction and is approximately halfway between H1 and H-3 for most values of E. In axial symmetry the *x* and *y* turning points of the $\frac{5}{2}\to\frac{3}{2}$ transition would occur

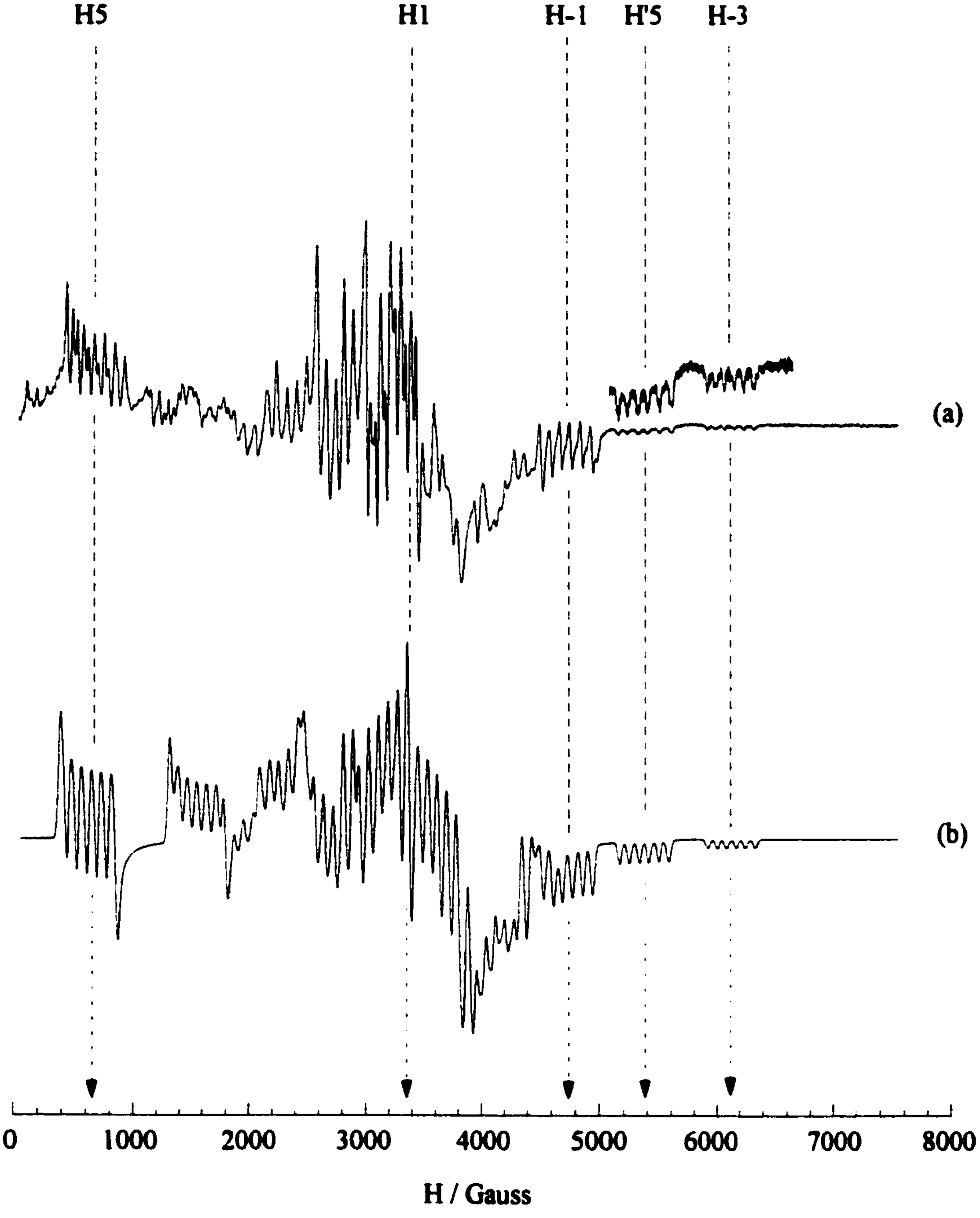

Figure 4.6.2 Powder ESR spectra of Mn^{2+} in $[Fe(bpp)_2][CF_3SO_3]_2.H_2O$ complex at 290.5K. (a) is the experimental spectrum, and (b) is the computer-simulated spectrum obtained using parameters from Table 4.6.1.

near H-1 in the spectrum giving a first derivative shape but for large values of E the x and y turning points would separate and the high field turning point would look like a negative absorption peak and would be found between H-1 and H-3. The peak labeled as H'5 has been assigned to this turning point and its position is very sensitive to the value of E.

The computer simulation of the experimentally observed powder ESR spectrum was done using the SimFonia powder simulation program obtained from Bruker, whose calculations are based on perturbation theory to second-order approximation. The program simulates ESR spectra for $S = \frac{1}{2}$ to $S = \frac{7}{2}$ systems, and only allowed ESR transitions are simulated. The assumption made in the simulations is that the electronic Zeeman interaction is the largest, followed by the zero-field splitting, and the nuclear hyperfine term is the smallest. Perturbation theory works best when the ratio between the successive interactions is at least ten. The experimentally estimated D value for g = 2.0000 was used in the first simulation process to obtain the approximate locations of the resonance fields. The calculation procedure was repeated by adjusting both the D and E values, keeping A at the originally estimated value, to obtain a good fit of the spectrum. The correct D and E values were then obtained from the simulated spectrum. The result is given in figure 4.6.2(b). The structural features in the high field region from H-1 to H-3 are clearly seen matching up with those observed in the experimental spectrum. The simulation program also predicts the low-field features, such as H5, but most of the resonance lines appear to fall out of place. This is due to the breaking down of the assumption used in the perturbation calculation which assumes that $g\beta_e H >> D$. For the resonance field of H5 centered at 634G, the ratio between H5 and D is only about 0.9. The same procedures were also used in the simulations of the VT spectra at 239.5K, 196.3K, 179.1K, 156.7K, 152.0K, 150.3K, 142.5K and the spectra obtained after rapidly and slowly cooling of the powder sample at 77K. The results are given in figures 4.6.3 and 4.7.2, respectively. For reason of clearer comparison, only the high field region of the simulated spectra are shown. The parameters used in the simulations are given in Table 4.6.1.

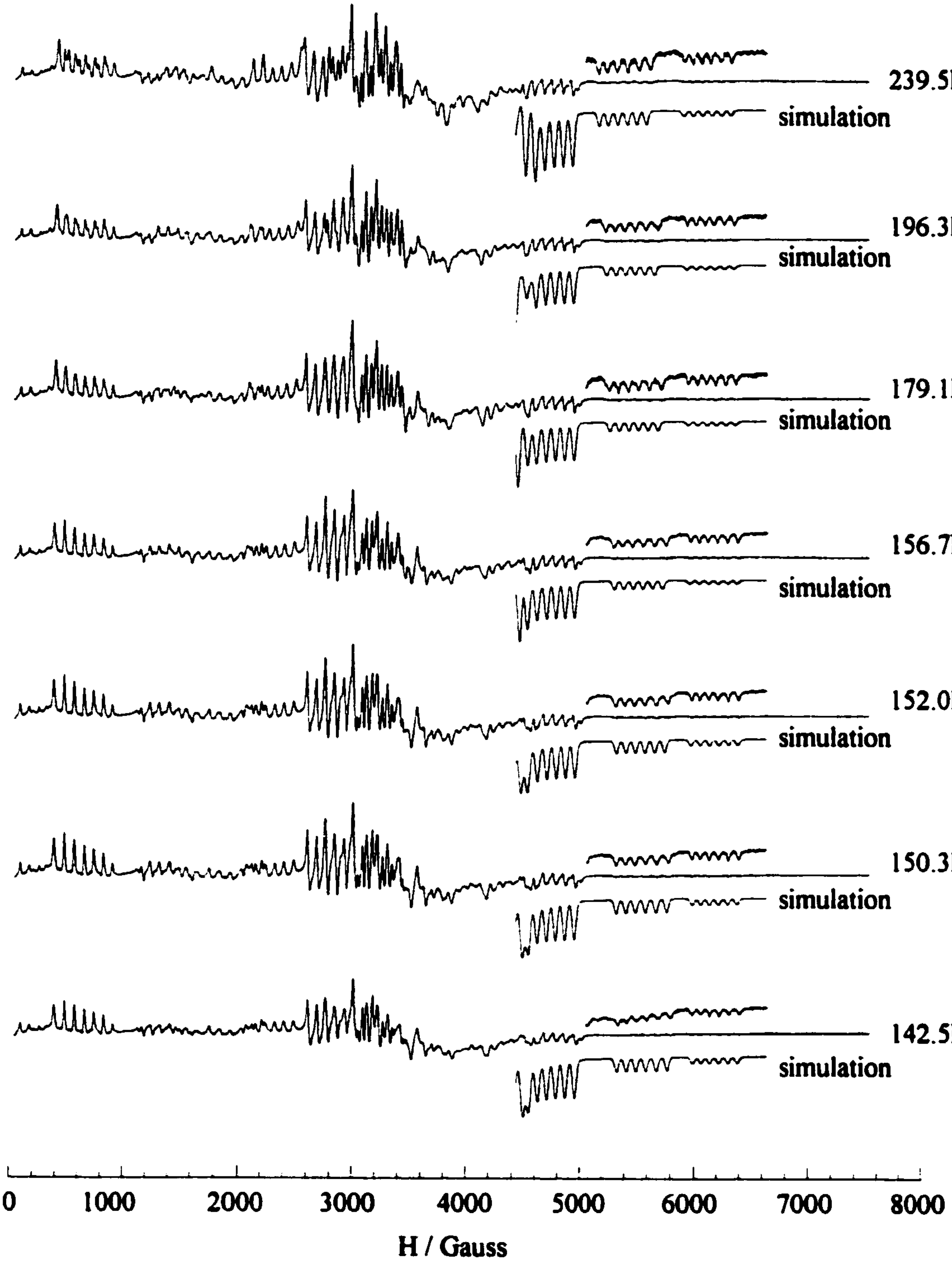

Figure 4.6.3 Powder ESR spectra of Mn^{2+} in $[Fe(bpp)_2][CF_3SO_3]_2.H_2O$ complex at different temperatures T* as indicated. The computer-simulated spectra are obtained using parameters from Table 4.6.1. Only the high field region of the simulated spectra is shown for clearer comparison with those experimentally observed.

Table 4.6.1 Parameters used in SimFonia simulations of powder ESR spectra of Mn^{2+}-doped $[Fe(bpp)_2][CF_3SO_3]_2.H_2O$ complex.

T* / K	g	A / G	D × 10^4 / cm^{-1}	E × 10^4 / cm^{-1}
290.5	2.0000	83 ± 1	640 ± 2	81 ± 2
239.5	2.0000	83 ± 1	641 ± 2	84 ± 2
196.3	2.0000	83 ± 1	646 ± 2	93 ± 2
179.1	2.0000	83 ± 1	649 ± 2	97 ± 2
156.7	2.0000	83 ± 1	652 ± 2	102 ± 2
152.0	2.0000	83 ± 1	654 ± 2	104 ± 2
150.3	2.0000	83 ± 1	655 ± 2	106 ± 2
142.5	2.0000	83 ± 1	655 ± 2	106 ± 2
77 (rapid cooled)	2.0000	83 ± 1	659 ± 2	120 ± 2
77 (slow cooled)	2.0000	83 ± 1	423 ± 2	41 ± 2
RT (298)	2.0000	83 ± 1	639 ± 2	79 ± 2

The zero-field splitting parameters for Mn^{2+} ion at 77K for the S = 2 system is very different from those for S = 0 system at the same temperature, indicating that the HS state of the complex resides in a different lattice than the LS state. The HS and LS states of the complex are characterized by two different types of Mn^{2+} spectra, and the errors in the zero-field splitting parameters are expected to be larger in the region of 140K due to mixed spectrum of both types. At temperature above 140K, the temperature-dependence of both the D and E parameters for Mn^{2+} ion in the HS phase of the complex are shown in figures 4.6.4 and 4.6.5, respectively. The increase in the D parameter as temperature decreases indicates an overall contraction of the crystal lattice has occurred in the HS phase over the temperature range 290.5 - 77K, and the increase in the E parameter indicates an increase of rhombic distortion from axial symmetry has also occurred.

The simulation of the powder ESR spectra of Mn^{2+} ion in the $[Fe(bpp)_2][CF_3SO_3]_2.H_2O$ complex obtained at temperatures below 142.5K has not been attempted because of the insignificant change in the observed D values between 141.5K and 137.5K. At further lower temperatures from 136.5 to 117.8K, the simulation

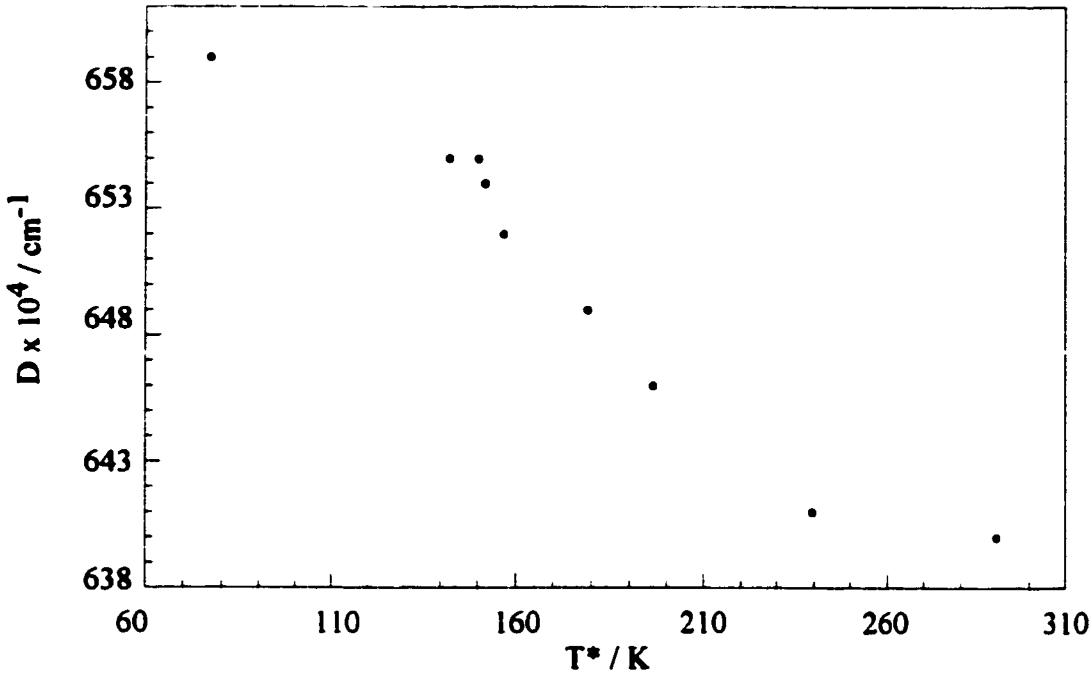

Figure 4.6.4 Temperature-dependence of D parameter for Mn^{2+} ion in HS phase of $[Fe(bpp)_2][CF_3SO_3]_2.H_2O$ complex.

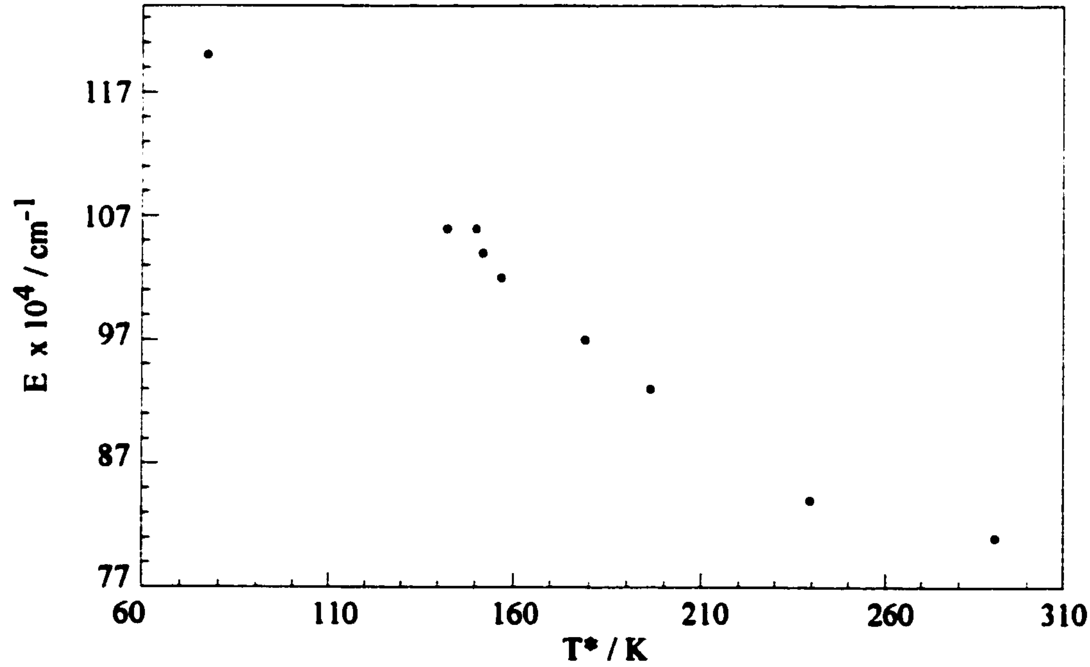

Figure 4.6.5 Temperature-dependence of E parameter for Mn^{2+} ion in HS phase of $[Fe(bpp)_2][CF_3SO_3]_2.H_2O$ complex.

becomes quite impossible due to the disappearance of the high-field structures at H-3. As can be seen in figure 4.7.1(c), the disappearance of the high-field structures is due to phase change accompanying the conversion from HS → LS state of the complex.

The same simulation program was also used in the simulations of the powder ESR spectra of Mn^{2+} ion in the $[Fe(bpp)_2][BF_4]_2$ complex obtained at room temperature and at 77K after rapidly and slowly cooling of the powder sample. The results are given in figure 4.7.4. For the same reason of clearer comparison, only the high field region of the simulated spectra are shown. The parameters used in the simulations are given in Table 4.6.2.

Table 4.6.2 Parameters used in SimFonia simulations of powder ESR spectra of Mn^{2+}-doped $[Fe(bpp)_2][BF_4]_2$ complex.

Temperature / K	g	A / G	$D \times 10^4 / cm^{-1}$	$E \times 10^4 / cm^{-1}$
RT(296)	2.0000	83 ± 1	593 ± 4	112 ± 4
77 (rapid cooled)	2.0000	83 ± 1	621 ± 4	163 ± 4
77 (slow cooled)	2.0000	83 ± 1	799 ± 4	188 ± 4

The broad and featureless spectra obtained for the Mn^{2+} ion in the $[Fe(5\text{-}NO_2\text{-}sal\text{-}N(1,4,7,10))]$ complex at different temperatures render their simulations quite impossible. It is apparent from the lack of a prominent peak in the g = 2 region that the condition of $D << g\beta_eH$ is not true. Equally the absence of a prominent peak at $g \sim 6$ indicates that $D >> g\beta_eH$ is also not true. Apparently D and $g\beta_eH$ are of similar magnitude. Therefore no simulation with the simulation program is possible.

4.7 Results and Discussion

$[Fe(bpp)_2][CF_3SO_3]_2.H_2O$ complex

The powder ESR spectra of the Mn^{2+} ion in $[Fe(bpp)_2][CF_3SO_3]_2.H_2O$ complex given in figures 4.7.1(a) - (c) show a gradual change in its spectral features at different temperatures during the HS → LS crossover. The spectrum of Mn^{2+} in the paramagnetic form of the complex with S = 2 at 290.5K is shown in figure 4.7.1(a), it has a D value of 640×10^{-4} cm^{-1}. The spectrum from the diamagnetic form of the complex with S = 0 at 117.8K and 77K is shown in figures 4.7.1(c) and 4.7.2(b), respectively. The D value for S = 0 at 77K is found to be 423×10^{-4} cm^{-1}. The large difference in the D values indicates that the HS and LS states are in two distinct types of lattice. The spectral features at about 5400G and 6100G appear to shift towards higher fields at decreasing temperatures, they become unrecognizable and disappear completely at temperatures below 133.5K. This is due to the disappearance of the HS domains accompanying the HS → LS transition, and the spin crossover occurs at T^{*} = 134.5 - 132.5K. As shown in figure 4.6.4, the increase in D value of Mn^{2+} in the HS phase is probably due to a contraction of the crystal lattice with temperature. The paramagnetic to diamagnetic phase transformation is also indicated in the more prominent spectral features in the regions of 600G, 4000G and 4800G. These features can be used as a measure of the formation of the diamagnetic form of the complex. The reverse change from LS → HS occurs over the increasing temperature range 127.5 - 298.0K, it is also accompanied by a reverse phase transformation in the lattice. As shown in figures 4.7.1(d) - (e), the ESR spectrum of Mn^{2+} undergoes a change with the appearance of features in the region of 600G and 6000G at 174.8K typical of the HS phase. From 180K until about 275K the spectrum changes little. There is a second change in the spectrum in the region 275 - 285K resulting in the HS phase spectrum observed originally. This two stage LS → HS conversion was originally detected in the magnetic susceptibility measurements of the complex by Buchen *et al.*[73] The quantitative estimation of the fractional amount of each of the two crystal forms during the LS → HS transition is not possible due to the complicated nature of the Mn^{2+} spectra.

The powder ESR spectra of Mn^{2+} given in figure 4.7.2 show the results of the slow and rapid cooling of the S = 2 system at 77K. The diamagnetic form of the complex, as shown in figure 4.7.2(b), can only be obtained by a slow cooling process, and it is stable over time. Visual observation has revealed a color change from yellow to orange-brown indicating that the ${}^{5}T_{2g} \rightarrow {}^{1}A_{1g}$ spin-state transition has also occurred. Rapid cooling of the paramagnetic form of the complex in liquid nitrogen has produced no new features in the observed spectrum as shown in figure 4.7.2(c), and the yellow color of the paramagnetic form of the complex also remains unchanged. The spectral features are similar to those observed for the paramagnetic form at room temperature as shown in figure 4.7.2(a). As shown in Table 4.6.1, the small difference in the D values of Mn^{2+} for the S = 2 system at room temperature and 77K suggests that the rapidly-cooled complex has a structure similar to that at room temperature. The yellow color of the complex also suggests that the $^5T_{2g}$ spin state has been trapped in the paramagnetic form of the rapidly-cooled sample at 77K. The crystal structure of the rapidly-cooled complex is also stable over time. At higher temperatures above 77K, the normal $^5T_{2g} \rightarrow {}^1A_{1g}$ spin-state transition occurs in association with the paramagnetic to diamagnetic phase transformation of the complex. The important result of the studies shows that the HS↔LS crossover in the $[Fe(bpp)_2][CF_3SO_3]_2.H_2O$ complex is due to a structural phase transformation of the lattice.

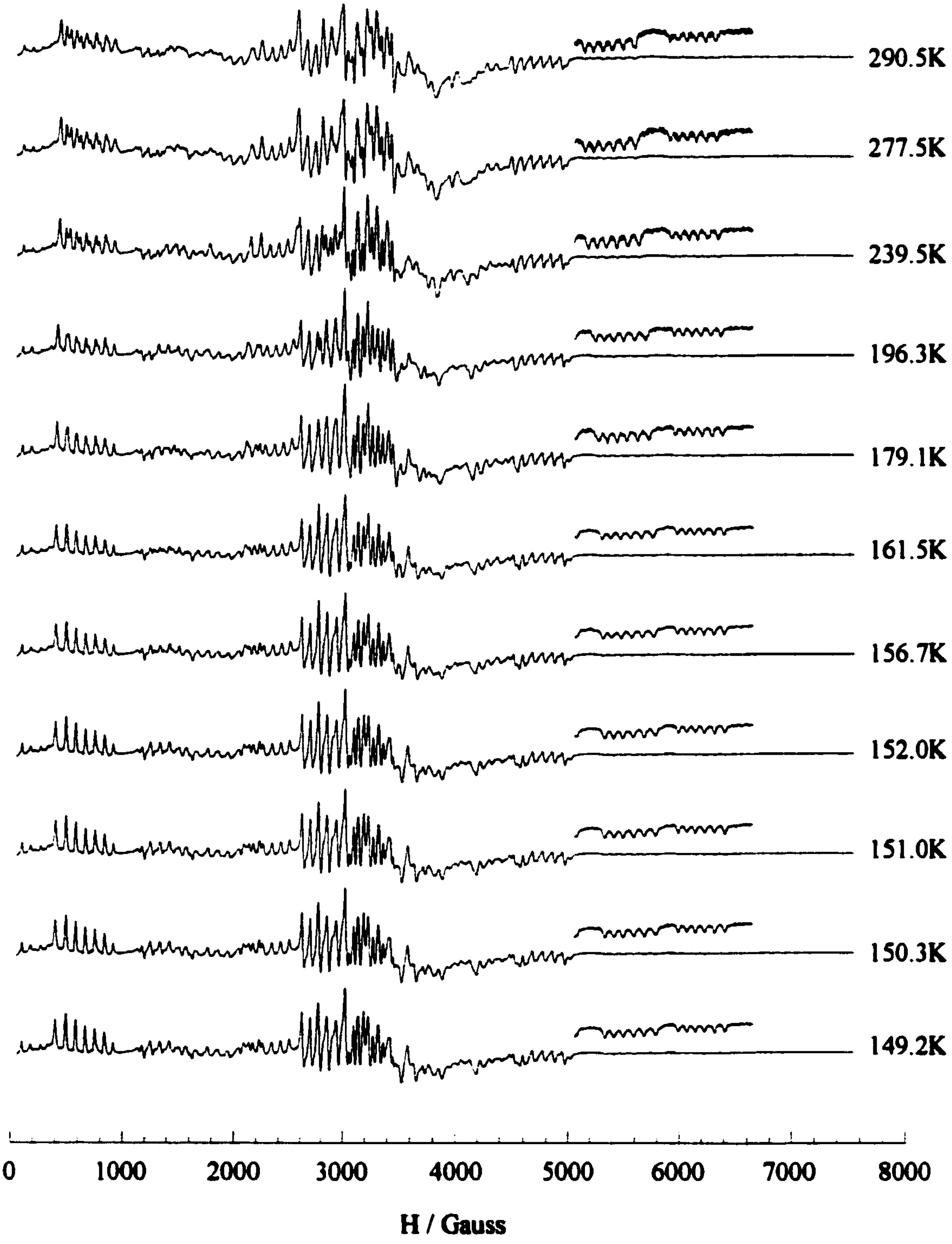

Figure 4.7.1(a) Powder ESR spectra of Mn^{2+} ion in $[Fe(bpp)_2][CF_3SO_3]_2.H_2O$ complex at decreasing temperatures T* as indicated. Sample was slowly cooled from 290.5K (top spectrum) to 149.2K (bottom spectrum).

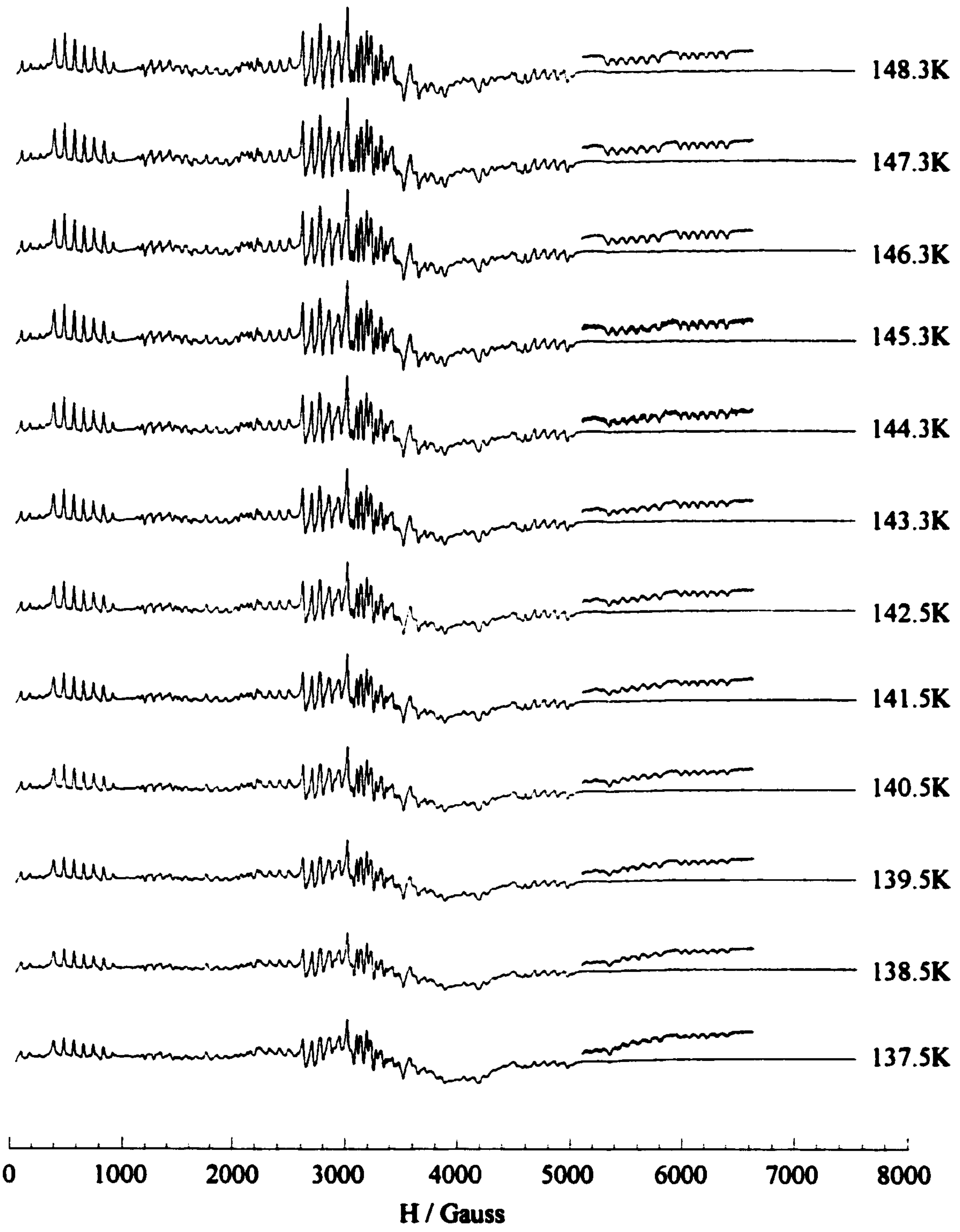

Figure 4.7.1(b) Powder ESR spectra of Mn^{2+} ion in $[Fe(bpp)_2][CF_3SO_3]_2.H_2O$ complex at decreasing temperatures T* as indicated. Sample was slowly cooled from 148.3K (top spectrum) to 137.5K (bottom spectrum).

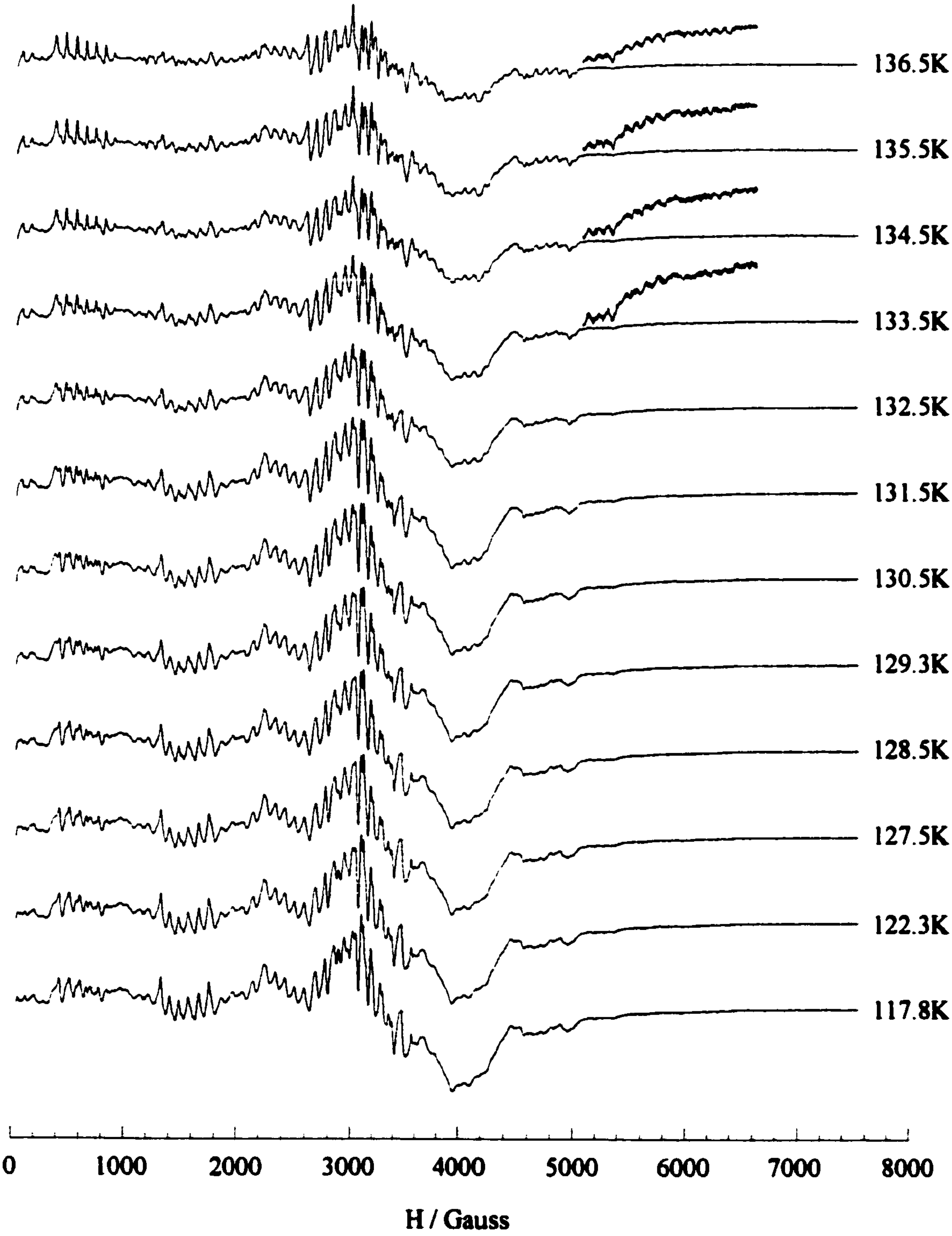

Figure 4.7.1(c) Powder ESR spectra of Mn^{2+} ion in $[Fe(bpp)_2][CF_3SO_3]_2.H_2O$ complex at decreasing temperature T* as indicated. Sample was slowly cooled from 136.5K (top spectrum) to 117.8K (bottom spectrum).

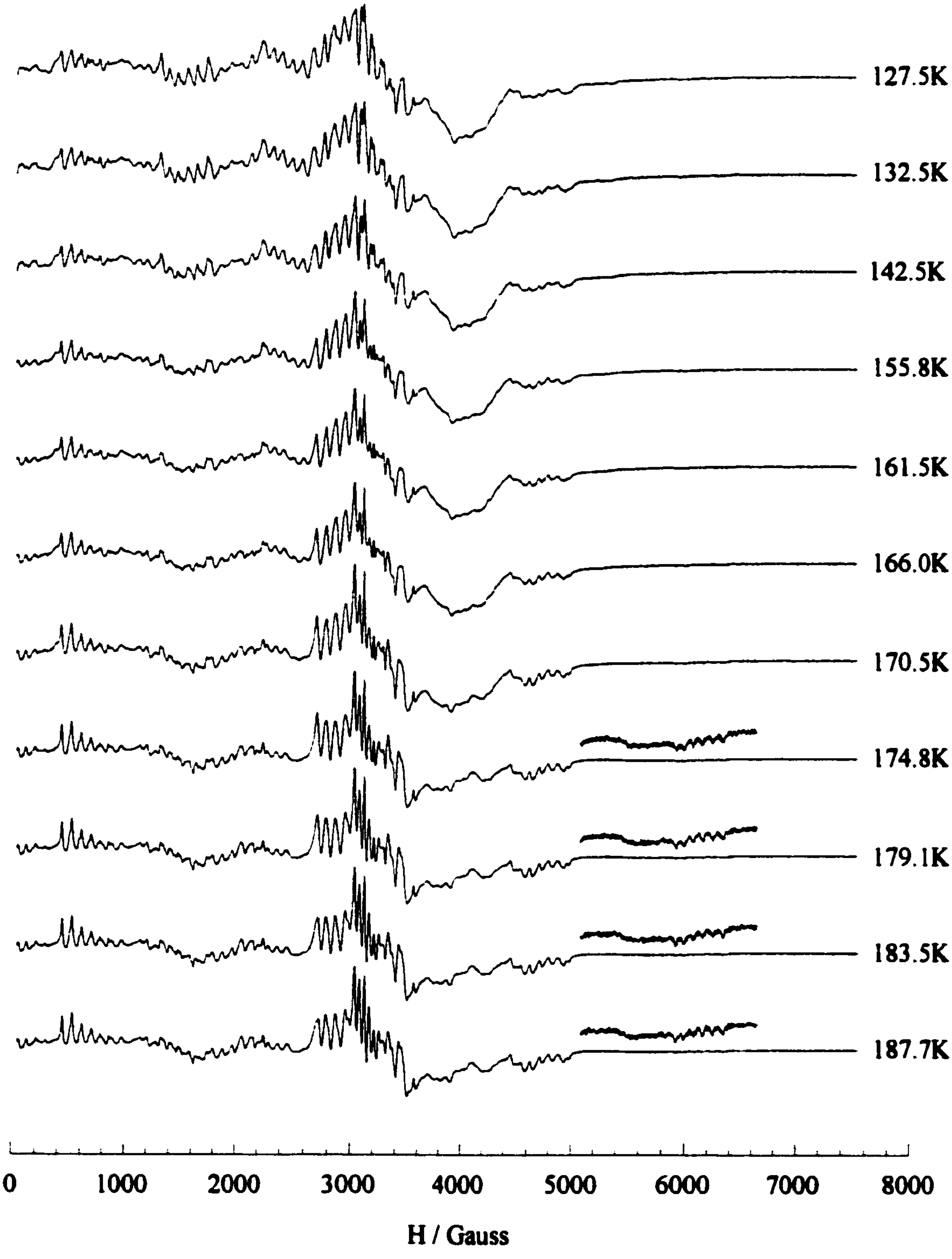

Figure 4.7.1(d) Powder ESR spectra of Mn^{2+} ion in $[Fe(bpp)_2][CF_3SO_3]_2.H_2O$ complex at increasing temperatures T* as indicated. Sample was slowly heated from 127.5K (top spectrum) to 187.7K (bottom spectrum).

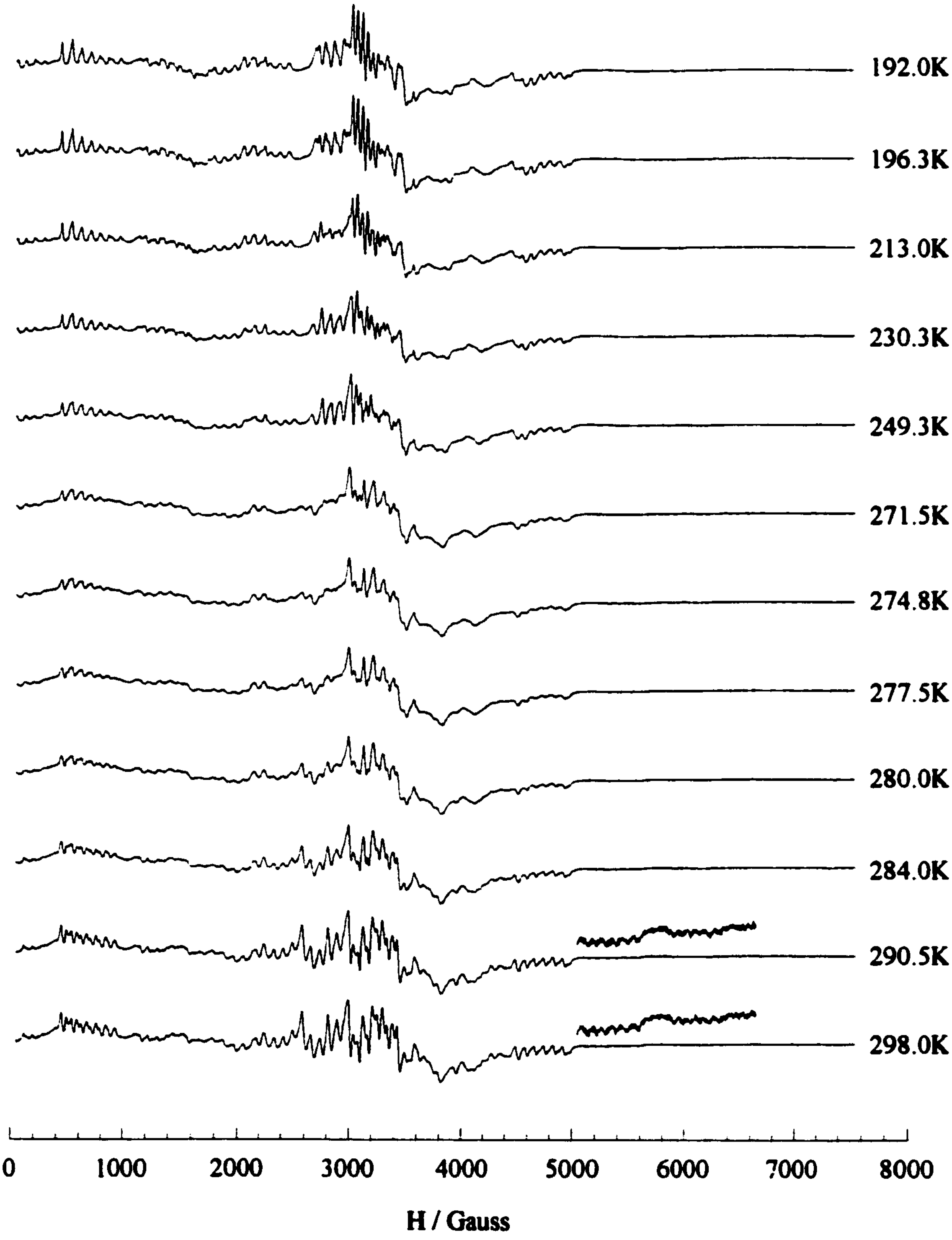

Figure 4.7.1(e) Powder ESR spectra of Mn^{2+} ion in $[Fe(bpp)_2][CF_3SO_3]_2.H_2O$ complex at increasing temperatures T* as indicated. Sample was slowly heated from 192.0K (top spectrum) to 298.0K (bottom spectrum).

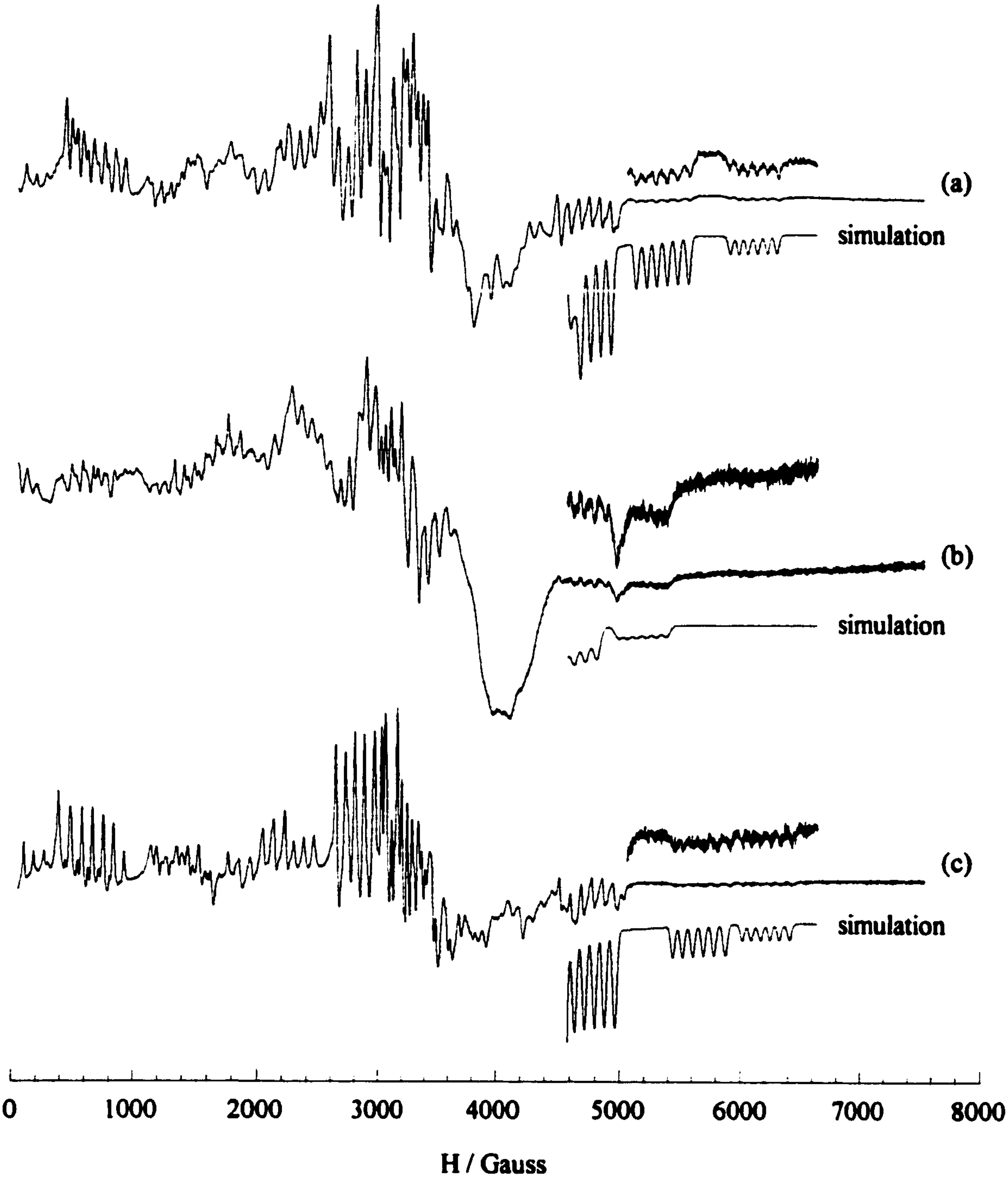

Figure 4.7.2 Powder ESR spectra of Mn^{2+} ion in $[Fe(bpp)_2][CF_3SO_3]_2.H_2O$ complex at (a) room temperature, (b) 77K after slow cooled and (c) 77K after rapid cooled. The computer-simulated spectra are obtained using parameters from Table 4.6.1. Only the high field region of the simulated spectra is shown for clearer comparison with those experimentally observed.

$[Fe(bpp)_2][BF]_2$ Complex

The powder ESR spectra given in figures 4.7.3(a) - (b) show a gradual change of spectral features for the Mn^{2+} resonance for the $S = 2$ to $S = 0$ conversion as the temperature decreases. As indicated in table 4.6.2, the D value of Mn^{2+} in the $S = 2$ system at room temperature increases as temperature is lowered to 77K as observed, also, for the $[Fe(bpp)_2][CF_3SO_3]_2.H_2O$ system. The much smaller D value for Mn^{2+} in the $S = 0$ phase at 77K indicates that there is a phase change with the HS → LS conversion. Visual observation shows a color change from yellow to red-brown during the slow cooling of the complex at 77K. This indicates that the conversion from HS → LS has occurred with the phase transformation in the lattice. The reverse change also occurs when temperature increases, which is shown by the spectra given in figure 4.7.3(c). The major features in the regions of 3200G and 4200G indicates that the spin crossover occurs at $T^* = 167.0 - 164.0K$ for the decreasing temperature and $T^* = 170.5 - 174.8K$ for the increasing temperature.

The spectrum given in figure 4.7.4(c) shows the result of the rapidly-cooled complex at liquid nitrogen temperature. The spectral features are very similar to those observed at room temperature, indicating that a change of the phase of the lattice has not occurred. This is also indicated by the D values for the $S = 2$ system at room temperature and 77K. The yellow color of the complex also remains unchanged during the rapid cooling process, indicating that the $^5T_{2g}$ spin state has been trapped in the paramagnetic form of the complex. The phase and spin state of the rapidly-cooled complex is stable over time as long as the temperature remains at 77K, but at higher temperatures the usual paramagnetic to diamagnetic phase transformation begins to set in. The change of the more prominent spectral features at about 600G, 1600G and 4200G as observed in the VT-measurements of the complex may be used to provide a quantitative measure of the formation of the diamagnetic phase of the complex. It is clear, at this stage, that the temperature-dependent HS↔LS crossover is always accompanied by a phase transformation.

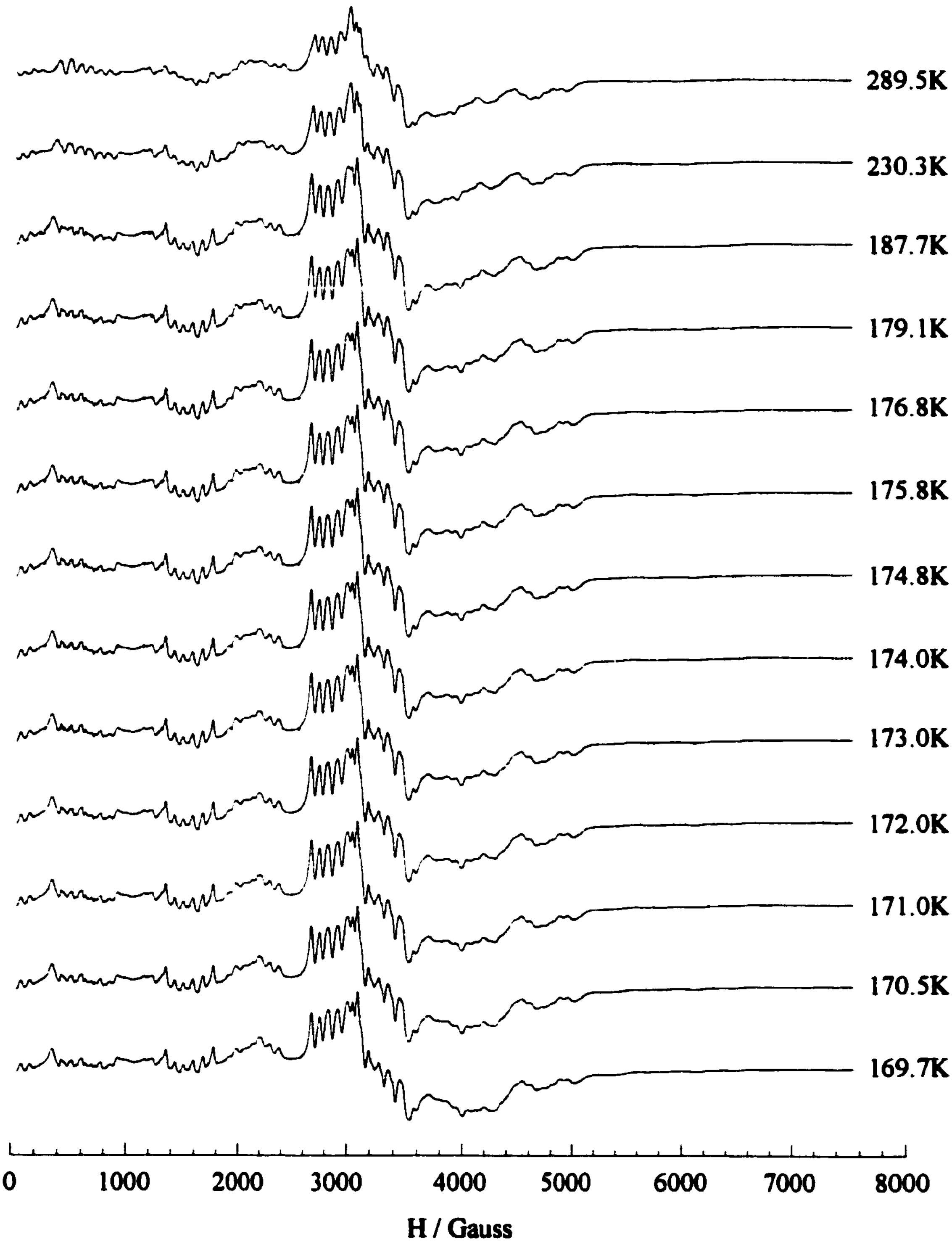

Figure 4.7.3(a) Powder ESR spectra of Mn^{2+} ion in $[Fe(bpp)_2][BF_4]_2$ complex at decreasing temperatures T* as indicated. Sample was slowly cooled from 289.5K (top spectrum) to 169.7K (bottom spectrum).

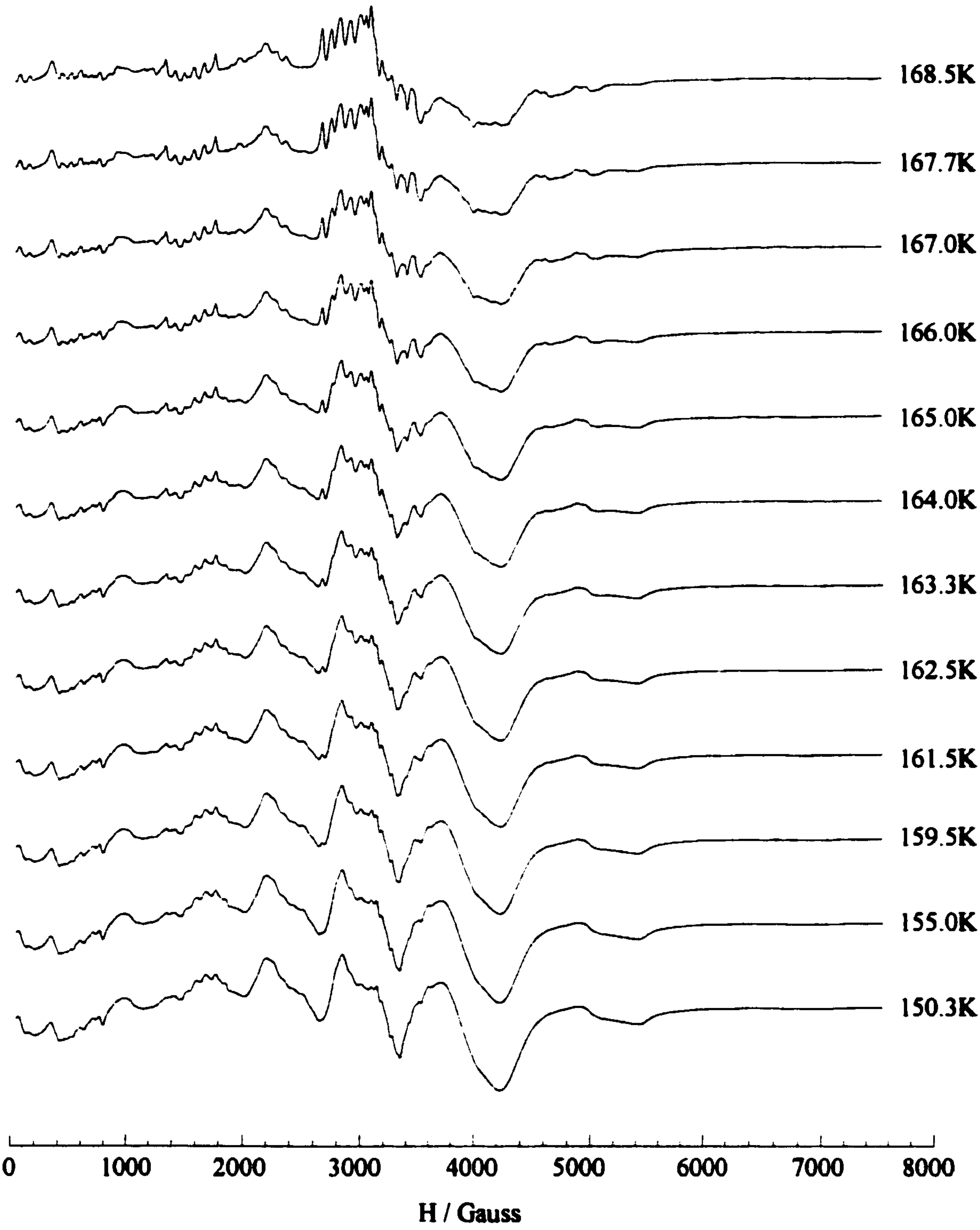

Figure 4.7.3(b) Powder ESR spectra of Mn^{2+} ion in $[Fe(bpp)_2][BF_4]_2$ complex at decreasing temperatures T* as indicated. Sample was cooled slowly from 168.5K (top spectrum) to 150.3K (bottom spectrum).

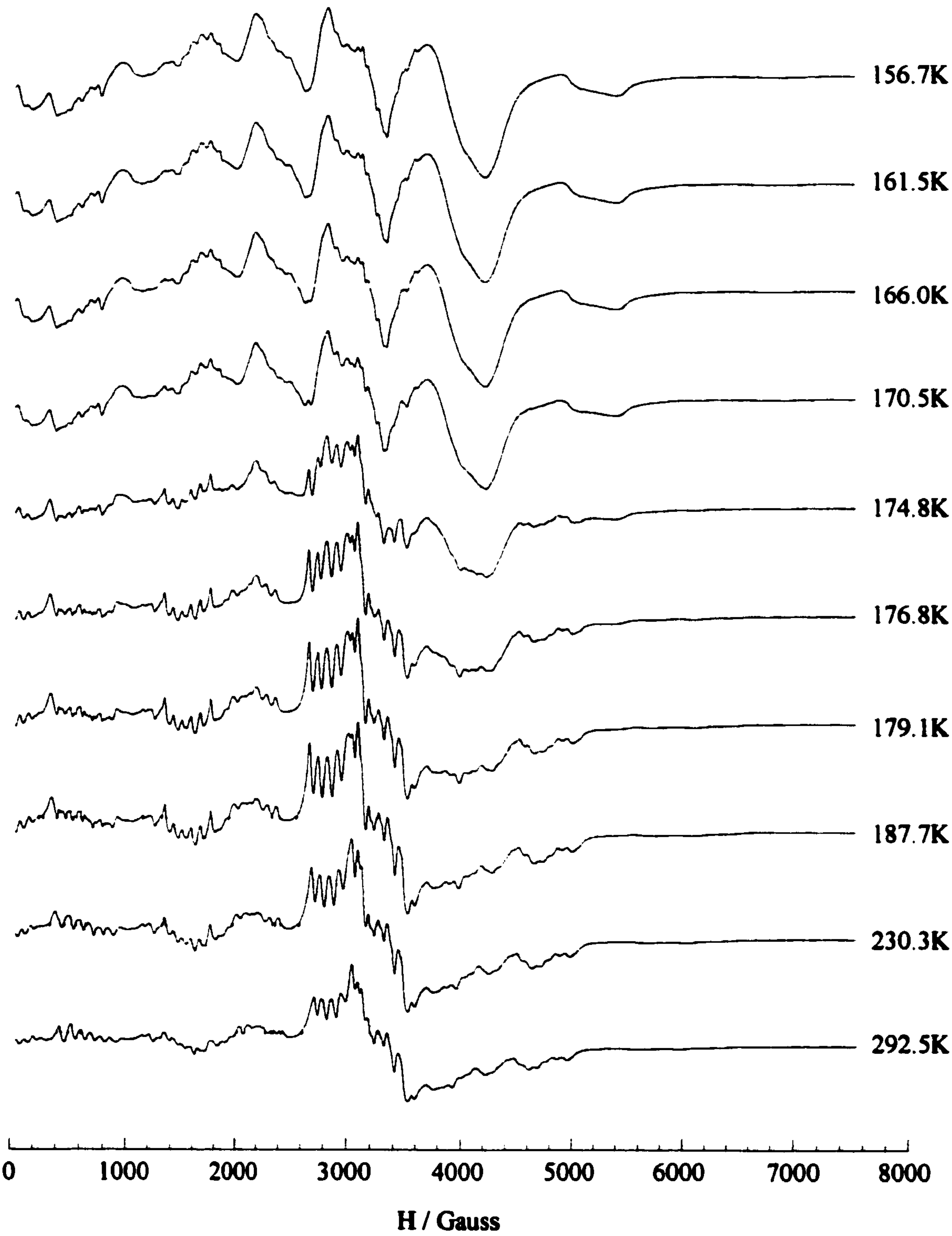

Figure 4.7.3(c) Powder spectra of Mn^{2+} ion in $[Fe(bpp)_2][BF_4]_2$ complex at increasing temperatures T* as indicated. Sample was slowly heated from 156.7K (top spectrum) to 292.5K (bottom spectrum).

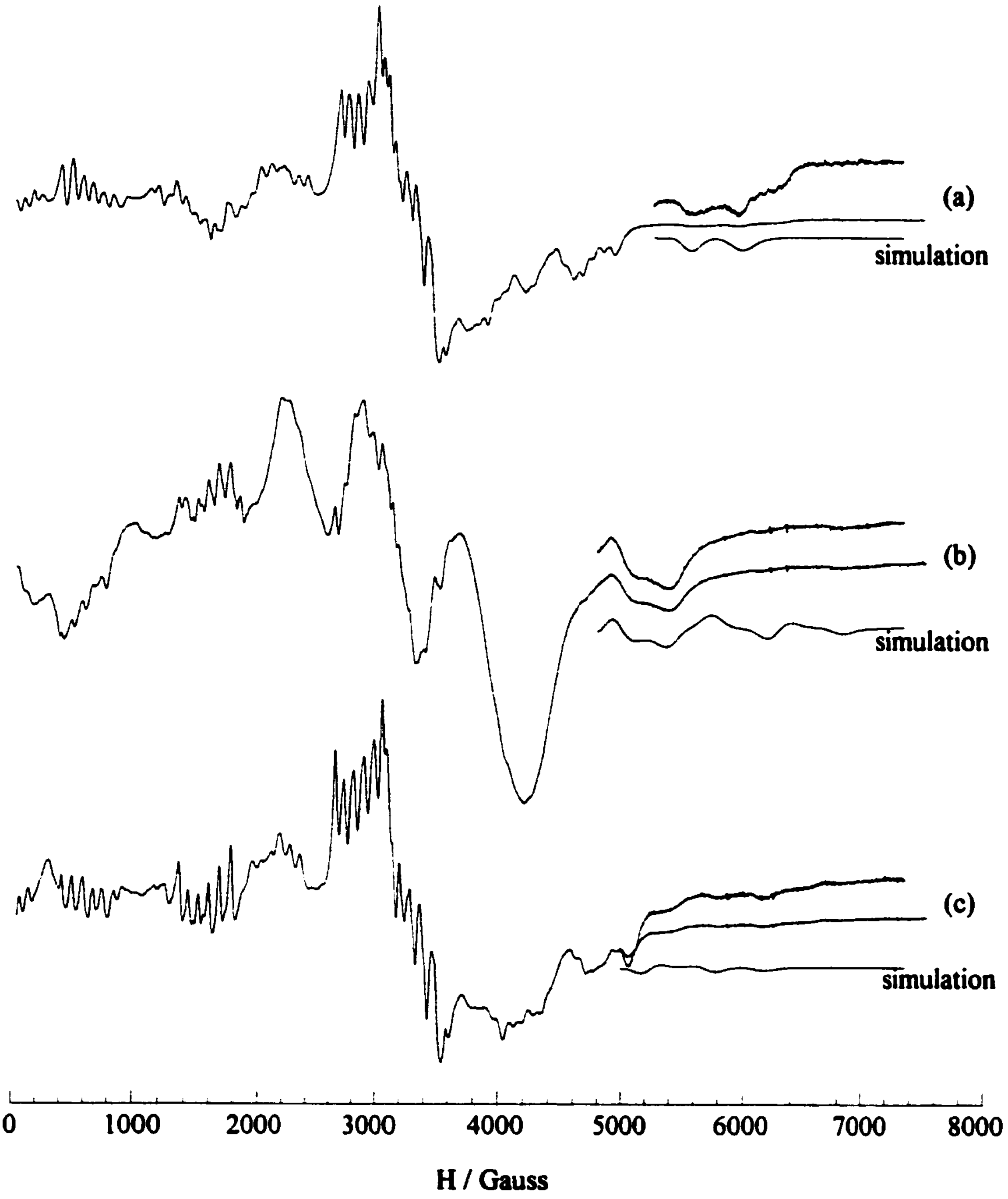

Figure 4.7.4 Powder ESR spectra of Mn^{2+} ion in $[Fe(bpp)_2][BF_4]_2$ complex at (a) room temperature, (b) 77K after slow cooled and (c) 77K after rapid cooled. The computer-simulated spectra are obtained using parameters from Table 4.6.2. Only the high field region of the simulated spectra is shown for clearer comparison with those experimentally observed.

[Fe(5-NO_2-sal-N(1,4,7,10))] Complex

The very broad, unresolved and practically featureless spectra given in figures 4.7.5(a) - (c) and 4.7.6 provide very little information for characterization of the spin crossover in the [Fe(5-NO_2-sal-N(1,4,7,10))] complex. It is apparent from the lack of a prominent peak in the g = 2 region that the condition of $D \ll g\beta_e H$ is not true. Equally the absence of a prominent peak at g ~ 6 indicates that $D \gg g\beta_e H$ is also not true. Apparently D and $g\beta_e H$ are of similar magnitude. Therefore no simulation with the simulation program is possible. There is also no evidence of a phase change seen in the ESR spectra. Visual observation of a color change in the complex has also not been possible owing to its dark-green nature. Due to a lack of extractable spectral information, further ESR study of the complex was not pursued.

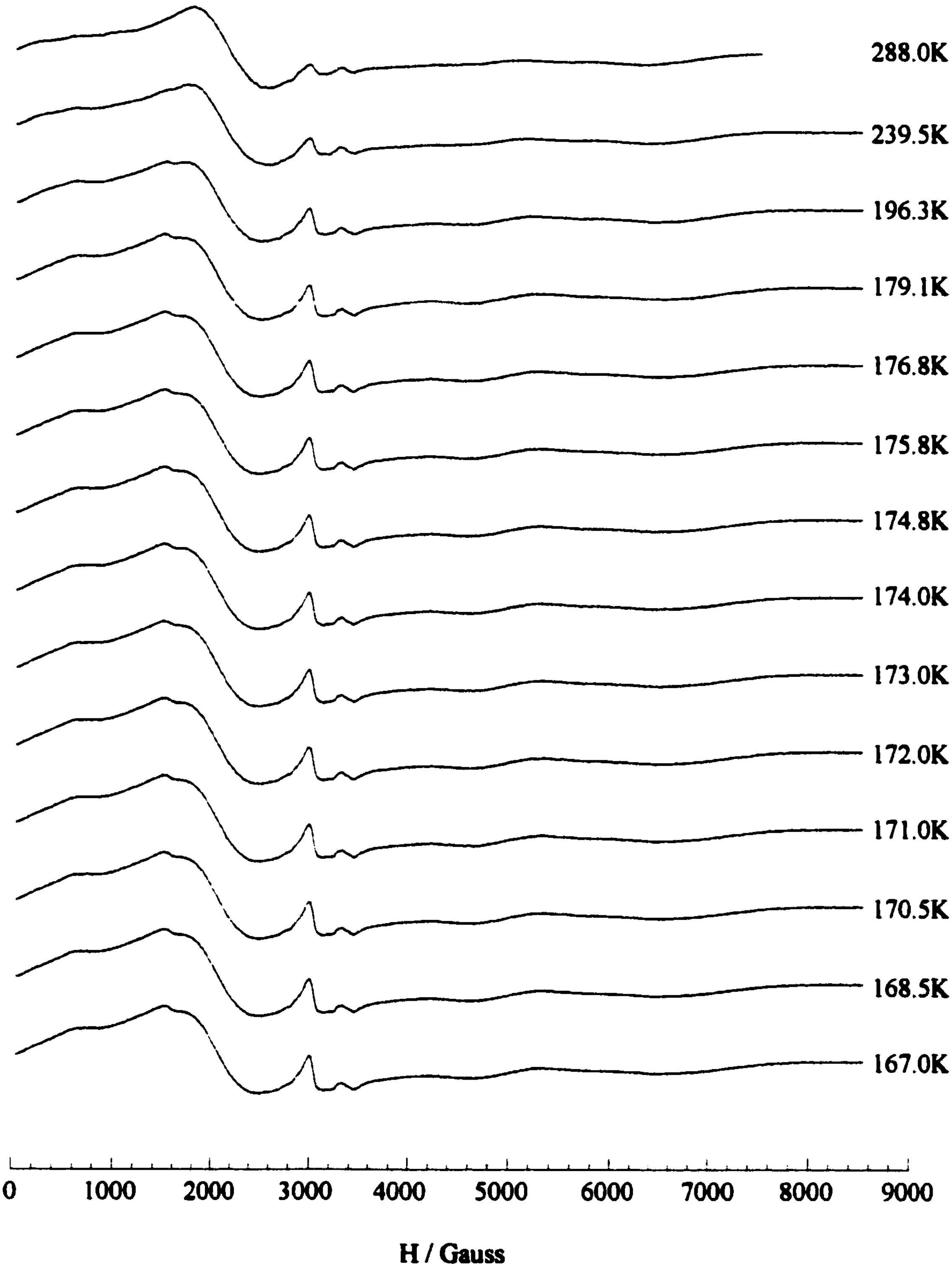

Figure 4.7.5(a) Powder ESR spectra of Mn^{2+} ion in [Fe(5-NO_2-sal-N(1,4,7,10))] complex at decreasing temperatures T* as indicated. Sample was slowly cooled from 288.0K (top spectrum) to 167.0K (bottom spectrum).

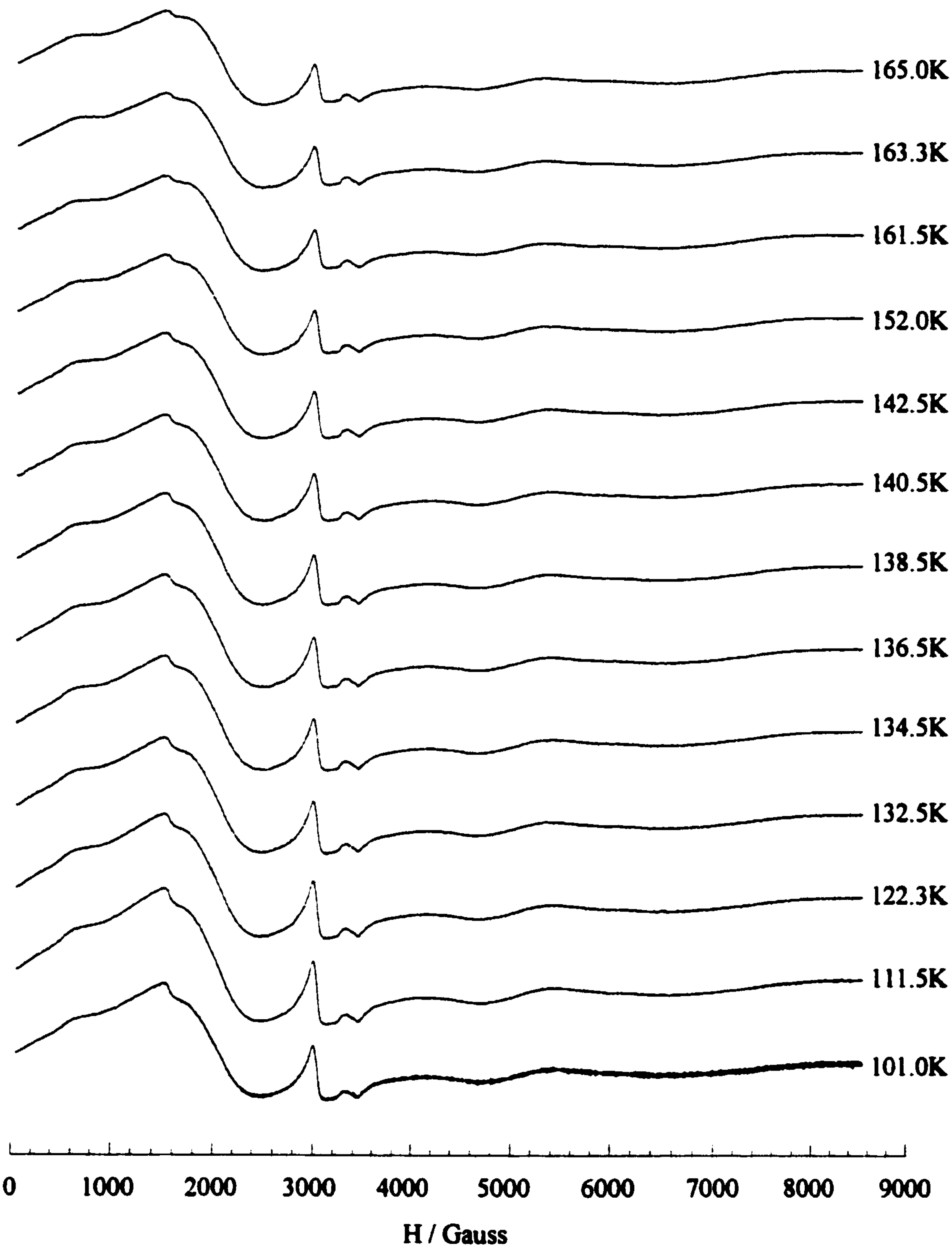

Figure 4.7.5(b) Powder ESR spectra of Mn^{2+} ion in [Fe(5-NO_2-sal-N(1,4,7,10))] complex at decreasing temperatures T* as indicated. Sample was slowly cooled from 165.0K (top spectrum) to 101.0K (bottom spectrum).

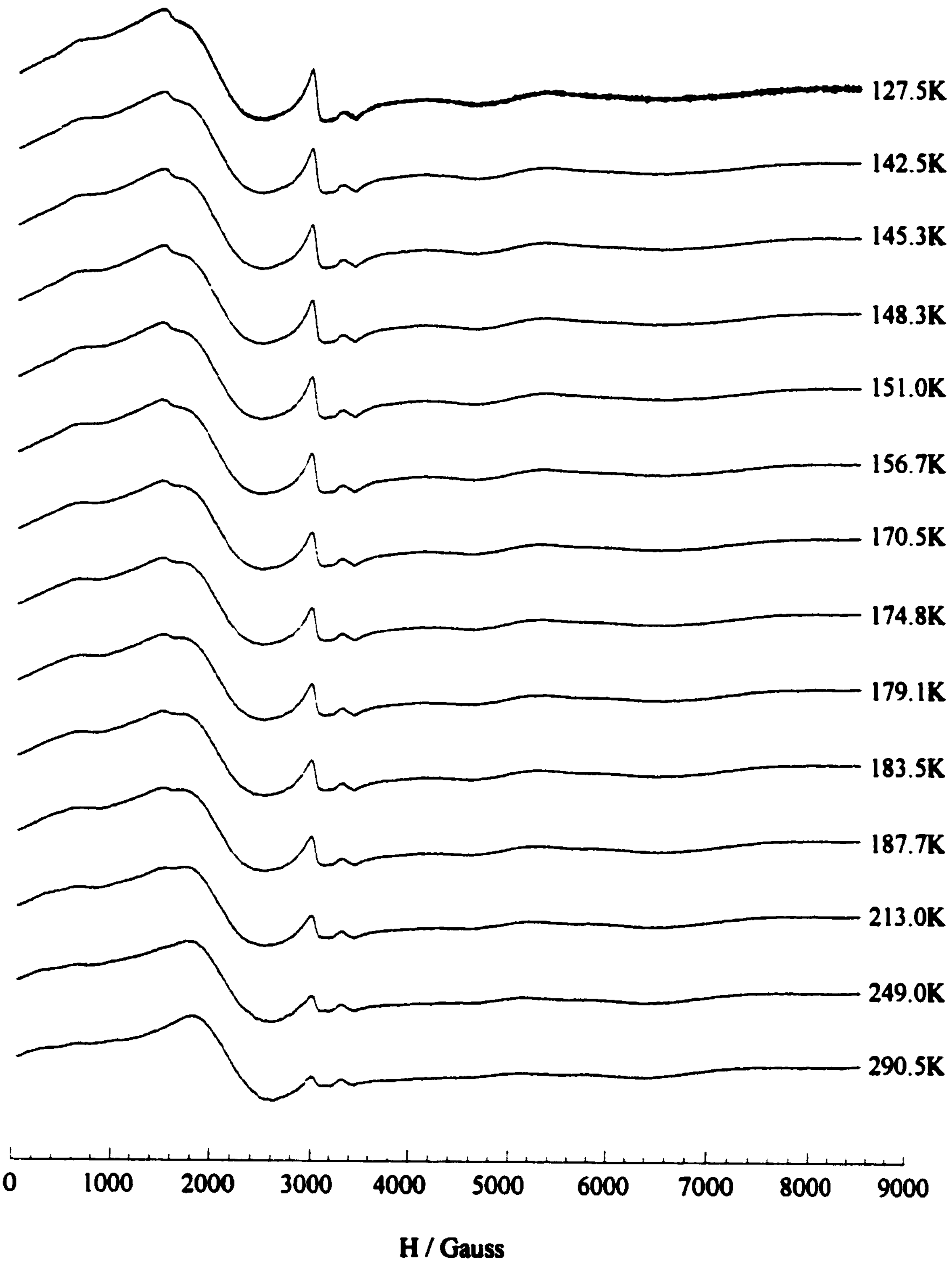

Figure 4.7.5(c) Powder ESR spectra of Mn^{2+} ion in $[Fe(5\text{-}NO_2\text{-sal-N}(1,4,7,10))]$ complex at increasing temperatures T* as indicated. Sample was slowly heated from 127.5K (top spectrum) to 290.5K (bottom spectrum).

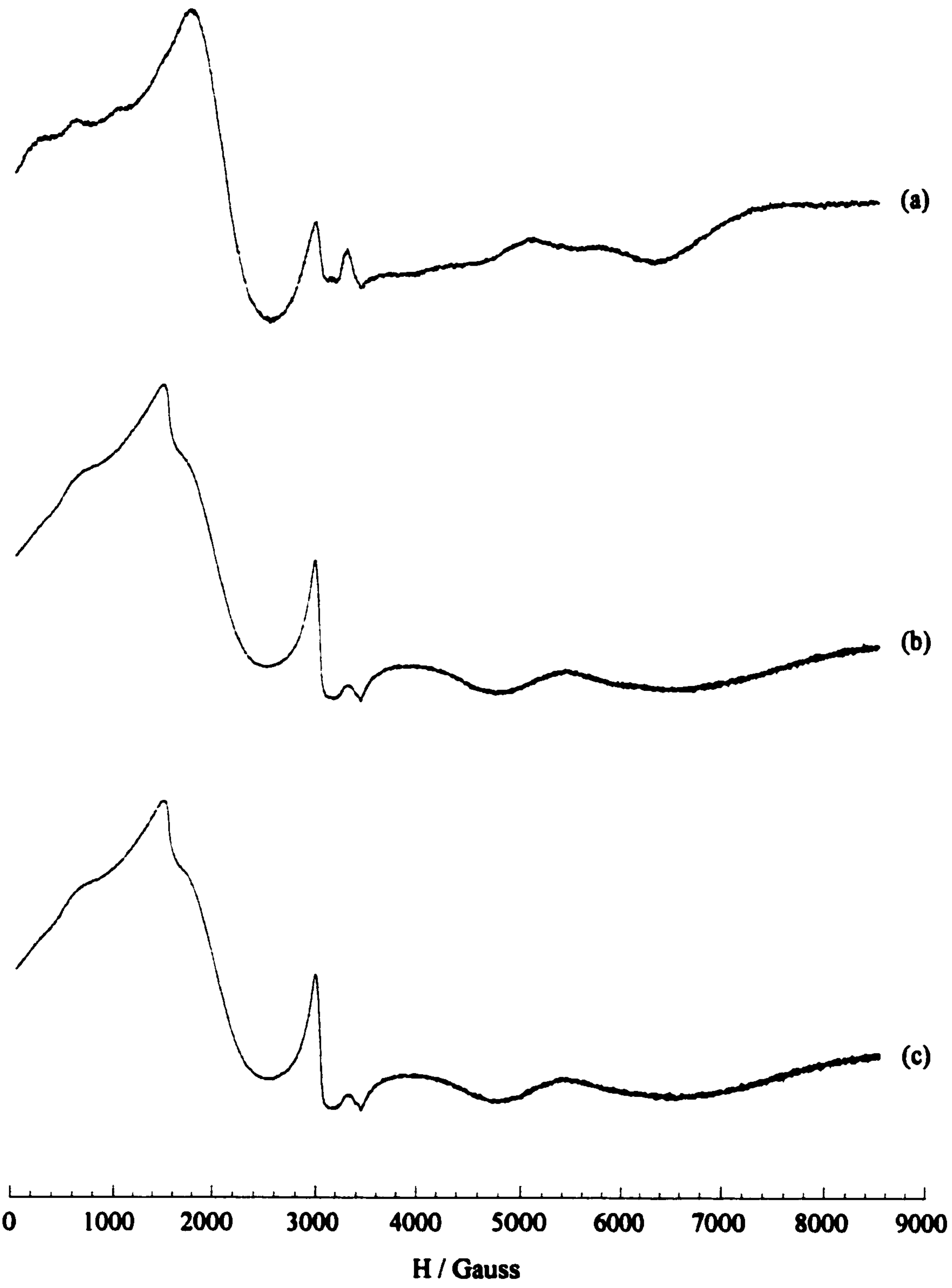

Figure 4.7.6 Powder ESR spectra of Mn^{2+} ion in [Fe(5-NO_2-sal-N(1,4,7,10))] complex at (a) room temperature, (b) 77K after slow cooled and (c) 77K after rapid cooled.

CHAPTER 5

IRRADIATION EXPERIMENTS

5.1 Introduction

The well known LIESST and the reverse LIESST effects have been reported[58,59,62-68,72,73,77] to occur in many Fe^{2+} spin crossover complexes at temperatures well below their critical temperatures. The mechanism of the effects has also been proposed by Decurtins[58,59] and later proved to be correct by Hauser[65] In the LIESST studies, a beam of light with a suitable wavelength of *ca.* 514.5 nm is generally used to induce the ${}^1A_{1g} \rightarrow {}^5T_{2g}$ spin-state transition, and the reverse change may also occur by using a beam of light with a different wavelength of *ca.* 800 nm. In most of the Fe^{2+} spin crossover systems studied so far, a very low temperature below 50K is usually required to observe the effect. For example in the $[Fe(ptz)_6][BF_4]_2$ complex, the system has to be cooled to *ca.* 20K in order for the effects to be experimentally observed. Both Mössbauer spectroscopy and magnetic susceptibility measurements have been extensively used to study the light induced ${}^5T_{2g} \leftrightarrow {}^1A_{1g}$ spin-state transition.

Both LIESST and reverse LIESST effects have been found in the $[Fe(bpp)_2][CF_3SO_3]_2.H_2O$ by Buchen *et al.*[73], and $[Fe(bpp)_2][BF_4]_2$ by Goodwin and Sugiyarto[72] and by Buchen *et al.*[68] These complexes undergo the HS ↔ LS crossover with a color change, the HS state of both complexes being yellow and the LS state of the first complex is orange-brown and that the second complex is red-brown. There is no direct proof of a phase change occurring in both of the complexes during the spin crossover, it is only inferred from the thermal hysteresis behavior in both cases. In the Buchen *et al.*[73] studies of the $[Fe(bpp)_2][CF_3SO_3]_2.H_2O$ complex, a complete LS → HS transition has been observed during LIESST, but the reverse change is partial with only *ca.* 10% LS state formed in reverse LIESST. LIESST effect in the $[Fe(bpp)_2][BF_4]_2$ complex has been observed at a temperature ≤ 80K, the LS → HS transition is complete but the reverse change is also partial with only *ca.* 5% conversion of HS state in the reverse LIESST. The present ESR studies of the irradiation effects on the $[Fe(bpp)_2][CF_3SO_3]_2.H_2O$ and $[Fe(bpp)_2][BF_4]_2$ complexes were undertaken because these workers[72,73] have shown that both the effect can be experimentally observed at temperatures above 77K. It was hoped that the experimental results may provide more information concerning the relationship between the spin-state transition and the phase transformation in the lattice.

5.2 Experimental Procedures

The irradiation experiments were performed on powder samples of $[Fe(bpp)_2][CF_3SO_3]_2.H_2O$ and $[Fe(bpp)_2][BF_4]_2$ complexes at 77K using a Lexel 95 Ar-laser operating at 100mW power and a Spectra Physics 2000 Kr-laser operating at 50mW power. All samples were cooled from room temperature to 77K in the 50 ml finger Dewar flask outside the microwave cavity, the subsequent irradiation of the cooled samples was also done outside the microwave cavity. Extreme caution was taken to ensure that the sample volume was properly and uniformly irradiated. This was done by slowly moving the finger portion, containing the sample tube, of the Dewar flask vertically up and down in the light beam. A very small turning was applied to bring the adjacent side of the sample tube in the light beam, then followed by the vertical motion. ESR spectra of Mn^{2+} ion in the complexes were recorded after each irradiation. They were acquired using a microwave power 20mW, microwave frequency 9.5GHz, modulation frequency 100kHz, modulation amplitude 4.062G and 4k data points covering a magnetic field range 50G - 7500G.

The $[Fe(bpp)_2][CF_3SO_3]_2.H_2O$ complex was slowly cooled from room temperature to 77K, it was then irradiated with the Ar-laser at 514.5 nm for 20 minutes. The color of the sample changed from orange-brown to yellow. This was followed by irradiating with the Kr-laser at 676.0 nm for 20 minutes, and the color remained yellow. The ESR results are given in figures 5.3.1(a) - (c). The sample was then allowed to warm up to room temperature, it was slowly cooled to 77K again. This was then irradiated only with the Kr-laser for 90 minutes, the color of the sample also changed from orange-brown to yellow. The ESR result is given in figure 5.3.1(d). The same sample was then allowed to warm up to room temperature again, it was rapidly cooled to 77K by plunging directly into liquid nitrogen. This was irradiated only with the Kr-laser for 20 minutes, and the color remained yellow. The ESR result is given in figure 5.3.1(f)

The same procedure was used in the irradiation studies of $[Fe(bpp)_2][BF_4]_2$ complex. The $[Fe(bpp)_2][BF_4]_2$ complex was slowly cooled from room temperature to 77K, it was then irradiated with the Ar-laser at 514.5 nm for 12 minutes. The color of the sample changed from red-brown to yellow. This was followed by irradiating the sample with the Kr-laser at 676.0 nm for 11 minutes. The color of the sample remained yellow. The ESR results are given in figures 5.3.2(a) - (c). The sample was then allowed to warm up to room temperature, it was slowly cooled to 77K again. This was irradiated with only the Kr-laser for 30 minutes. The color of the sample also changed from red-brown to yellow. The ESR result is given in figure 5.3.2(d). The same sample was then allowed to warm up to room temperature again, it was rapidly cooled to 77K by plunging directly into liquid nitrogen. This was irradiated only with the Kr-laser again for 20 minutes, and the color of the sample also remained yellow. The ESR result is given in figure 5.3.2(f).

5.3 Results and Discussion

$[Fe(bpp)_2][CF_3SO_3]_2.H_2O$ Complex

The orange-brown diamagnetic form of the Mn^{2+} doped complex with S = 0 and the yellow paramagnetic form with S = 2 at 77K are shown in figures 5.3.1(a) and 5.3.1(e), respectively. The results from temperature dependence studies show the spin crossover is accompanied by a phase change and that during the transition there are separate domains for each spin-state. The irradiation of the S = 0 system at 77K using the Ar-laser has produced no change in the Mn^{2+} spectrum in the LS phase of the $[Fe(bpp)_2][CF_3SO_3]_2.H_2O$ complex, this can be seen in figure 5.3.1(b). However, visual observation detects a color change from orange-brown to yellow, indicating that the LS

→ HS transition has occurred. The subsequent irradiation of the same system using the Kr-laser has produced neither a color change nor phase change. As shown in figure 5.3.1(c), all the spectral features of Mn^{2+} in the system remain practically the same as those observed for the S = 0 system. The unchanged yellow color indicates the reverse HS → LS transition has not occurred. Figure 5.3.1(d) shows the results after irradiating the S = 0 system at 77K using the Kr-laser only, the Mn^{2+} spectrum also remains identical to that in the LS phase, but this time the color of the complex changes from orange-brown to yellow which again is indicative of the LS → HS transition. It appears that the lattice for the HS state created by irradiation of the LS state is identical to that of the LS state. Additional evidence is also seen in the result given in figure 5.3.1(f) after the S = 2 system at 77K has been irradiated with the Kr-laser. The Mn^{2+} spectrum in the HS phase of the complex is practically identical to that given in figure 5.3.1(e) also no color change is observed. The important result of these experiments is that the LIESST effect observed at these temperatures does not involve the phase transformation observed in the thermal spin crossover. Further no reverse LIESST effect has been observed for HS state in either the LS or HS phase.

$[Fe(bpp)_2][BF_4]_2$ complex

This complex has an almost identical behavior as that observed for the $[Fe(bpp)_2][CF_3SO_3]_2.H_2O$ Complex. The color of the LS and HS states are red-brown and yellow, respectively, and as shown in the temperature dependence studies that the HS ↔ LS transition is always accompanied by a phase transformation of the system. The Mn^{2-} spectrum in the LS phase is given in figure 5.3.2(a), all the spectral features of Mn^{2-} in the system are different from that given in figure 5.3.2(e) for the HS phase at 77K. Figure 5.3.2(b) shows the result after irradiating the LS phase at 77K using Ar-laser, the Mn^{2+} spectrum remains practically identical to that given in figure 5.3.2(a) indicating that the LS → HS phase transformation has not occurred. Visual observation detects a color change from red-brown to yellow, indicating that the HS → LS transition has occurred. The subsequent irradiation of the same system using the Kr-laser has produced neither a color change nor phase change. As shown in figure 5.3.2(c), the same Mn^{2+} spectrum in the LS phase is seen. The unchanged yellow color indicates the reverse HS → LS transition has not occurred. The Mn^{2+} spectrum given in figure 5.3.2(d), after irradiating the slow cooled system at 77K using only the Kr-laser, is also identical to that given in figure 5.3.2(a). This time, the color changed from red-brown to yellow indicating that the LS → HS transition has occurred. It also appears that, in the $[Fe(bpp)_2][BF_4]_2$ system, the lattice for the HS state created by irradiation of the LS state is also identical to that of the LS state. Additional evidence is also seen in the result given in figure 5.3.2(f) after rapidly cooled system at 77K has been irradiated with Kr-laser only. The Mn^{2+} spectrum in the HS phase of the system is also identical to that given in figure 5.3.2(e), and also, no color change is observed. The conclusion from these experiments is also similar to that given for the $[Fe(bpp)_2][CF_3SO_3]_2.H_2O$ system. The LIESST effect observed at 77K does not involve phase transformation as observed in the thermal spin crossover, and no reverse LIESST effect has been observed for HS state in either the LS or HS phase.

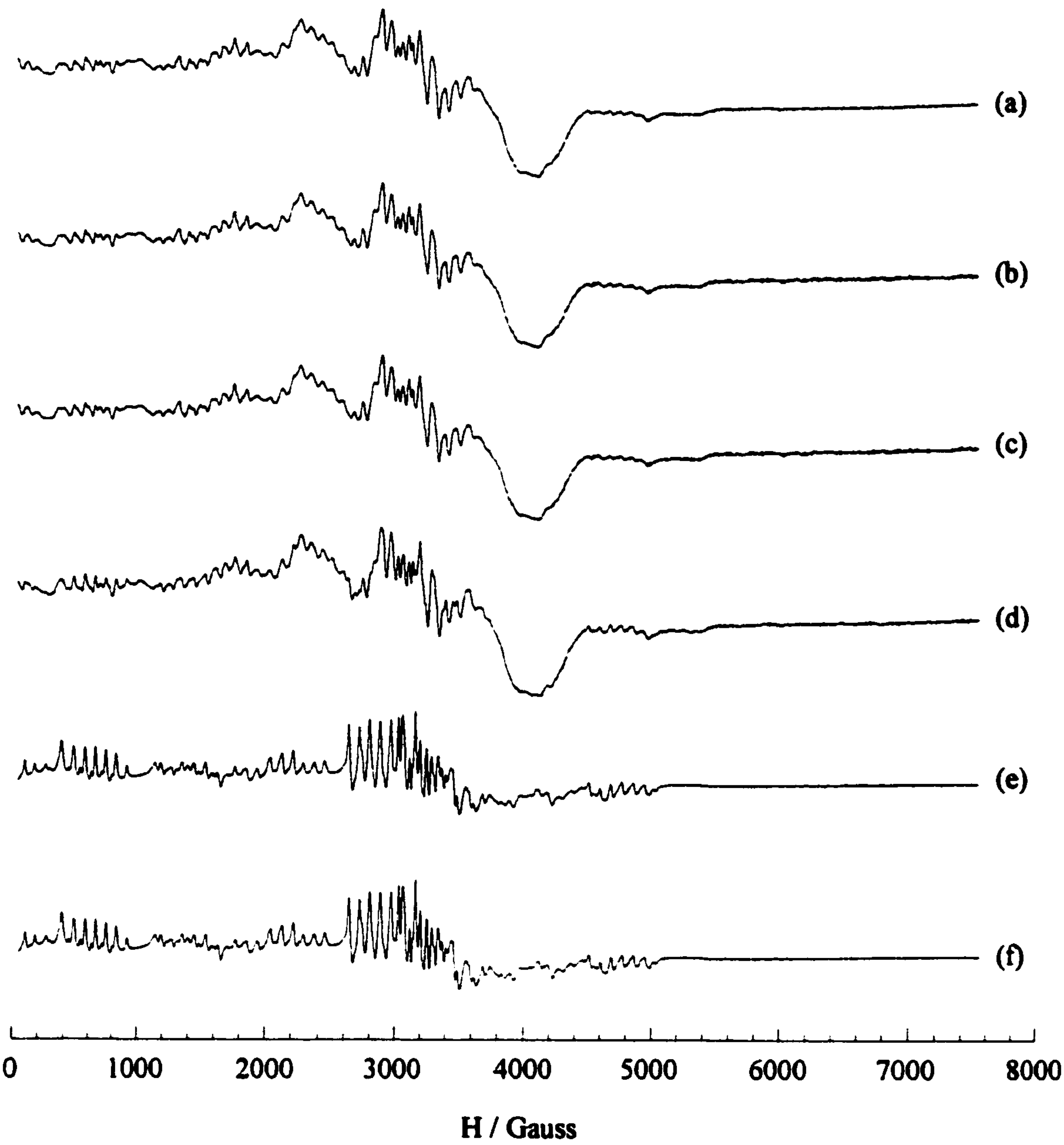

Figure 5.3.1 Powder ESR spectra of Mn^{2+} ion in $[Fe(bpp)_2][CF_3SO_3]_2.H_2O$ complex at 77K after various treatments.

(a) spectrum of a sample slowly cooled to 77K, spin state S = 0.

(b) spectrum of S = 0 sample, (a), after irradiation by Ar-laser for 20 min.

(c) spectrum of sample shown in (b) after an additional irradiation by Kr-laser for 20 min.

(d) spectrum of S = 0 sample, (a), after irradiation by Kr-laser for 90 min.

(e) spectrum of a sample rapidly cooled to 77K, spin state S = 2.

(f) spectrum of S = 2 sample, (e), after irradiation by Kr-laser for 20 min.

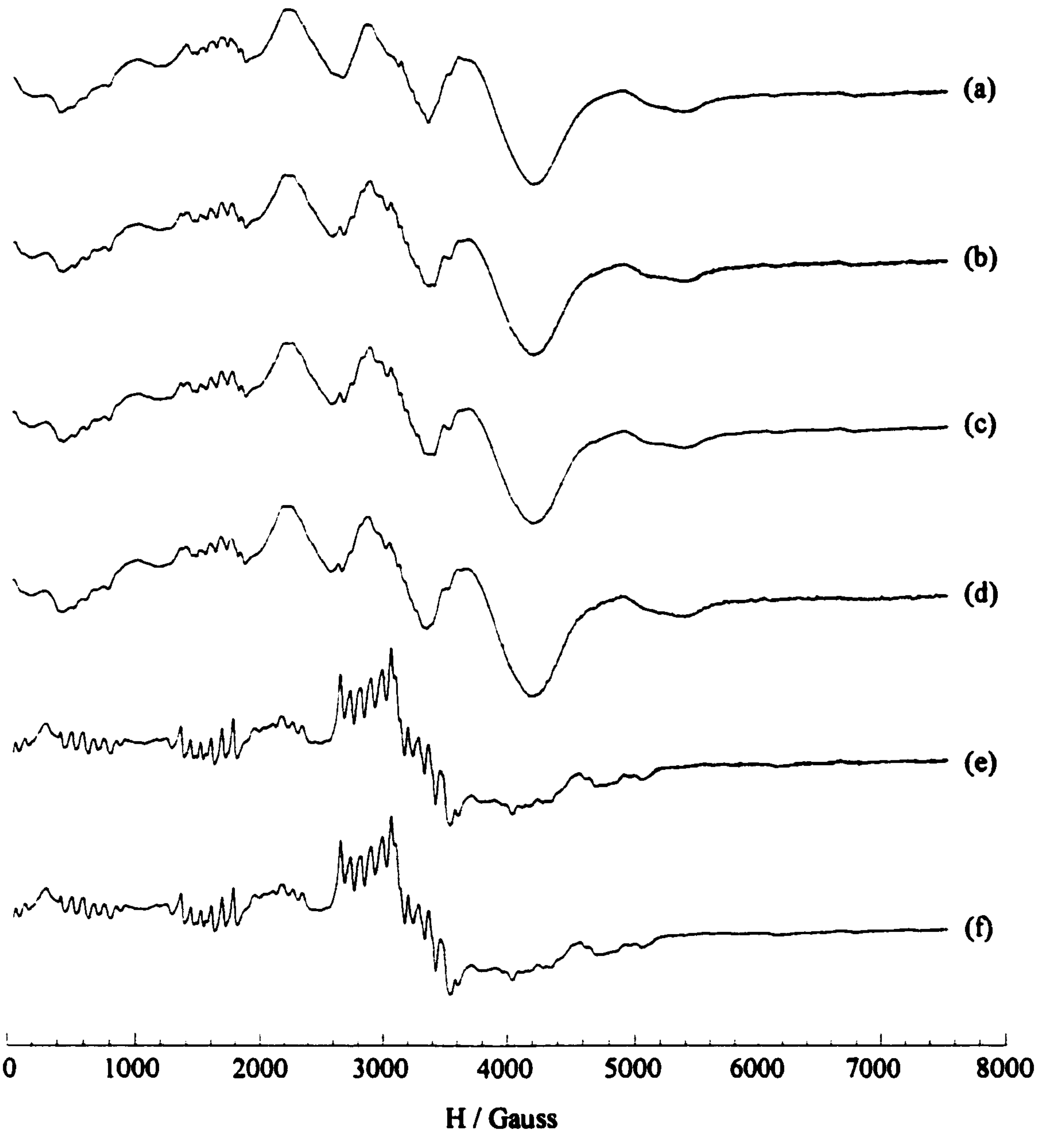

Figure 5.3.2 Powder ESR spectra of Mn^{2+} ion in $[Fe(bpp)_2][BF_4]_2$ complex at 77K after various treatments.

(a) spectrum of a sample slowly cooled to 77K, spin state S = 0.

(b) spectrum of S = 0 sample, (a), after irradiation by Ar-laser for 12 min.

(c) spectrum of sample shown in (b) after an additional irradiation by Kr-laser for 11 min.

(d) spectrum of S = 0 sample, (a), after irradiation by Kr-laser for 30 min.

(e) spectrum of a sample rapidly cooled to 77K, spin state S = 2.

(f) spectrum of S = 2 sample, (e), after irradiation by Kr-laser for 20 min.

CHAPTER 6

KINETICS OF HS → LS PHASE TRANSFORMATION

6.1 Introduction

Buchen *et al.*[73] studied the kinetics of the HS → LS transition in the $[Fe(bpp)_2][CF_3SO_3]_2.H_2O$ system using Mössbauer spectroscopy and magnetic susceptibility measurements. Both the LIESST effect and rapidly cooling method were used to generate the HS state in the system. The subsequent HS → LS transition for the LIESST generated HS state was followed by Mössbauer spectroscopy over the temperature range 77.5 - 85K, and for that produced by rapidly cooling method was followed by magnetic susceptibility measurements over the temperature range 104 - 118K. Their results suggest that the mechanism of the spin-state transition for the LIESST generated HS state is different from that observed for the thermally produced HS state, and that the latter change is caused by a phase transformation of the system.

The kinetics of the HS → LS crossover in the $[Fe(bpp)_2][BF_4]_2$ system was first studied by Goodwin *et al.*[72] using the rapidly cooling method to generate the HS state, and first order kinetics was reported for the spin-state transition. In the system prepared by the rapidly cooling to liquid nitrogen temperature, the HS → LS transition was followed by magnetic susceptibility over the temperature range 99 - 114K. A phase transformation was also inferred from the thermal hysteresis behavior of the system. The same complex was later reinvestigated by Buchen *et al.*[68] using both the rapid cooling method and the LIESST effect to generate the HS state and Mössbauer spectroscopy to follow the subsequent HS → LS transition over the temperature range 92.5 - 100K. In the Buchen *et al.* results[68], the spin-state transition for the HS state produced by the rapidly cooling method showed a sigmoidal behavior rather than a first-order kinetics. The rate of conversion to the LS state was similar for both methods of preparation. It was postulated that the surprisingly long lifetime for the excited HS state was due to a phase change and that the phase change rate determined the rate of change from HS to

LS. A similar study was done by Buchen *et al.*[73] for $[Fe(bpp)_2][CF_3SO_3]_2.H_2O$, in this case LIESST was done at 80K rather than the 20K used in the earlier study on $[Fe(bpp)_2][BF_4]_2$. In this case the rate of change from HS to LS was considerably slower when the HS state was formed by rapid cooling than when it was formed by the LIESST effect. In both cases no conversion was observed until the temperature was above 90K, again the slow conversion rate was attributed to a phase conversion.

The ESR investigation of the HS $\rightarrow$ LS phase transformation in the $[Fe(bpp)_2][CF_3SO_3]_2.H_2O$ and $[Fe(bpp)_2][BF_4]_2$ system was done in hope that the experimental results might provide valuable information to give a better understanding of the kinetics between the HS $\rightarrow$ LS phase transformation and the spin-state transition in the systems. This is probably the first time that the application of ESR in the kinetic studies of the phase transformation in these Fe^{2-} spin crossover systems has been attempted. The use of Mn^{2+} ion as an ESR probe is based on the experience that the ion is very sensitive to changes of its surrounding environment, enabling a direct measure of the phase transformation in the systems.

6.1 Experimental Procedures

The ESR studies of the paramagnetic to diamagnetic phase transformation in the $[Fe(bpp)_2][CF_3SO_3]_2.H_2O$ complex were done at 104.3K and 119.6K, using the 50 ml finger Dewar flask and the VT-Dewar associated with the variable temperature unit. The sample was rapidly cooled from room temperature to 77K by plunging directly into liquid nitrogen contained in the finger Dewar flask outside the microwave cavity. The color of the sample remained yellow during the cooling process. It was then quickly transferred into the VT-Dewar mounted inside the microwave cavity at the preset temperature of 104.3K. The temperature of the sample was controlled at $\pm 0.1K$ by the Bruker B-VT2000 nitrogen-flow variable temperature control unit. Powder ESR spectra of Mn^{2+} ion in the complex were then recorded at different time intervals. The same study was also done at 119.6K. The ESR results are given in figures 6.3.1(a) - (b) and 6.3.2, respectively. All the spectra were acquired using a microwave power 20mW, microwave frequency 9.5GHz, modulation frequency 100kHz, modulation amplitude 4.062G and 4k data points covering a magnetic field range from 50G to 7500G.

The same experimental procedure was also used in the ESR studies of the paramagnetic to diamagnetic phase transformation in the $[Fe(bpp)_2][BF_4]_2$ complex at 99K and 104.7K, and the ESR results are given in figures 6.3.5 and 6.3.6, respectively. All spectra were acquired using the same experimental conditions as those for the $[Fe(bpp)_2][CF_3SO_3]_2.H_2O$ complex.

6.3 Results and Discussion

$[Fe(bpp)_2][CF_3SO_3]_2.H_2O$ complex

The powder ESR spectra of Mn^{2+} in $[Fe(bpp)_2][CF_3SO_3]_2.H_2O$ complex as given in figures 6.3.1(a) - (b) and 6.3.2 show a continuous phase transformation of the system during the HS → LS transition at 104.3K and 119.6K, respectively. The gradual disappearance of the HS phase in the system is clearly indicated by the decreases of intensity in the more prominent spectral features in the regions 600G, 1400G, and 4800G. In contrast to these, the increases in the intensity of the spectral features in the region 4000G reflects the increases in the LS phase in the system. The determination of either the increases or the decreases of the HS or LS phase can be achieved by using any of the above Mn^{2+} features characteristic of the phase. For a better and clearer comparison with the results reported by Buchen *et al.*[73] in their kinetic studies of the HS → LS transition over the similar temperature range, the Mn^{2+} spectral features in the region 600G were used as a quantitative measure of the disappearance of the HS phase in the system. The Mn^{2+} spectrum obtained after a long time was subtracted from each of those obtained at different times to determine the intensity $[I(t) - I(t \sim \infty)]$. The results are given in figure 6.3.3. It can be clearly seen that the HS phase reaches a minimum in about 25 - 30 minutes at 119.6K and 160 minutes at 104.3K which are comparable to the time scales in the Buchen *et al.* results[73], reproduced as shown in figure 6.3.4, during their kinetic studies of the HS → LS transition of a sample when the HS state was prepared by rapid cooling at 118K and 104K, respectively. The important result of the present study is that the HS → LS phase transformation follows a curve very similar to that for the HS → LS transition in the system.

$[Fe(bpp)_2][BF_4]_2$ complex

The $[Fe(bpp)_2][BF_4]_2$ system has a very similar behavior as that observed in the $[Fe(bpp)_2][CF_3SO_3]_2.H_2O$ system. The powder ESR spectra of Mn^{2+} given in figures 6.3.5 and 6.3.6 also show a continuous HS → LS phase transformation at 99K and 104.7K, respectively. The same method used in the $[Fe(bpp)_2][CF_3SO_3]_2.H_2O$ system was also used to determine the intensity $[I(t) - I(t \sim \infty)]$. In order to compare the results from this study with the results reported by Buchen *et al.*[68] in their kinetic studies of the HS → LS transition over the temperature range 92.5 - 100K, the Mn^{2+} features in the region 600G were also used as a quantitative measure of the disappearance of the HS phase during the HS → LS transformation. The results are given in figure 6.3.7. It appears that the HS phase reaches the same minimum in about 85 - 90 minutes at both temperatures, suggesting that the rate of the HS → LS phase transformation is similar at 99K and 104.7K. In the Buchen *et al.* results[68], reproduced as shown in figure 6.3.8, the time required for the HS state to decay to a minimum during the HS → LS transition is about 167 minutes at 100K. The conclusion from this study indicates that the HS → LS phase transformation in the $[Fe(bpp)_2][BF_4]_2$ system occurs at twice the rate of the spin-state transition in the system.

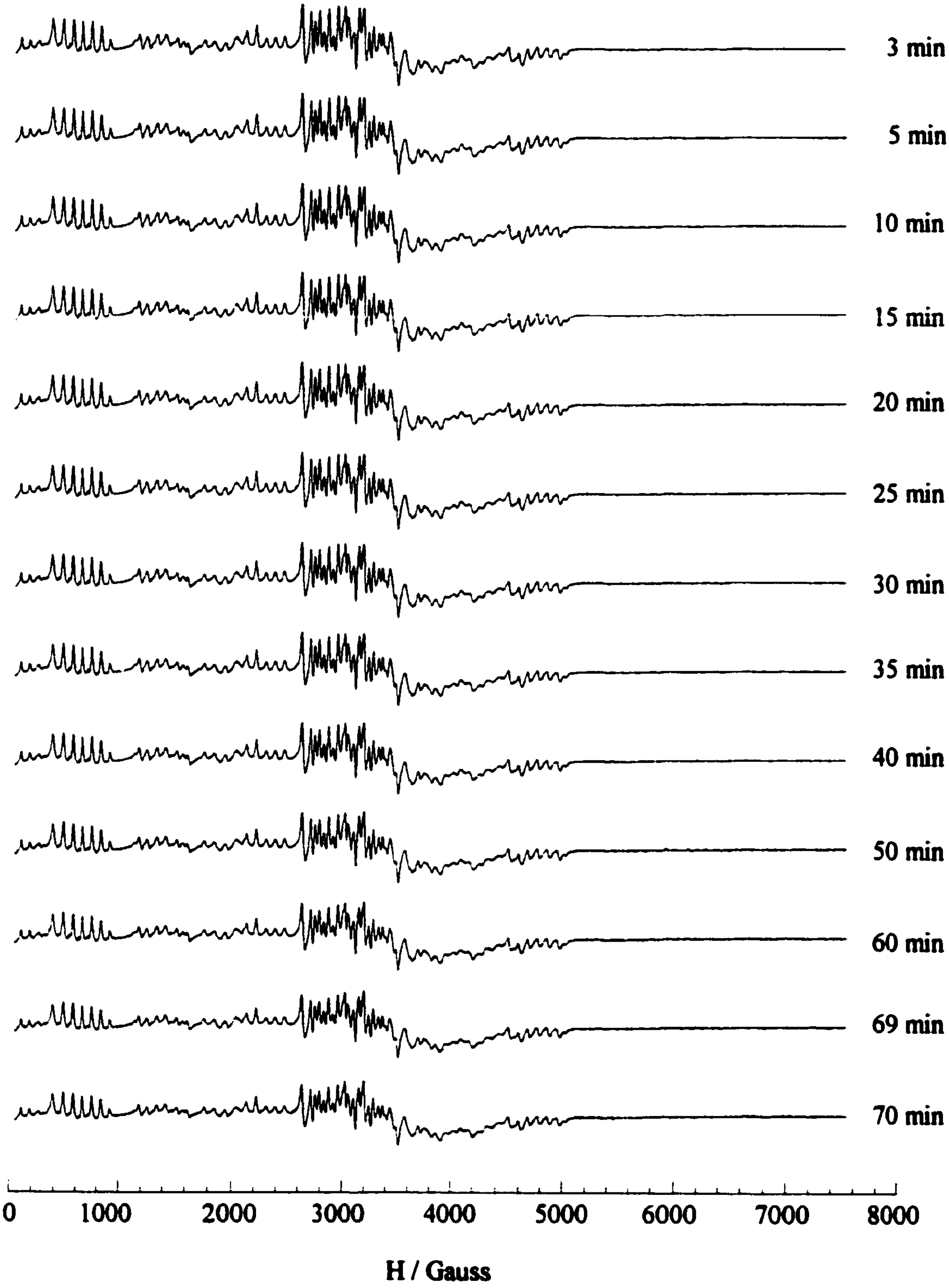

Figure 6.3.1(a) Powder ESR spectra of Mn^{2+} ion in $[Fe(bpp)_2][CF_3SO_3]_2.H_2O$ complex at 104.3K, showing the kinetics of the paramagnetic to diagmagnetic phase transformation. The paramagnetic phase was obtained by rapidly cooling the sample in liquid nitrogen.

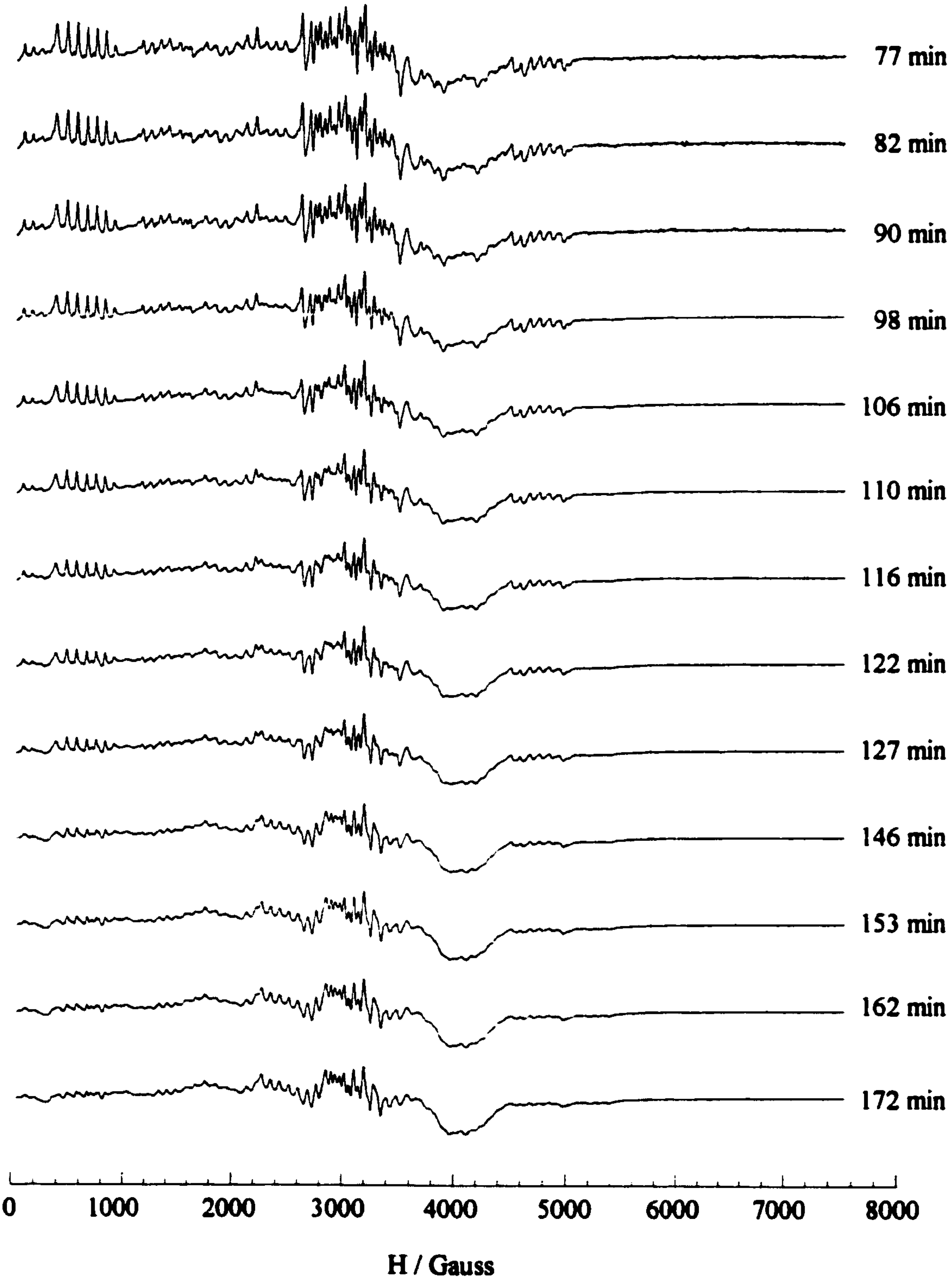

Figure 6.3.1(b) Powder ESR spectra of Mn^{2+} ion in $[Fe(bpp)_2][CF_3SO_3]_2.H_2O$ complex at 104.3K, showing the kinetics of the paramagnetic to diamagnetic phase transformation. The paramagnetic phase was obtained by rapidly cooling the sample in liquid nitrogen.

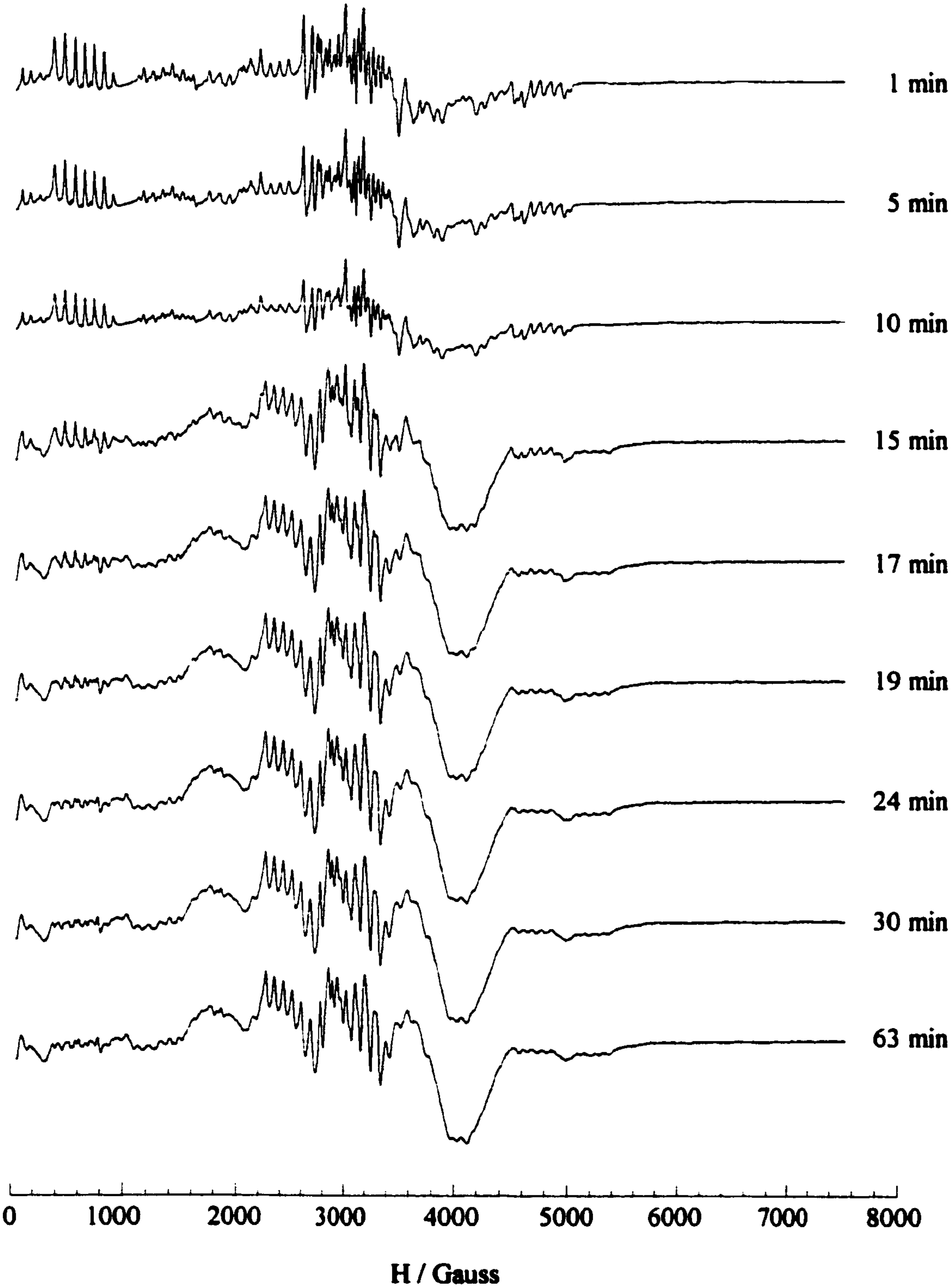

Figure 6.3.2 Powder ESR spectra of Mn^{2+} ion in $[Fe(bpp)_2][CF_3SO_3]_2.H_2O$ complex at 119.6K, showing the kinetics of the paramagnetic to diamagnetic phase transformation. The paramagnetic phase was obtained by rapidly cooling the sample in liquid nitrogen.

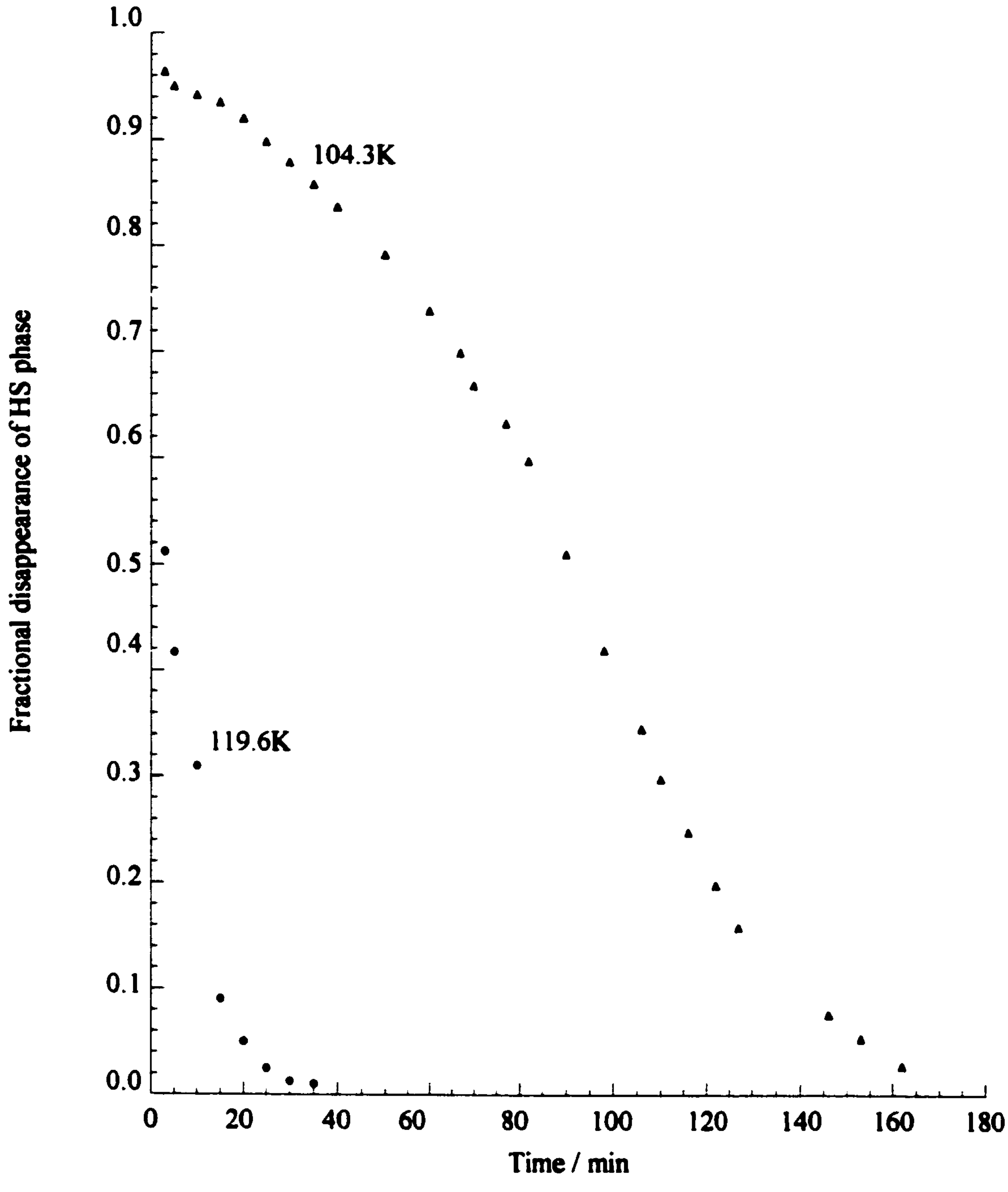

Figure 6.3.3 Kinetic curves of the paramagnetic to diamagnetic phase transformation of $[Fe(bpp)_2][CF_3SO_3]_2.H_2O$ complex at temperatures as indicated. The paramagnetic phase was obtained by rapidly cooling the sample in liquid nitrogen.

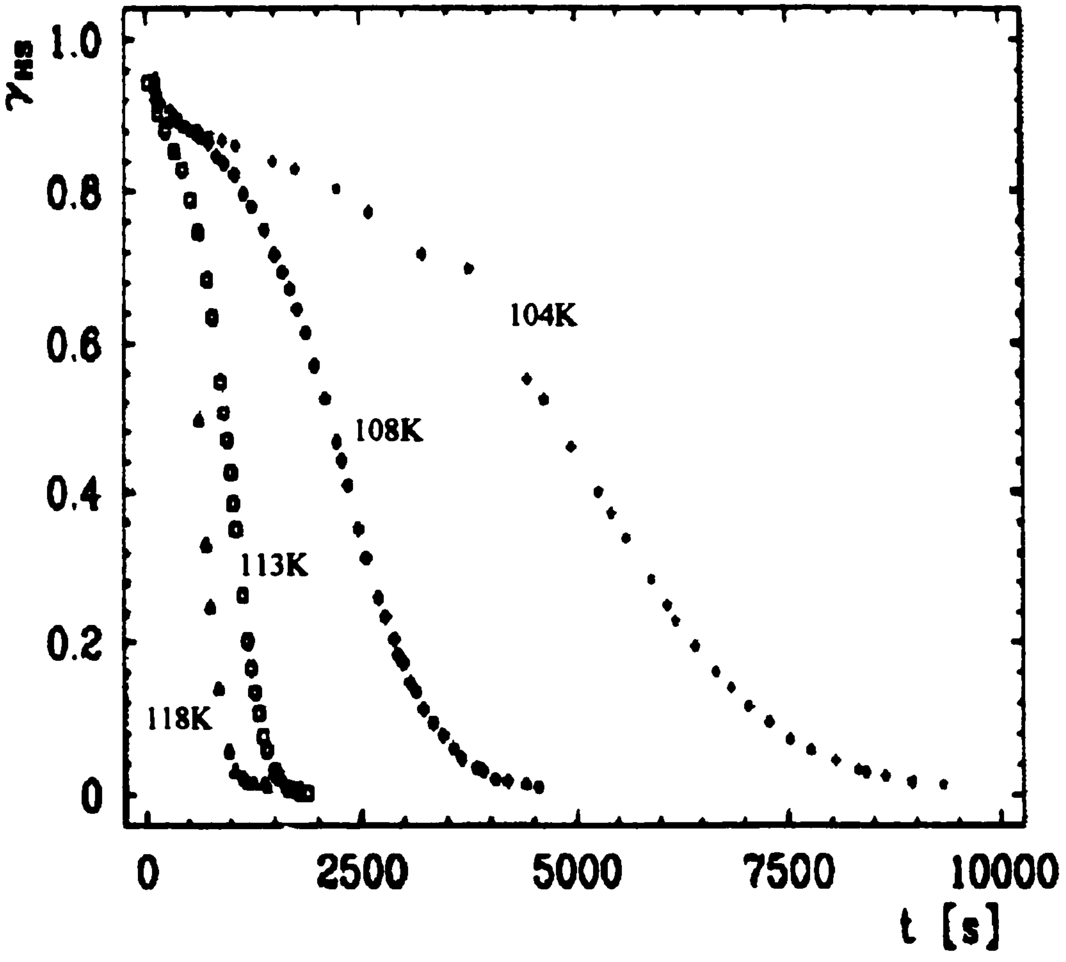

Figure 6.3.4 This figure was taken from reference 73 (figure7), showing the kinetic studies of HS → LS transition in $[Fe(bpp)_2][CF_3SO_3]_2.H_2O$ complex at temperatures as indicated. The HS state was prepared by rapid cooling the sample. The HS fraction $\gamma_{HS}(t)$ was determined from magnetic susceptibility measurements. Note the $\gamma_{HS}(t)$ reaches a minimum in *ca.* 1500s at 118K and *ca.* 9500s at 104K which are comparable to the time scales in the present ESR studies of the HS → LS phase transformation at 119.6K and 104.3K as shown in figure 6.3.3.

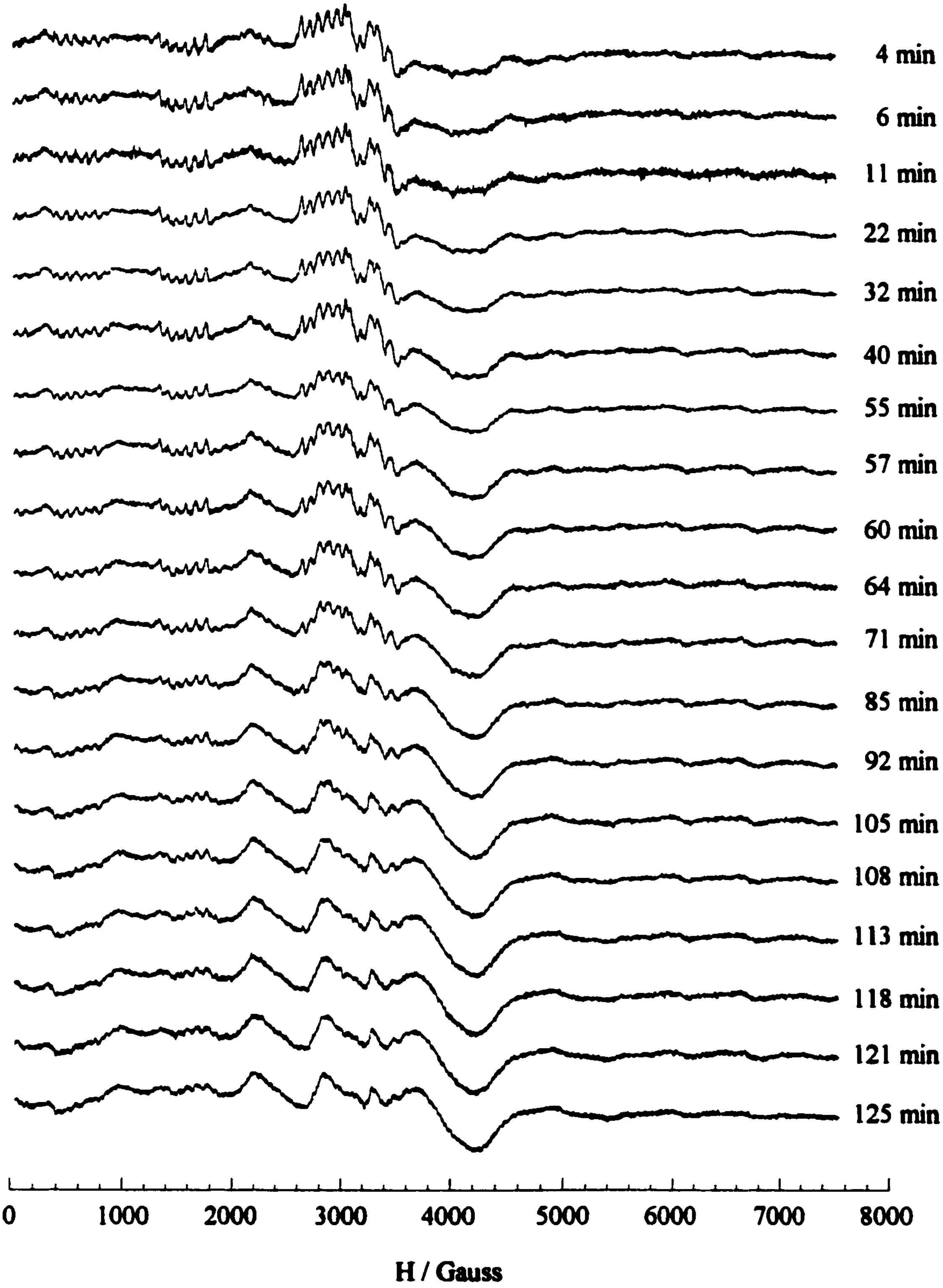

Figure 6.3.5 Powder ESR spectra of Mn^{2+} ion in $[Fe(bpp)_2][BF_4]_2$ complex at 99K, showing the kinetics of the paramagnetic to diamagnetic phase transformation. The paramagnetic phase was obtained by rapidly cooling the sample in liquid nitrogen.

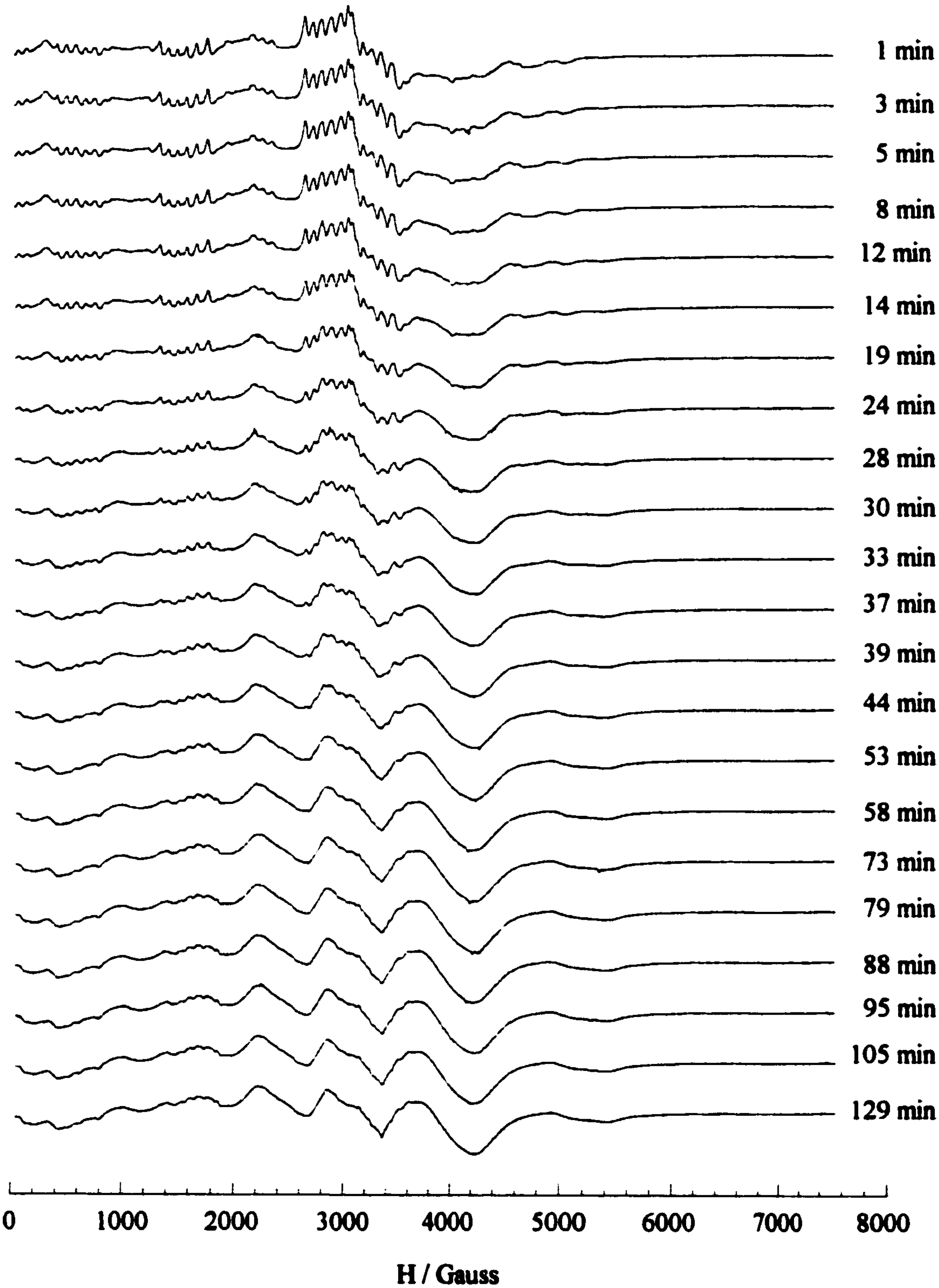

Figure 6.3.6 Powder ESR spectra of Mn^{2+} ion in $[Fe(bpp)_2][BF_4]_2$ complex at 104.7K, showing the kinetics of the paramagnetic to diamagnetic phase transformation. The paramagnetic phase was obtained by rapidly cooling the sample in liquid nitrogen.

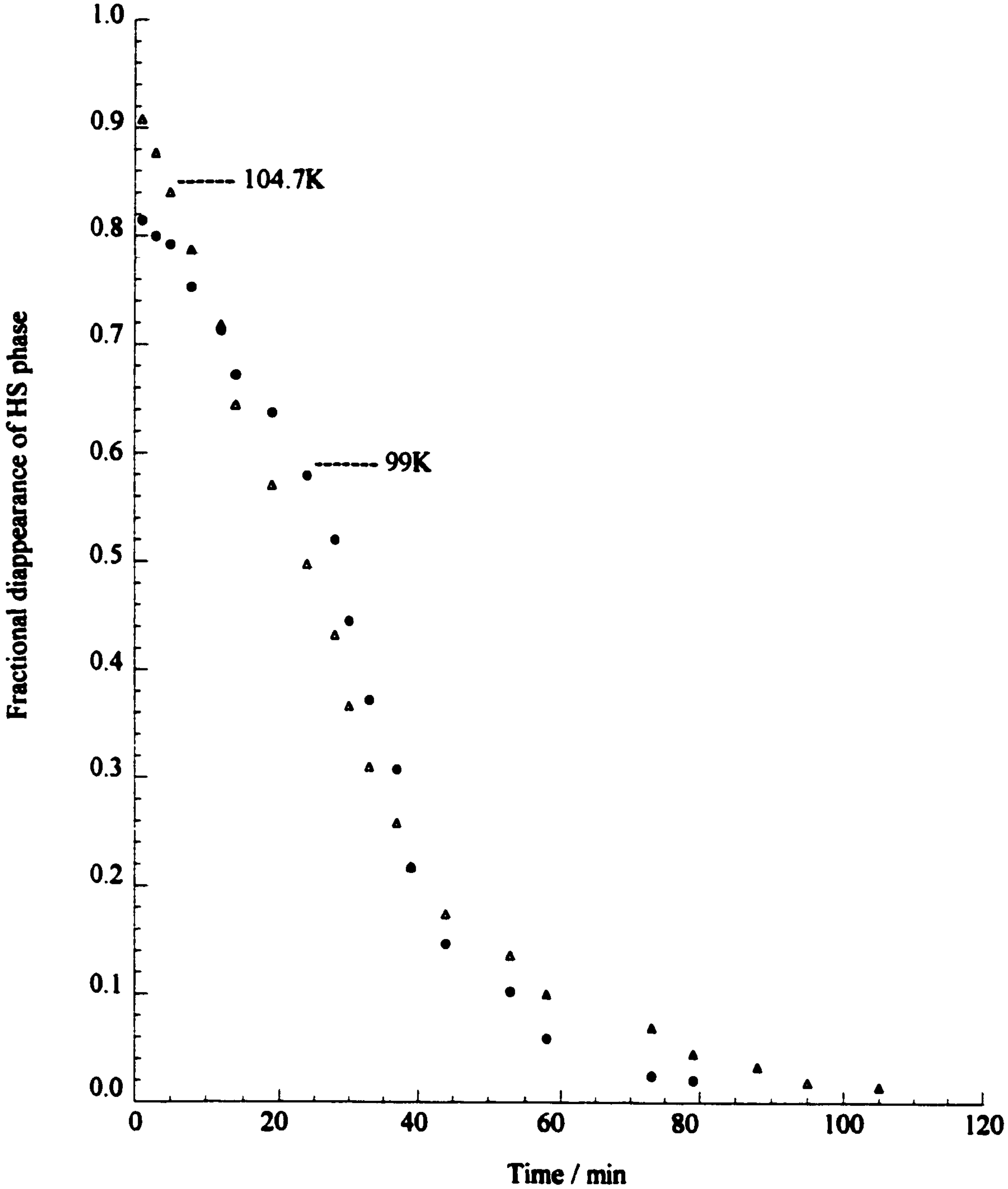

Figure 6.3.7 Kinetic curves of the paramagnetic to diamagnetic phase transformation of the $[Fe(bpp)_2][BF_4]_2$ complex at temperatures as indicated. The paramagnetic phase was obtained by rapidly cooling the sample in liquid nitrogen.

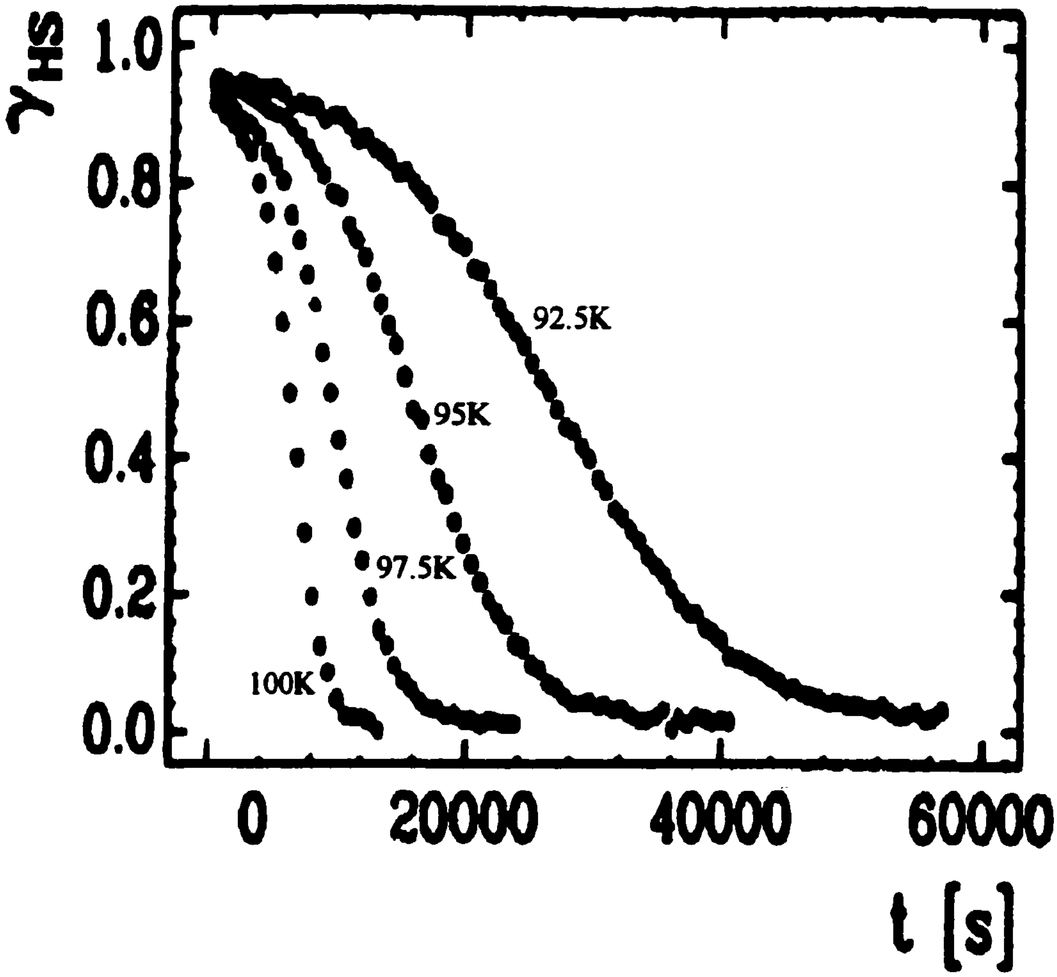

Figure 6.3.8 This figure was taken from reference 68 (figure 3B), showing the HS → LS transition in $[Fe(bpp)_2][BF_4]_2$ complex at temperatures as indicated. The HS state was prepared by rapid cooling of the sample. The HS fraction $\gamma_{HS}(t)$ was determined from Mössbauer spectroscopy. Note the time for $\gamma_{HS}(t)$ to decay to a minimum is *ca.* 10000s at 100K, which is almost double that found in the ESR studies of the HS → LS phase transformation at 99K and 104.7K.

CHAPTER 7

CONCLUSION

The use of Mn^{2+} ion as an ESR probe to study the spin crossover in powder samples of $[Fe(bpp)_2][CF_3SO_3]_2.H_2O$ and $[Fe(bpp)_2][BF_4]_2$ complexes has provided new information on the nature of spin-state transition and phase transformation in these systems.

The results from temperature-dependence studies have shown that the HS ↔ LS crossover in both systems is accompanied by a phase change and during the transition there are separate domains for each spin state. The appearance and disappearance of domains in both systems is deduced from the fact that two kinds of Mn^{2+} spectrum with unique spectral features, in particular the sharp hyperfine structures, for the HS and LS phase were observed during the spin-state transition. This kind of sharp spectral features would not have been observed if the spin states were distributed in a statistically random manner.

The temperature-dependence studies of $[Fe(bpp)_2][CF_3SO_3]_2.H_2O$ complex revealed a sudden transition at 134K, half-way between $T^* = 135 - 133K$ in the cooling direction, and a two-stage transition over the range $T^* = 175 - 180K$ and $T^* = 275 - 284K$ for the first and second stage, respectively, and a plateau region from 180K to 275K in the heating direction. The mid-point temperature for the first and second stage being 177K and 280K, respectively. This thermal hysteresis behavior was originally observed by Buchen *et al.*[73], using magnetic susceptibility measurement, at $T_c^{\downarrow} = 147K$ in the cooling direction and $T_c^{\uparrow} \approx 285K$ for the second stage transition in the heating direction. In Buchen *et al.*[73] studies, the first stage transition occurred over the temperature range 150 - 190K, followed by a plateau region from 190K to 250K before the second stage occurred over the range 250 - 300K. There is a marked difference of 13K in the HS → LS transition temperature as determined by ESR and that found by Buchen *et al.*[73], but the reverse transition temperatures are in good agreement except the LS → HS conversion occurs over a much smaller temperature interval of 5K and 9K for the first and second stage transition, respectively, in the ESR measurements relative to the 40K and 50K for the corresponding stages reported by Buchen *et al.*[73] These discrepancies may simply be due to differences in the final process of drying the samples. The presence of varying amounts of water molecules within the crystal lattice may have a profound effect on the spin crossover phenomenon. This has been shown by König *et al.*[83] in their studies of the significance of lattice water on the spin-state transition in the $[Fe(phen)_2][C_2O_4].5H_2O$ complex.

ESR studies of $[Fe(bpp)_2][BF_4]_2$ complex showed a transition from 167K to 164K centered at T^* = 166K and from 171K to 175K centered at T^* = 173K in the cooling and heating directions, respectively, giving a 7K difference in the hysteresis curves. Buchen *et al.*[68] reported $T_c^{\downarrow}$ = 170K and $T_c^{\uparrow}$ = 180K with ΔT_c = 10K, and Goodwin *et al.*[72] reported $T_c^{\downarrow}$ = 173K and $T_c^{\uparrow}$ = 183K also with ΔT_c = 10K for the same compound. The differences in the transition temperatures found by ESR and those reported by Buchen *et al.*[68] and Goodwin *et al.*[72] are small. The width of the hysteresis loop ΔT_c is 7K in our ESR results and 10K in the other studies[68,72]. Again the small discrepancies in ΔT_c and the transition temperatures could be attributed to the slight differences in the drying process.

The present ESR studies of the Mn^{2+} doped $[Fe(bpp)_2][CF_3SO_3]_2.H_2O$ and $[Fe(bpp)_2][BF_4]_2$ complexes have also found that the zero-field splitting parameters for Mn^{2+} in the HS and LS phases of both systems are very different, indicating that the spin crossover in these systems is accompanied by a phase transformation; while other workers[68,72,73] could only infer a phase transformation from the thermal hysteresis behavior of the systems. The use of zero-field splitting parameters for Mn^{2+} ion in other Fe^{2+} spin crossover systems has also been shown[43,44,55-57] to be a reliable measure of a phase transformation.

The irradiation experiments on both the $[Fe(bpp)_2][CF_3SO_3]_2.H_2O$ and $[Fe(bpp)_2][BF_4]_2$ systems showed that the HS state formed by the LIESST effect at 77K is not accompanied by the phase change that occurs in the thermal transition. The failure to induce a reverse LIESST effect in these complexes by using the red line from a Kr-laser is in agreement with the results obtained by Buchen *et al.*[68,73] at low temperatures, who were able to find only a 5% conversion back to the LS state. The explanation for this is found in our discovery that the Kr-laser also causes the LIESST effect and converts LS to HS with no phase change. The bands associated with the LIESST and reverse LIESST effect must overlap in the region of irradiation, and the rate of HS → LS conversion must be slower than the rate of LS → HS conversion.

The kinetic studies of Buchen *et al.*[68,73] on the HS → LS conversion in rapidly cooled sample of the $[Fe(bpp)_2][CF_3SO_3]_2.H_2O$ agree very well with our kinetic studies of the phase transformation, using the ESR of Mn^{2+}, in the same compound. The same ESR studies on $[Fe(bpp)_2][BF_4]_2$ complex shows that the phase transformation occurs at twice the rate of HS → LS transition reported by Buchen *et al.*[68] These results indicate that the HS → LS transition follows the phase transformation. Thus the high temperatures needed to cause the HS → LS change, when the HS state is formed by rapidly cooling the HS state, is readily explained by the necessity for a phase change to occur first followed by the spin conversion. The high temperatures needed in these two compounds to cause the HS → LS conversion[68,73] in samples whose HS was caused by the LIESST effect cannot be blamed on the necessity for a phase change, because we found no evidence for any change in phase when the HS state was produced. Our results indicate that some other reason must be sought to explain the long lifetimes, below 80K, for the HS state in these two compounds when produced by the LIESST effect. Since we see no change in the ESR spectra, it seems unlikely that any ESR experiments will shed any light on this problem.

This study has shown the utility studying the spin crossover transition with ESR along with the more traditional techniques of Mössbauer spectroscopy and magnetic susceptibility. These last two techniques measure magnetic changes in the Fe^{2+} complex itself while the ESR measurements of Mn^{2+}-doped into samples detect changes in the surrounding lattice during the spin crossover.

The knowledge and experience gained from the present studies of the Mn^{2+}-$[Fe(bpp)_2][CF_3SO_3]_2.H_2O$ and $[Fe(bpp)_2][BF_4]_2$ systems would be useful in the planning of future work to be done in a more systematic way. Each of the two systems has a different behavior, and they are quite different from the other Fe^{2+} spin crossover systems studied in the past. Since the amount of solvent incorporated in an Fe^{2+} system can have a profound effect on the nature of the spin crossover, this can be determined by controlling the drying process of the samples obtained from the same batch. The samples should be carefully dried to a constant weight prior to measurements. Although there is not much can be done about the amount of dopant in the system, salts with different solubility can be tried to gain some control of the doping process. This may help in the future ESR study of the [Fe(5-NO_2-sal-N(1,4,7,10))] system. One could also try to grow single crystals of the compound to be studied using the gel diffusion technique. The technique involves the making of a gel in a U-shape tube and allowing suitable solutions containing the appropriate reactants to diffuse from both openings, the reaction at the junction where the two solutions meet may produce single crystals of the compound. Experimental measurements of the same compound can also be done at another laboratory using a different instrument, this would allow the results to be more reliably compared. The present equipment in this laboratory would only allow the temperature-dependence studies to 77K, it is hoped that liquid hydrogen or helium temperature could be available in the near future. This would allow the reverse LIESST effect in the present systems to be properly addressed. The laser irradiation process can be improved by using a mechanical rotating device connected directly to the sample tube in the finger Dewar to enable a more accurate judgment of the uniformity of the sample volume being illuminated. The time-dependence studies of the $[Fe(bpp)_2][CF_3SO_3]_2.H_2O$ and $[Fe(bpp)_2][BF_4]_2$ systems can also be done at more temperature intervals to allow for the results to be compared with those obtained by other methods at similar temperature intervals. This time-dependence study can also be extended to include other known Fe^{2+} spin crossover systems such as $[Fe(paptH)_2][NO_3]_2$[84,85], cis-$[Fe(bpen)][NCS]_2$[86] and $[FeL][CN]_2.H_2O$[87] which appear to be promising candidates. This may provide a better understanding of the relation between the spin-state transition and phase transformation in a spin crossover compound. Finally, the simulations of ESR spectra of Mn^{2+} ion doped into the systems should be carried out using a more elaborate computer program, such as the one being developed by Misra[88], to allow for a more accurate evaluation of the zero-field splitting parameters.

REFERENCES

1. A. J. Bard, Electron Spin Resonance, in Standard Methods of Chemical Analysis, 6th Ed., *3(A)*, F. J. Welcher, Ed., Van Nostrand, New York, 1962
2. M. Bersohn and J. C. Baird, An Introduction to Electron Paramagnetic Resonance, Benjamin, New York, 1966
3. H. M. Assenheim, Introduction to Electron Spin Resonance, Plenum Press, New York, 1967
4. A. Carrington and A. D. McLachlan, Introduction To Magnetic Resonance. With Applications to Chemistry and Chemical Physics, Harper International Edition, Harper and Row, New York, 1967
5. I. B. Goldberg and A. J. Bard, Electron Spin Resonance Spectroscopy, in Treatise on Analytical Chemistry, ***10**(1)*, 2nd Ed., I. M. kolthoff and P. J. Elving, Eds., John Wiley & Sons, New York, 1983
6. J. E. Wertz and J. R. Bolton, Electron Spin Resonance. Elementary Theory and Practical Applications, Chapman and Hall, New York, 1986
7. J. E. Wertz, *Chem. Rev.*, ***55***, 829 (1955)
8. E. G. Janzen, *Anal. Chem.*, ***44***, 113R (1972)
9. E. G. Janzen, *Anal. Chem.*, ***46***, 478R (1974)
10. J. R. Wasson and P. J. Corvan, *Anal. Chem.*, ***50***, 92R (1978)
11. D. L. Williams-Smith and S. Wyard, *Progr. Med. Chem.*, ***12***, 191 (1975)
12. B. Clarkson, P. H. Davis, J. Forrer, M. J. Nilges, M. D. W. Wang, R. L. Belford, R. Timken, T. Walczak, M. C. Thurnauer, J. R. Norris, A. L. Morris and Y. Zhang, *Appl. Magn. Reson.*, ***6***, 195 (1994)
13. C. J. Ballhausen, Introduction to Ligand Field Theory, McGraw-Hill, New York, 1962
14. B.N. Figgis, Introduction to Ligand Fields, Interscience, New York, 1966
15. J. W. Orton, Electron Paramagnetic Resonance, An Introduction to Transition Group Ions in crystals, Iliffe, London, 1968

16. A. Abragam and B. Bleaney, Electron Paramagnetic Resonance of Transition Ions, Clarendon Press, Oxford, 1970
17. F. A. Cotton, Chemical Applications of Group Theory, 3rd ed., John Wiley & Sons, New York, 1990
18. B. R. McGarvey, Electron Spin Resonance of Transition-Metal Complexes, in Transition Metal Chemistry, *3*, 89, R. L. Carlin, Ed., Marcel Dekker, New York, 1966
19. E. König, Electron Paramagnetic Resonance, in Physical Methods in Advanced Inorganic Chemistry, H. A. O. Hills and P. Day, Eds., Interscience, 1968
20. S. K. Misra and J. S. Sun, *Mag. Res. Rev.*, ***16***, 57 (1991)
21. G. C. Upreti and P. Chand, *Mag. Reson. Rev.*, ***12***, 245 (1987)
22. E. Fermi, *Z. Physik*, ***60***, 320 (1930)
23. B. Bleaney and K. W. H. Stevens, *Repts. Progr. Phys.*, ***16***, 108 (1953)
24. B. Bleaney and R. S. Trenam, *Proc. Roy. Soc., (London)*, ***223A***, 1 (1954)
25. K. D. Bowers and J. Owen, *Repts. Progr. Phys.*, ***18***, 304, (1955)
26. B. Bleaney, *Phil. Mag.*, ***42***, 441 (1951)
27. W. Gordy, Theory and Applications of Electron Spin Resonance, John Wiley & Sons, New York, 1980
28. C. F. Kokoszka and G. Gordon, Electron Paramagnetic Resonance, in Technique of Inorganic Chemistry, *7*, H. B. Jonassen and A. Weissberger, Eds., Interscience, New York, 1968
29. S. K. Misra, *Physica B*, ***203***, 193 (1994)
30. S. K. Misra, *Physica B*, ***240***, 183 (1997)
31. F. K. Kneubühl, *J. Chem. Phys.*, ***33***, 1074 (1960)
32. Y. Tanabe and S. Sugano, *J. Phys. Soc. Jpn.*, ***9***, 753 (1954)
33. E. König and S. Kremer, *Theoret. Chim. Acta*, ***23***, 12 (1971)
34. E. König and K. J. Watson, *Chem. Phys. Letters*, ***6***, 457 (1970)
35. M. A. Hoselton, L. J. Wilson and R. S. Drago, *J. Am. Chem. Soc.*, ***97***, 1722 (1975)
36. B. A. Katz and C. E. Strouse, *J. Am. Chem. Soc.*, ***101***, 6214 (1979)
37. M. Mikami, M. Konno and Y. Saito, *Acta Cryst.*, ***B36***, 275 (1980)

38. J. G. Leipoldt and P. Coppens, *Inorg. Chem.*, ***12***, 2269 (1973)

39. J. Albertsson, A. Oskarsson and M. Nygren, *Acta Cryst.*, ***B35***, 1473 (1979)

40. E. König, G. Ritter and S. K. Kulshreshtha, *Chem. Rev.*, ***85***, 219 (1985)

41. E. König, *Progr. Inorg. Chem.*, ***35***, 527 (1987)

42. E. König, *Struct. Bonding*, ***76***, 53 (1991)

43. A. Ozarowski, Y. Shunzhong, B. R. McGarvey, A. Mislankar and J. E. Drake, *Inorg. Chem.*, ***30***, 3167 (1991)

44. A. Ozarowski and B. R. McGarvey, *Inorg. Chem.*, ***28***, 2262 (1989)

45. P. Gütlich, R. Link and A. Trautwein, Mössbauer spectroscopy and Transition Metal Chemistry, Springer-Verlag, 1978

46. W. Irler, G. Ritter, E. König, H. A. Goodwin and S. M. Nelson, *Solid State Commun.*, ***29***, 39 (1979)

47. E. König and K. Madeja, *Chem. Commun.*, ***3***, 61 (1966)

48. G. Ritter, E. König, W. Irler and H. A. Goodwin, *Inorg. Chem.*, ***17***, 224 (1978)

49. M. Sorai and S. Seki, *J. Phys. Soc. Japan*, ***33***, 575 (1972)

50. M. Sorai and S. Seki, *J. Phys. Chem. Solids*, ***35***, 555 (1974)

51. P. Gütlich, *Struct. Bonding*, ***44***, 83 (1981)

52. H. A. Goodwin, *Coord. Chem. Rev.*, ***18***, 293 (1976)

53. H. Toftlund, *Coord. Chem. Rev.*, ***94***, 67 (1989)

54. R. L. Martin and A. H. White, The Nature of the Transition between High-spin and Low-spin Octahedral Complexes of the Transition Metals, in Transition Metal Chemistry, ***4***, R. L. Carlin Ed., Marcel Dekker, Inc. New York (1968)

55. P. S. Rao, A. Reuveni, B. R. McGarvey, P. Ganguli and P. Gütlich, *Inorg. Chem.*, ***20***, 204 (1981)

56. P. E. Doan and B. R. McGarvey, *Inorg. Chem.*, ***29***, 874 (1990)

57. A. Ozarowski, B. R. McGarvey, A. B. Sarkar and J. E. Drake, *Inorg. Chem.*, ***27***, 628 (1988)

58. S. Decurtins, P. Gütlich, C. P. Köhler, H. Spiering and A. Hauser, *Chem. Phys. Letters*, ***105***, 1 (1984)

59. S. Decurtins, P. Gütlich, K. M. Hasselbach, A. Hauser and H. Spiering, *Inorg. Chem.*, ***24***, 2174 (1985)
60. P. L. Franke, J. G. Haasnoot and A. P. Zuur, *Inorg. Chim. Acta*, ***59***, 5 (1982)
61. E. W. Muller, J. Ensling, H. Spiering and P. Gütlich, *Inorg. Chem.*, ***22***, 2074 (1983)
62. A. Hauser, *Chem. Phys. Letter*, ***124***, 543 (1986)
63. A. Hauser, P. Gütlich and H. Spiering, *Inorg. Chem.*, ***25***, 4245 (1986)
64. A. Hauser, *J. Chem. Phys.*, ***94***, 2741 (1991)
65. A. Hauser, *Coord. Chem. Rev.*, ***111***, 275 (1991)
66. P. Poganiuch and P. Gütlich, *Inorg. Chem.*, ***26***, 455 (1987)
67. P. Poganiuch, S. Decurtins and P. Gütlich, *J. Am. Chem. Soc.*, ***112***, 3270 (1990)
68. Th. Buchen, P. Gütlich and H. A. Goodwin, *Inorg. Chem.*, ***33***, 4573 (1994)
69. D. C. Fisher and H. G. Drickamer, *J. Chem. Phys.*, ***54***, 4825 (1971)
70. C. B. Bargeron and H. G. Drickamer, *J. Chem. Phys.*, ***55***, 3471 (1971)
71. H. G. Drickamer and C. W. Frank, Electronic Transitions and the High Pressure Chemistry and Physics of Solids, Chapman and Hall, 1973
72. H. A. Goodwin and K. H. Sugiyarto, *Chem. Phys. Letters*, ***139***, 470 (1987)
73. Th. Buchen, P. Gütlich, K. H. Sugiyarto and H. A. Goodwin, *Chem. Eur. J.*, ***2***, No.9, 1134 (1996)
74. V. Petrouleas and J.-P. Tuchagues, *Chem. Phys. Letters*, ***137***, 21 (1987)
75. D. Boinnard, A. Bousseksou, A. Dworkin, J.-M. Savariault, F. Varret and J.-P. Tuchagues, *Inorg. Chem.*, ***33***, 271, (1994)
76. Yang-i Lin and S. A. Lang, Jr., *J. Heterocylic Chem.*, ***14***, 345 (1977)
77. K. H. Sugiyarto and H. A. Goodwin, *Aust. J. Chem.*, ***41***, 1645 (1988)
78. B. Mabad, P. Cassoux, J.-P. Tuchagues and D. N. Hendrickson, *Inorg. Chem.*, ***25***, 1420 (1986)
79. A. Rakotonandrasana, D. Boinnard, J.-M. Savariault, J.-P. Tuchagues, V. Petrouleas, C. Cartier and M. Verdaguer, *Inorg. Chim. Acta*, ***180***, 19 (1991)
80. T. H. Wilmshurst, Electron Spin Resonance Spectrometers, Plenum Press, New York, 1968

81. C. P. Poole, Jr., Electron Spin Resonance, A Comprehensive Treatise on Experimental Techniques, Interscience, New York, 1967
82. R. S. Alger, Electron Paramagnetic Resonance: Techniques and Applications, Interscience, 1968
83. E. König, R. Schnakig, G. Ritter, W. Irler, B. Kanellakopulos and B. Powietzka, *Inorg. Chim. Acta*, ***35***, 239 (1979)
84. R. N. Sylva and H. A. Goodwin, *Aust. J. Chem.*, ***20***, 479 (1967)
85. G. Ritter, E. König, W. Irler and H. A. Goodwin, *Inorg. Chem.*, ***17***, 224 (1978)
86. H. Toftlund, E. Pedersen and S. Yde-Andersen, *Acta Chem. Scand.*, ***A38***, 693 (1984)
87. E. König, G. Ritter, J. Dengler and S. M. Nelson, *Inorg. Chem.*, ***26***, 3582 (1987)
88. S. K. Misra, computer program (private communication), to be published.

VITA AUCTORIS

Raymond Chi Wai Sung was born on September 8, 1953 in Hong Kong. He received most of his education in Hong Kong and England. He graduated from the University of Essex with a B.Sc. Honors degree in chemistry in 1978, and obtained a M.Sc. degree in analytical chemistry from the University of East Anglia in 1989. He has been teaching advanced-level chemistry at Delia Memorial School in Hong Kong from 1981 to 1986, and physical chemistry at the Hong Kong Polytechnic from 1982 to 1987. He has also taught at Maria College in Hong Kong from 1988 to 1992, Open College in Hong Kong from 1988 to 1992, and analytical chemistry at the Hong Kong Polytechnic from 1988 to 1992.

The author started his Ph.D. studies in chemistry under the guidance of Dr. Bruce R. McGarvey at the University of Windsor in 1992. He has been a research assistant, and teaching assistant in the Department of Chemistry and Biochemistry from 1992 to 1997.